Size Dependence of Mechanical Responses of Materials in Small-Volume Structures

by

Yoonjoon Choi

M.S., Inorganic Materials Engineering,
Seoul National University, 1992

B.S., Inorganic Materials Engineering,
Seoul National University, 1990

Submitted to the Department of Materials Science and Engineering
in partial fulfillment of the requirements for the degree of

Doctor of Philosophy in Materials Science and Engineering

at the

MASSACHUSETTS INSTITUTE OF TECHNOLOGY

June 2003

MASSACHUSETTS INSTITUTE OF TECHNOLOGY
JAN 07 2004
LIBRARIES

© Massachusetts Institute of Technology 2003. All rights reserved.

Author .....
Department of Materials Science and Engineering
February 27, 2003

Certified by .....
Subra Suresh
Ford Professor of Engineering
Thesis Supervisor

Accepted by .....
Harry L. Tuller
Professor of Ceramics and Electronic Materials
Chair, Departmental Committee on Graduate Students

ARCHIVES

Size Dependence of Mechanical Responses of Materials in Small-Volume Structures

by

Yoonjoon Choi

Submitted to the Department of Materials Science and Engineering
on April 25, 2003, in partial fulfillment of the
requirements for the degree of
Doctor of Philosophy in Materials Science and Engineering

Abstract

The effect of length scales on mechanical responses of materials in small-volume structures, such as thin films and patterned lines on substrates, is examined. The understanding of stress evolution and deformation behavior of those materials is one of major factors in the fabrication, performance, and reliability of microelectronic devices. The length scales involved in such materials are on the order of 1 μm, and the deformation characteristics of the materials exhibit a strong dependence on their physical size such as film thickness and line width, as well as their microstructural length scale such as grain size. In this thesis, analytical, experimental, and computational approaches are utilized to elucidate the effect of length scales on the time-independent inelastic deformation of materials in small-volume structures. Experiments focus on continuous thin films and patterned lines of Al on Si substrates. The inelastic deformation of a material can be described by parameters which range from global constitutive (stress-strain) relations to atomistic descriptions of defect generation. An analytical model based on the generation of an array of dislocation loops is used to rationalize the film-thickness and grain-size effect on the stress evolution of thin metallic films on thick substrates. The consequence of the dislocation generation restricted by the film thickness and grain size leads to the full description of stress-temperature histories in an Al film on a Si substrate, which is subjected to thermal cycling, by incorporating the constitutive law of kinematic hardening. Systematic nanoindentation experiments on continuous thin films and patterned lines on Si substrates explore another length scale (line width) effect on the indentation load-displacement response. Computational modeling at the continuum (finite element analysis) and atomistic (molecular dynamics) levels presented herein provides insights into the origin of such size effects by correlating with the experimental observations. Based on the premise of dislocation-mediated deformation, such size effects on the mechanical responses of materials in small-volume structures arise from the equilibrium distribution of dislocations, which are tailored by the interaction of those dislocations with microstructural, physical length scales of materials, as well as various loading conditions.

Thesis Supervisor: Subra Suresh
Title: Ford Professor of Engineering

Acknowledgments

Nothing in the world is softer than water,
Yet nothing is better at overcoming the hard and strong.
This is because nothing can alter it.

That the soft overcomes the hard
And the gentle overcomes the aggressive
Is something that everybody knows, but none can do themselves.
Therefore the sages say:
The one who accepts the dirt of the state becomes its master.
The one who accepts its calamity becomes king of the world.

Truth seems contradictory. — Lao Tzu, The Tao Te Ching, Ch. 78, Translated by C. Muller.

Water flows as life should flow. It goes around all obstacles. In doing so, it wears them down by its persistence. Water does not oppose. Water merely goes the way of its own nature. It remains calm and serene. All power lies in such a course. Your victory lies in not distorting your true and original nature. There is one who wants to be as water and who has been just turned one of meanders in his river. No one knows how many shoals and meanders he gets through to reach the ocean. Just praying someday he can see the dazzling horizon of the blue ocean.

During last five years I owe a lot to people around me to accept a challenge I could not face without them. The only thing I can do for them is to leave my gratitude here, even if most of them may not see this monologue.

First of all I would like to thank my advisor, Prof. Subra Suresh, for providing his guidance and for giving me great opportunity. Without his enthusiastic support, I may not finish my work at MIT. I feel fortunate to have work with and for someone who is full of enthusiasm to pursue the light of science and of appreciation to construct the bigger picture in every aspect. I would also like to thank to my committee members, Prof. Samuel M. Allen and Prof. S. Mark Spearing, for their valuable comments and encouragement.

My memory of MIT will simply fade away without recalling people of LEXCOM. First I thank Mr. George Labonte and Mr. Kenneth Greene for helping me out everything from the beginning. I am still missing the cheerful atmosphere in the basement with Raj. I'd like to express my best gratitude to Andrew and Krystyn for reading and commenting my thesis with great patient, I believe, then to Kob and Ming for helping me on all kinds of computational stuff. My obsolete understanding of Thermodynamics and Physics was rejuvenated very much by Tae-soon, and we always had a nice conversation on everything

over beer glasses, especially with our mother tongue. I sincerely hope our friendship will continue forever in spite of our separation over the globe. I am so much obliged to Prof. Sang-gook Kim for giving me a chance to experience this wonderful place. I am also happy to have spent time with many Koreans: Jae-Joong, Yong-Nam, Dong-Won, Yong-Ki, and so many others. I am definitely not thanking everyone properly here, but you are in my thoughts as I am tumbling to finish this thesis.

Finally I must admit that all I have done here would not be possible without endless support and love from my family: My parents and parents-in-law who are always in my side from the bottom of their hearts, My brothers and sisters who have been taken care of my absent for long time. Most of all, I thank my beloved wife and son, Kyung-Ah and JaeHyun, for understanding, supporting, and loving me in every situation. I am truely sorry for not having enough time to share with you. My love to them is absolutely beyond my words.

Contents

1 Introduction **21**

2 Size Effects on the Mechanical Properties of Thin Polycrystalline Metal Films on Substrates **27**

2.1 Introduction 28

2.2 Analysis 32

2.3 Comparison with Experimental Data 37

2.3.1 Polycrystalline Al thin films on Si substrates 37

2.3.2 Passivated polycrystalline Cu thin films on Si substrates 41

2.3.3 Polycrystalline Cu thin films on a deformable substrate 43

2.4 Discussion 45

2.5 Conclusions 49

3 Stress evolution of an Al thin film on a Si substrate during thermal cycling **51**

3.1 Introduction 51

3.2 Background 53

3.2.1 The Bauschinger effect 53

3.2.2 Kinematic hardening 55

3.2.3 Constitutive law 56

3.3 Experiments 57

3.4 Results 58

3.5 Discussion 60

3.6 Conclusions 63

4 Nanoindentation of Continuous Films and Patterned Lines on Si Substrates 65

4.1 Introduction 65

4.2 Materials and Experimental Procedures 68

4.3 Experimental Results 72

4.3.1 Evaluation of tip radius 72

4.3.2 Nanoindentation of continuous films 72

4.3.3 Nanoindentation of patterned lines 77

4.4 Discussion 81

4.4.1 Plastic zone size 82

4.4.2 Discrete dislocation model 84

4.5 Summary of Experimental Observations 86

5 Simulations of Nanoindentation on Thin Films and Patterned Lines 89

5.1 Finite Element Simulation of Nanoindentation 89

5.1.1 Introduction 89

5.1.2 Finite element modeling 91

5.1.3 Simulation results of FEM 93

5.1.4 Correlation with experiment 98

5.2 Atomistic Simulation of Nanoindentation 103

5.2.1 Introduction 103

5.2.2 MD Simulation of indentation on a 2-D crystal 104

5.2.3 Correlation of 2-D MD simulation with experiment 107

5.2.4 MD Simulation of indentation on 3-D crystals 111

5.3 Discussion 113

5.4 Conclusions 117

6 Concluding Remarks and Suggestions for Future Work **119**

A Nanocrystallization During Nanoindentation of a Bulk Amorphous Metal Alloy at Room Temperature **123**

B Nanoindentation Experimental Details **133**

B.1 Experimental procedure on NanoTest 600 133

B.2 Experimental procedure on Triboindenter 135

List of Figures

2-1 A schematic of dislocation loop structure along an inclined slip plane of a grain, where d is the grain size, h_f is the film thickness, z is the distance between loops, Φ is the angle between slip planes and film surface normal, $\mathbf{b}$ is the Burgers vector, and σ is the applied stress, or the film mismatch stress. 35

2-2 Stress evolution in thin polycrystalline Al films on Si substrates during cooling, (a) for d=0.9 μm and h_f=0.98 μm, and (b) for d=0.9 μm and h_f=0.18 μm. Symbols are experimental data from Venkatraman and Bravman [21] , solid lines are calculated from Eq. (2.12), and dashed lines are calculated from Eq. (2.3). 38

2-3 Stress evolution in thin polycrystalline Al films on Si substrates during cooling, for h_f=0.98 μm and h_f=0.18 μm for a fixed grain size of 0.9 μm. Symbols are experimental data from Venkatraman and Bravman [21], solid lines are calculated from Eq. (2.12) when $R = (d + h_f')/4$, and dashed lines are calculated from Eq. (2.12) when $R = \sqrt{dh_f'/\pi}$. 39

2-4 Stresses in thin polycrystalline Al films on Si substrates with d=0.9 μm, 1.9 μm, and laser reflowed large grain as a function of film thickness at 60°C. Symbols are experimental data from Venaktraman and Bravman [21], solid lines are calculated from Eq. (2.12), and dashed line is calculated from Eq. (2.3). 40

2-5 Stress evolution in passivated thin polycrystalline Cu films on Si substrates during cooling, (a) for d=0.35 μm and h_f=0.45 μm, and (b) d=1.3 μm and h_f=1.0 μm. Symbols are experimental data from Keller *et al.* [22], solid lines are calculated from Eq. (2.12), and dashed line is calculated from Eq. (2.3). 42

2-6 Stress at room temperature and at 250°C for passivated thin polycrystalline Cu films on Si substrates as a function of film thickness. Open symbols are experimental data from Keller *et al.* [22], filled symbols are calculated from Eq. (2.12), and solid line is calculated from Eq. (2.3). 43

2-7 Stress–strain behavior of a thin polycrystalline Cu film on a polyimide substrate at room temperature, for h_f=1.0 μm and d = 0.9 μm. Symbols are experimental data from Hommel and Kraft [46]and lines are calculated from Eq. (2.13). 44

2-8 Residual strain at room temperature as a function of film thickness in thin polycrystalline Al film on Si substrate for a imposed thermal strain. Grain size is assumed to be the same as the film thickness. Solid lines with symbols are calculated from Eq. (2.12) for η=0.6 and 0.8, and dashed line represents the imposed thermal strain ($\varepsilon_{\text{thermal}}$=0.00714). 47

2-9 Stresses in thin polycrystalline Al film on Si substrate as a function of total strain with different film thicknesses. Grain size, d, is fixed at 0.9 μm. Symbols are replotted from Fig. 2-2, and solid lines are calculated from Eq. (2.12). 48

3-1 Stresses, normalized by the shear moduli (26 and 44 GPa for Al and Cu, respectively), of Cu films (with and without a passivation layer) [55] and Al films (with only a native oxide) [56] of the same film thickness (h_f = 1 μm) on Si substrates as a function of the homologous temperature. All curves are taken from the second stress–temperature cycle. 52

3-2 Simulated stress–temperature hysteresis of a thin film on an elastic substrate subjected to a kinematic hardening constitutive law with strong strain hardening and a temperature dependent yield strength. 58

3-3 Stress–temperature hysteresis of a 1 μm thick Al film on a Si substrate thermally cycled between room temperature and 300 °C. The solid lines represent the elastic response of the film from Eq. (3.6). 59

3-4 Stress–temperature hysteresis of a 1 μm thick Al film on a Si substrate thermally cycled between the several minimum cooling temperatures and 300 °C. The four minimum cooling temperatures are 110, 50, 20 and -10 °C. The solid lines represent the fitting of the constitutive law with Eqs. (3.3) and (3.10), combined with (3.4) and (3.9). The best fit yields n=0.4, σ^*=190 MPa, and T^*=1100 °C. The dashed line represents the temperature-dependent yield strength of the film. 61

4-1 Plane view of TEM micrograph of a 1 μm thick polycrytalline Al film on a Si substrate. 69

4-2 Micrographs of (a) the patterned lines of polycrystalline Al on a Si substrate, and (b) a series of indents at the center of the top surface of 3 μm wide Al line. The maximum depth of indentation was 500 nm to demonstrate large indents. All indentations were oriented in the same way with respect to the line direction. 70

4-3 Load-displacement (P–h) response of two diamond indenters on a quartz specimen in log-log scale. Solid lines represent Eq. (4.1) with different tip radii. 71

4-4 A typical load-displacement (P–h) response of a continuous Al film of 1 μm thickness in normal scale (a) and in log-log scale (b). The predictions for elastic indentation responses with a spherical tip (Eq. 4.1) and an elasto-plastic response with a sharp tip are also plotted. 73

4-5 Statistical distributions of indentation depth at 100 and 200 μN indentation load for polycrystalline Al thin film of 0.33, 0.7, and 1.0 μm thicknesses. Each set of experiments contained 50 indentations. The mean penetration depths of indentation h_{mean} are indicated near the normal distribution curves, which are denoted by the solid lines. 75

4-6 Penetration depth as a function of film thickness of continuous Al films subjected to 100 and 200 μN indentation loads. The error bars indicate ± 1 standard deviation in penetration depths of 20, at least, indentations. . . . 76

4-7 Load-displacement (P–h) responses of polycrystalline Al thin film and lines of 1.5, 3.0, and 5.0 μm line widths. The solid line denotes the elastic response on aluminum of a spherical diamond indenter with the tip radius $R = 500$ nm. 77

4-8 Statistical distribution of indentation depth at 100 and 200 μN indentation load for polycrystalline Al thin film and lines with 1.5, 3.0, and 5.0 μm line widths. The mean penetration depths of indentation h_{mean} are indicated near the normal distribution curves, which are denoted by the solid lines. 78

4-9 Load-displacement (P–h) responses of polycrystalline Al thin film and lines of 2, 3, 4, and 5 μm line widths with a sharp indenter tip. The maximum load is fixed as 1 mN, and the film and line thickness are the same of 1 μm. 79

4-10 Indentation depth as a function of line width for 100 μN and 200 μN indentation loads. The error bars indicate ± 1 standard deviation in penetration depth of indentation experiments. 80

4-11 Simulated load-displacement (P–h) responses of Al thin film and lines using the general purpose finite element package ABAQUS [97]. The indenter was a sharp conical rigid indenter with the included half angle of 70.3°, and σ_{ys} of film and lines is assumed to be 300 MPa. The arrows denote the load levels in Fig. 4-10. 83

4-12 Schematics for a discrete dislocation model, (a) Geometrical configuration of the indenter and patterned line, and (b) Deformation of the cross sectional plane (shaded area in (a)) by the glide of dislocations along the slip planes. 85

5-1 Computational modeling of nanoindentation. (a) schematic of a conical indenter with a sharp tip (left side) and a round tip (right side), where θ is the included half angle of indenter, a and R are the contact radius and tip radius, respectively. Detailed illustrations of mesh design near the indenter tip for the continuous films (b), and for the patterned lines (c) on substrates. 92

5-2 Simulated load-indentation depth (P–h) response of 1 μm thick Al films on Si substrates and bulk counterparts with the same yield stress. A typical experiment of a 1 μm thick Al film on a Si substrate is also plotted. 93

5-3 Simulated P–h response of 1μm thick Al films on a Si substrate with various tip radii. The yield stress of films is the same of 300 MPa. 95

5-4 Simulated P–h response of continuous film and patterned lines of 2, 3, 4 μm width on a Si substrate. Thickness and yield stress of film and lines are the same of 1 μm and 300 MPa, respectively. 96

5-5 Effect of tip radius on the simulated P–h response of continuous film and patterned line of 2 μm width on a Si substrate. Thickness and yield stress of film and lines are the same of 1 μm and 300 MPa, respectively. 97

5-6 Effect of yield stress on the simulated P–h response of continuous film and patterned line of 2 μm width on a Si substrate. Film and line thickness is 1 μm, and the tip radius is 100 nm. 97

5-7 Load-displacement (P–h) response of continuous film of 1 μm thickness on a Si substrate in the log-log scale. Dashed lines indicate the analytical elastic P–h responses of spherical indentation from Eq. (4.1) with various tip radii, and solid lines indicate the elastic-plastic FEM simulations with spherical tips. Symbols represent two experimental indentation responses with two different tip radii. 99

5-8 Mises stress and deformed surface profile around indenters with different tip radii as a function of the distance from the indentation axis at a fixed indentation load of 100 μN. 100

5-9 Load-displacement P–h response of continuous film and patterned lines. Symbols are experiments with a relatively sharp tip, and lines are FEM simulated response with tip radius of R=100 nm on a continuous film and a 2 μm wide patterned line on a Si substrate. 101

5-10 Short-range interatomic potential with equilibrium separation distance r_o = 0.9. Both the potential-well depth and cut-off distance are set to unity and serve as normalizations of energy and length, respectively. 105

5-11 Effect of film thickness on the MD simulated nanoindentation responses. The indenter radius is 29 in reduced units. 107

5-12 Effect of line width on the MD simulated nanoindentation responses. All units are in reduced unit. Thickness of film and lines are 185 and the indenter radius is 29, respectively, in the reduced unit. 109

5-13 Effect of tip radius on the MD simulated nanoindentation responses. All units are in reduced unit. The simulations are conducted on a film and lines of two widths with the tip radius of $R = 29$ and $R = 87$ in the reduced units. Film and line thickness are the same of 185 in the reduced units. 110

5-14 MD simulated load-displacement (P–h) responses of 3-D Cu crystal comprising 90,000 atoms. A sphere of 0.4 nm radius indents normal to the {111} plane of the defect-free crystal of Cu. The simulation size is 8.85 nm×9.39 nm×12.78 nm. The displacement rate of the indenter is 12 m/s. 112

5-15 Defect structures underneath indenters for (a) the film case and for (c) line case at a load of 0.3 μN (denoted as points A and B in Fig. 5-14). (b) and (d) are the rotated views of (a) and (c), respectively, to reveal features on the top and side wall surfaces. In both cases, $x = \langle 11\bar{2}\rangle$, $y = \langle 111\rangle$, $z = \langle 1\bar{1}0\rangle$.114

5-16 Schematics of dislocation configuration during the initial stage of indentation for a bulk material, and a film and a line on a substrate. 116

A-1 Images of deformation around ultra-fine-scale indents. (A) AFM illumination mode image (5 μm$\times$5 μm) of an indented impression after a 60 mN maximum load. The characteristic circular patterns around the triangular indent impression constitute "pile-up", which represents overlapping layers of displaced material. Similar patterns also can be found along the pyramidal faces of the indent. (B) Bright field TEM image of an indented impression after a 20 mN maximum load. It also shows the same circular patterns around the triangular indent hole in a thin foil. 130

A-2 Dark field TEM images of indents with nanocrystallites and their corresponding SAD patterns. The maximum applied load for these indents was 20 mN. (A) SAD pattern obtained from a region of indent beneath the indenter tip and dark field TEM image constructed using a diffracted spot in the SAD pattern. Since the thickness of the TEM foil directly beneath the indent impression is only slightly greater than the maximum penetration depth of indenter ($\sim$ 400 nm) and since the electron beam can transmit only near the indent tip region, we are able to see the region beneath the indenter tip (or the central region of the indent) in this image. The dark field shows a few groups of clustered nanocrystallites inside the indent, as indicated by the arrows. (B) Dark field TEM image obtained from an indented triangular hole and SAD patterns obtained in a region located at a small distance outside of the indent (bottom right) and from the indent (bottom left and schematic). In the dark field image, the arrow indicates clustered nanocrystallites at the edge of dark triangular zone, which is a hole made by the backside thinning through the indent impression. Six spots around transmitted beam in the schematic are analyzed and are found to be associated with the (111) plane of tetragonal Zr_2Ni (space group I4/mcm, a = 6.49 Å, c = 5.28 Å). Halo rings of the bottom right SAD pattern without spots indicate fully amorphous structure of metallic glass in a region that is not affected by the indentation. 131

A-3 Atomic force microscope analysis after 60 mN maximum load. (A) AFM height mode image (5 μm$\times$5 μm) of an indent. We also see the characteristic circular patterns around such indent again, and the colored height information around the triangular indent reveals both large material pile-up at the perimeter of the indent and overlapping layers of severely displaced materials. (B) Cross sectional profile of the indent, along the green line of Fig. 3A, showing the surface uplift along one side to be as much as 150 nm above the reference surface. This large pile-up height around the perimeter of the indent, compared to the penetration depth (720 nm), indicates that the severity of plastic flow around this region during indentation. 132

B-1 Scanned profile of patterned lines by WIRESCAN software. The arrow indicates the center of a line. 135

List of Tables

2.1 Experimentally measured and calculated dislocation densities of passivated thin polycrystalline Cu films on Si substrates at room temperature after cooling from 600°C. All data in the table, except the predictions from Eq. (2.8), are taken from Keller *et al.* [22] 49

3.1 Bauschinger effect parameters for a 1 μm thick Al film on a Si substrate with different pre-strains (minimum cooling temperatures). σ_m is the maximum stress in the forward strain. 61

5.1 Conditions of molecular dynamics simulation for 2-D crystals. 106

Chapter 1

Introduction

For the past several decades, the information revolution has been led by significant achievements in microelectronics technology. Materials-related aspects associated with this revolution have focused primarily on the non-mechanical, functional performance of devices, e.g., their electrical, magnetic, or optical properties. Most of these applications do not rely primarily on the mechanical load bearing capacity of the underlying materials. Consequently, mechanical characterization of the constituent materials has often been neglected. However, It is now widely recognized that mechanical stress and its consequences are central factors in the fabrication, performance and reliability of microelectronic devices [1, 2] and an understanding of the related phenomena is essential for improving reliability and funtionality of those devices [3, 4].

With ever-continuing miniaturization, the microelectronics industry has accelerated its move towards faster and more densely integrated circuits through the reduction of device and interconnect line dimensions (increases in spatial density of individual devices), and through the incorporation of new classes of materials and device structures. Fabrication of these Ultra Large Scale Integration (ULSI) devices involves increasing numbers of deposition and etching stages. Even such devices without direct structural applications are subjected to large mechanical stresses that result from various processing conditions, such as deposition rate and temperature, thermal cycling, presence of surrounding layers, and other geometrical constraints [5, 6]. These processing conditions also influence the

structural evolution of constituent materials [7, 8], which is associated with the evolution of stress states in the materials. The material structures of those devices are subjected to various thermal and mechanical stresses during applications as well as manufacturing processes. Consequently, these stresses affect not only device functionality, but also material and device failure mechanisms, including electromigration [9–11], voiding [12, 13], and passivation cracking [14–16]. This causal relationship between processing/operational stress and device failure is one of the major reasons for the numerous investigations currently underway to accurately determine the stress state and deformation behavior of these structures [3]. Recent developments in Micro-Electro-Mechanical Systems (MEMS), which facilitate integration of mechanical and electrical performance within small structures on a single chip, have increased the need for understanding the mechanical behavior of small structures [17].

Furthermore, the basic geometrical structures of the materials in those applications are thin films or patterned features of thin films such as lines and dots. Compared to typical structural applications, the length scales involved are very small (typically on the order of 1 μm) in a given dimension. We refer to such structures, with at least one dimension in the range of 10 nm to few μm, as *small-volume structures*. These small length scales present another challenge in the experimental characterization and understanding of these materials in terms of their mechanical behavior. Metallic materials in small-volume structures exhibit strong size dependence in their mechanical behavior over a length scale which covers dimensions on the order of 1 μm. Since elastic deformation is a reversible process, and is governed by Angstrom scale (10^{-10} m) interaction parameters such as the interatomic potential and crystallographic lattice orientation, elastic deformation of materials exhibits virtually no size dependence unless a large population of pre-existing defects is involved [18]. Conversely, it has been established that physical and microstructural length scales exert a strong influence on the plastic deformation behavior of materials, as a consequence of the coupling between two competing size parameters [19]: the fundamental length scale of the physical phenomena involved (*e.g.*, the mean free path and distance among dislocations, in the case of plasticity) and the structural dimensions of the material (*e.g.*, grain size, film thickness, and line width). The plastic deformation response, which occurs as a result of the generation, annihilation, and motion of defects such as dislocations, displays marked

size effects when those material dimensions are on the order of 1 μm. Thus, the deformation models developed for bulk materials are inadequate, and the properties of these small-volume structures cannot be characterized by conventional plasticity theories because these theories incorporate no material length scale and predict no size effect. For example, thermally induced stresses of thin metallic films on substrates can reach several hundreds MPa, which is a factor of three to ten higher than the typical flow stress of their bulk counterparts [2, 20–22]. The level of stresses depends not only on the microstructural dimension (grain size) of materials as bulk materials do, but also on the physical dimension of structures (film thickness and line width).

It is relevant to mention that the length scales in small-volume structures are also comparable with other characteristic physical lengths such as the mean free path of electrons or phonons and the size of magnetic domains. Therefore, the electrical and thermal transport properties [6, 23, 24] and magnetic properties [25] of small-volume structures also depend on the physical dimensions of material structures. In addition, other defects, such as grain boundaries, free surfaces, and interfaces, play a more significant role in the small-volume structures due to the relatively large volume fraction occupied by those defects with decreasing dimensions of structures.

The controlling mechanisms of plastic deformation in metallic materials, as well as the size dependence of this deformation, have been topics of long-standing scientific interest [19]. In addition, the technological relevance of this issue as it relates to microelectronic thin films has generated a large research effort over the last decade [2, 3]. The characterization of mechanical behavior on this small scale presents new and significant experimental challenges. In some cases, the principles of macroscopic testing can be transferred directly to small dimensions, as for instance in micro-tensile or nanoindentation testing [26]. However, innovative means of measuring forces and strains in small volumes are often required. In fact, current micro- and nano-scale experimental capabilities far exceed our interpretations of experimental observations. For example, the fundamental mechanisms responsible for the experimentally observed discrete deformation processes under nano-scale contact loading are still debated in the literature [27–30]. At present, the polycrystalline thin metal films and their patterned features are the most important small-volume structures because of the their applications in electric, optical, magnetic, and MEMS devices [6, 17, 31]. In ad-

dition, although the patterned features of thin films, which exhibit additional length scales, are more commonly encountered in practice than continuous thin films, we have very limited knowledge of the deformation mechanisms and properties unique to these structure. Many scientific issues have not been unresolved even in the mechanical properties of thin film systems.

The main objective in this thesis work will be the utilization of analytical, experimental, and computational tools by which the time-independent inelastic deformation of small-volume structures, such as thin films and patterned lines on substrates, can be investigated, and by which the effect of length scales on deformation can be understood. The approach adopted will include systematic experimental and theoretical investigations of the stress states and deformation behavior of metallic materials comprising small-volume structures. Experiments focus on continuous Al thin films and patterned Al lines on Si substrates; including the stress evolution of Al thin films on Si substrates via curvature measurements during various thermal excursion cycles, and systematic nanoindentation experiments on thin films and patterned lines on Si substrates. Theoretical and computational simulations are also conducted to identify the effect of size scales and fundamental mechanisms. Together, these analyses give insight into the origin of size effects on the mechanical properties of these materials. The thesis is organized in the following manner:

- Chapter 2 presents an analysis of the effects of the thickness and grain size of polycrystalline thin metal films on substrates, with the objective of linking the stress evolution of thin films to the underlying characteristic size scales. A model, based on energy minimization of the material system, is proposed on the basis of the premise that the relaxation of mismatch strain in the film is accommodated by the introduction of dislocation loops whose population, dimensions and interaction energies are controlled by the film thickness and microstructural dimensions.

- Chapter 3 addresses the stress hysteresis loops that arise in a thin Al film on a Si substrate. The stress evolution of an Al film is measured as a function of temperature via curvature measurements. The characteristics of the stress–temperature hysteresis, particularly the hardening behavior and the Bauschinger effect, is evaluated by recourse to the change in minimum cooling temperature during thermal excursions.

A phenomenological constitutive law governing the stress–temperature curve is also developed.

- Chapter 4 presents a systematic experimental study of nanoindentation on continuous films and unidirectionally patterned lines of Al on Si substrates to explore the effects of two length scales (film thickness and line width) on the indentation load–displacement (P–h) response. The observed experimental trends exhibit a strong size dependence, which cannot be rationalized on the basis of continuum concepts and suggest a significant role of discrete dislocations in the inelastic deformation mechanism.

- Chapter 5 considers the simulation of nanoindentation of continuous films and patterned lines on Si substrates through the finite element method (FEM) and molecular dynamics (MD) calculations. By correlation with the experimental observations of the previous chapter, possible mechanisms responsible for those size effects are discussed.

- Chapter 6 presents a summary of conclusions and discusses prospects of future work.

- In same situations, nano-scale mechanical contact can also leads to structural changes and phase transformation. An example of amorphous to crystalline phase transformation during active deformation induced by nanoindentation is described in Appendix A.

Chapter 2

Size Effects on the Mechanical Properties of Thin Polycrystalline Metal Films on Substrates

An analysis of the effects of the thickness and grain size of polycrystalline thin films on substrates is presented with the objective of linking the film mismatch stress to the underlying characteristic size scales. The model is predicated on the notion that the relaxation of mismatch strain in the film is accomplished by the introduction of dislocation loops whose population, dimensions and interaction energies are controlled by the film thickness and microstructural dimensions. The model is capable of capturing the combined effects of these size scales by accounting for the interaction energies of the constrained dislocation structure, and provides quantitative predictions of the evolution of film stress during thermal excursions. The predictions of the analysis are compared with available experimental results for polycrystalline films of face-centered cubic materials on Si substrates. It is shown that the model correctly predicts the observed influence of film thickness and grain size on stress evolution during thermal excursions. Aspects of strain hardening in thin polycrystalline films with high dislocation densities are also discussed.

2.1 Introduction

The physical dimensions of thin-film materials are generally comparable to the characteristic microstructural length scales which strongly influence their mechanical properties [19]. The mechanical behavior of thin films has also become an important technological issue in such applications as microelectronics, integrated optoelectronics, data storage, and Micro-Electro-Mechanical Systems (MEMS). In many cases, the reliability and performance of such devices are strongly influenced by their mechanical properties. It is now well known that the mechanical properties of thin metal films can be substantially different from those of their bulk counterparts [3, 5, 6, 32]. Specifically, the flow stress of thin films can exceed that of bulk materials of the same composition and grain size by as much as a factor of three to ten. For example, a 1 μm thick Al film on a relatively thick Si substrate can withstand up to 200 MPa prior to plastic yielding in tension at room temperature [2], whereas the yield stress of pure bulk Al is about 70 MPa. Prior studies, to be reviewed later in this section, have sought to provide a rationale for the observed high strength of thin films, vis-à-vis bulk materials, by invoking mechanisms of constrained dislocation motion within the film or the grain. However, accurate quantitative predictions of film stress evolution during large temperature changes, in terms of the film geometry and microstructure, are presently unavailable.

There exists a large body of experimental evidence which suggests that the coupling of various length scales influences the plastic response of film-substrate systems in a complex manner. Blakely [33] reported that the tensile stress–strain behavior of monocrystalline and polycrystalline gold films was very similar, suggesting that the microstructural size effect was not an important factor in thin-film strength. However, more recent and systematic experiments [20–22, 34] indicate that both the grain size and the film thickness have a marked influence on the strength of thin films. Murakami [20] studied the effect of film thickness and average grain size on strain relaxation due to the thermal mismatch using X-ray diffraction of thin Pb films on Si substrates. The residual strains after strain relaxation, directly related to stress states of thin films, were inversely proportional to both thickness and grain size. Murakami also assumed that dislocation glide was the dominant strain relaxation mechanism in the thin film system. Venkatraman *et al.* [21] measured, by

monitoring changes in substrate curvature, stress variations with temperature as a function of film thickness, for a fixed grain size, in pure Al and Al–0.5% Cu films on Si substrates. They found that the film strength varied inversely with film thickness, and examined their results in the context of the classical Hall-Petch relationship for the effect of grain size on strength:

$$\sigma_y = \sigma_o + Kd^{-1/2}, \tag{2.1}$$

where d is grain size and σ_o and K are empirical constants. Venkatraman *et al.* found that the value of K to be slightly greater for the Al thin films as compared to bulk Al, and that the data for thin films followed a d^{-1} variation instead of the $d^{-1/2}$ functional form for bulk materials. More recently, Keller *et al.* [22] showed that the grain-size dependence of strength in Cu thin films on Si substrates followed a Hall-Petch type relation. They also sought an alternative explanation for thin-film strengthening in the Cu–Si system with a superposition of the strain hardening effect by incorporating the increase in dislocation density with grain size reduction.

The effect of film thickness on the flow stress has been modeled [32] by considering the movement of a single threading dislocation that sweeps across a slip plane of the film. Such models invoke the assumption that when a single crystalline thin film, attached to a rigid and comparatively thick substrate, is subjected to a stress along the in-plane direction of the film, dislocations are generated which subsequently glide to relax the film stress. The minimum shear stress (τ_y) on the slip plane along the slip direction which is necessary to initiate yielding by dislocation glide is expressed as:

$$\tau_y \approx \frac{\mu_f b \cos\phi}{h_f}, \tag{2.2}$$

where μ_f is the shear modulus of the film, b is the magnitude of the Burgers vector, h_f is the film thickness, and ϕ is the angle made by the inclined slip plane with the plane of the film/substrate interface. In this expression, the obstacles which pin the dislocation are the film/substrate interface and the native oxide layer formed on the film. However, this simple equation significantly underestimates the yield stress of thin films. (For a thin pure Al film of 1 μm thickness, it predicts that τ_y is less than 10 MPa.)

Following the analysis of threading dislocations by Freund [35, 36], Nix [2] developed a model that incorporates the effect of thickness on the strength of thin films on substarates. This model is based on the balance between the work done by external stress on the gliding dislocation along the slip plane of the film and the stored energy in interfacial misfit dislocations. The critical biaxial stress required to generate the unit length of misfit dislocation is given by:

$$\sigma_{\text{flow}} = \frac{\sin\phi}{m}\left\{\frac{\mu_{\text{eff}} b}{4\pi(1-\nu_{\text{f}})h_{\text{f}}}\right\}, \tag{2.3}$$

where m is the Schmid factor, ν_{f} is Poisson's ratio of the film, and μ_{eff} is an effective shear modulus which takes into account the effect of the substrate and native oxide (or passivation layer) on the line tension of the interfacial dislocations. μ_{eff} is defined as:

$$\mu_{\text{eff}} = 2\left[\frac{\mu_{\text{f}}\,\mu_{\text{s}}}{\mu_{\text{f}}+\mu_{\text{s}}}\ln\left(\frac{\beta_{\text{s}}h_{\text{f}}}{b}\right) + \frac{\mu_{\text{o}}\,\mu_{\text{s}}}{\mu_{\text{o}}+\mu_{\text{s}}}\ln\left(\frac{\beta_{\text{o}}h_{\text{o}}}{b}\right)\right]. \tag{2.4}$$

Here, h_{o} is the thickness of oxide on the film, μ_{f}, μ_{s}, and μ_{o} are the shear moduli of the film, substrate, and oxide, respectively, and β_{s} and β_{o} are constants on the order of unity. If an oxide or passivation layer is not present, then the second term on the right-hand side of Eq. (2.4) is omitted.

Equation (2.3) predicts that the flow stress of the film is proportional to the inverse of film thickness. This thickness dependence of flow stress is supported by experimental results for large-grained and relatively thick ($\geq$1 μm) films. For example, the calculated stress values from Eq. (2.3) agreed well with experimental results of coarse-grained Al films on Si substrates, in which grains were enlarged by the laser reflow method [37]. However, the experimental results from polycrystalline Al and Cu films of typical grain size were significantly higher than the predictions from Eq. (2.3): for a film of 1 μm thickness, the predicted stresses are 23 and 45 MPa for Al and Cu films, respectively, while the corresponding experimental results are 200 and 280 MPa, respectively. Nix [38] incorporated strain hardening into the above model, considering the elastic interaction of a moving threading dislocation with an array of obstacle dislocations already present at the film/substrate interface. As the number of obstacle dislocations increases with strain, the elastic strain field in front of the moving dislocation, which inhibits the advance of the moving dislocation, increases

substantially. This results in the increase of the flow stress (by decreasing of effective thickness of the film) as the strain increases. Although this mechanistic model is reasonably suitable to predict the experimental results for thin films with large lattice resistance and low dislocation densities, such as hetero-epitaxial films of semiconducting covalently bonded materials, the predicted stresses do not agree well with experimental results in the case of metallic thin films, where lattice resistance is negligible and high dislocation densities are commonly observed. In addition, the film stress is only a function of the elastic properties of the film–substrate system in Eq.(2.3); as a result, explicit variations in film mismatch strain and microstructural length scales are not easily analyzed by this approach.

Grain size is a particularly important microstructural constraint and relevant length scale in polycrystalline thin films. During normal grain growth, film grain size is usually limited by film thickness [39]. The grains often extend through the thickness of film with a preferred orientation thereby developing a columnar grain structure. The discrepancy between experiments and the predicted strength values has been reduced by linearly superposing a grain-size effect, such as the classic Hall-Petch relation, with Eq. (2.3). Thompson [40] extended Eq. (2.3) to include the deposition of dislocations at grain boundaries, creating an additional term to account for the grain-size effect on film stress:

$$\sigma_{\mathrm{gb}} = \frac{2}{m}\frac{\mu_{\mathrm{f}} b}{4\pi(1-\nu_{\mathrm{f}})d}\ln\left(\frac{d}{b}\right), \tag{2.5}$$

where d is the grain size. This suggests a d^{-1} dependence of strength rather than the classical $d^{-1/2}$ dependence, which was noted by Keller *et al.* [22] in their study of Cu films. However, such grain-size dependence of film stress has not been validated by systematic experiments.

A comparison of available experimental results with the predictions of the aforementioned models for thin-film strengthening reveals that while the models qualitatively capture the general experimental trends of the effects of film thickness and grain size on the flow stress, they substantially underestimate the magnitude of the flow stress in most cases. This discrepancy is not surprising because these models consider only the movement of a single dislocation, ignoring the interaction between dislocations. In addition, although stresses are limited by the thermal mismatch strain during thermal excursion, these models

overestimate the stresses for very thin films due to the simple linear relation of $1/h_f$ in Eq. (2.3). Finally, since the only temperature dependence on mechanical response in these models arises from the weak temperature-dependence of elastic modulus, they are ill-suited to account for the large variation of stress and plastic properties with temperature throughout the thermal cycle.

In this chapter, a simple model for the strengthening of thin polycrystalline films subject to a thermal mismatch strain is presented. Instead of a single dislocation or dislocation loop, arrays of circular dislocation loops, which are equally spaced and confined within the slip planes of a grain, are considered. The generation of each dislocation loop in the set consecutively relaxes the elastic thermal strain, which arises from thermal mismatch between the thin film and the substrate during thermal cycling. With this simplified model, the total energy of system as the sum of the energies stored in dislocation loops, the interaction energies among the loops, and the elastic energy of the grain can be evaluated. By minimization of the total energy of the system, time-independent equilibrium strains that are sustained by the metal film are calculated and converted to stresses. This approach allows us to describe stress evolution in films as a function of their thickness, grain size, and thermally induced strain (or equivalently, temperature). The predictions of the model are found to agree well with available experimental data for Al and Cu films. The interaction energies among the dislocation loops is shown to play an important role in stress evolution of the thin film.

2.2 Analysis

When a single-crystal film is deposited on a substrate with a different lattice spacing, misfit dislocations form at the film/substrate interface when the film thickness exceeds a critical thickness. Matthews [41] developed a model to predict the critical thickness of the thin epitaxial layer on the substrate by minimizing the total energy in the layer with respect to the elastic strain due to the lattice mismatch between the film and the substrate. The total energy of the system, which is minimized at equilibrium, is the sum of the elastic strain energy and the misfit dislocation energy.

Based on similar energetic considerations, we can develop a model to evaluate the equilibrium elastic strain that can be sustained in a polycrystalline thin film on a substrate. The model assumes that dislocations or dislocation loops are generated in response to a uniform elastic strain. The total energy of the system can be described as the sum of two parts: the energy associated with the uniform elastic strain in the film (E_{elastic}) and the energy associated with the elastic strain fields of dislocations (E_{disl}):

$$E_{\text{total}} = E_{\text{elastic}} + E_{\text{disl}} \ . \tag{2.6}$$

Note that if the substrate is much thicker than the film, then it experiences a much lower in-plane stress than the film. Therefore, we make the usual approximation that all of the strain energy is accommodated by strain in the film, rather than in the substrate. We further assume that the polycrystalline thin film has a preferred texture normal to the film surface, but is of random in-plane orientation; the in-plane properties can then be considered isotropic. If we denote the in-plane quantities by the symbol '$\|$' and out-of-plane quantities by the symbol '$\perp$', the elastic energy, E_{elastic} in a single grain of thin film under the equibiaxial strain state is given by:

$$E_{\text{elastic}} = \frac{1}{2}\left(2\sigma_{\|}\varepsilon_{\|} + \sigma_{\perp}\varepsilon_{\perp}\right) V_{\text{g}} = 2\frac{(1+\nu_{\text{f}})}{(1-\nu_{\text{f}})}\,\mu_{\text{f}}\varepsilon^2 d^2 h_{\text{f}} \ , \tag{2.7}$$

where V_{g} is the volume of a grain, and ε is the equibiaxial mismatch strain to which the film is subjected. Since the film is free to expand out of the plane, $\sigma_{\perp}$ vanishes. The shape of the grains is assumed to be a rectangular prism.

Transmission electron microscope (TEM) observations by Kuan and Murakami [42] of Pb films on Si substrates cooled to −173°C from room temperature indicate that most dislocations glide across the grains along {111} planes that are inclined at an angle of ~70° to the film surface or along {111} planes that are nearly parallel to the film surface. These observations also show that, although the as-deposited Pb film contains very few dislocations at room temperature, a high density of dislocations is introduced in the grains upon cooling, suggesting that dislocations originate at grain boundaries and subsequently glide across the grain. All dislocation motion is confined within each grain by the native

surface oxide, the substrate, and the grain boundaries or twin boundaries. It is also found that most of the dislocation glide events are reversible for a small number of thermal cycles [42]. Dislocations induced upon cooling disappear during heating, and the new dislocations appear and glide on another set of slip planes during subsequent cooling. No tangling of dislocations gliding in the parallel glide planes occurs, and no appreciable increase in dislocation density is observed. Similar dislocation characteristics were also reported by Venkatraman *et al.*[43] for Al–0.5%Cu films on Si substrates which were heated from room temperature to 450°C.

Drawing on the above observations, the dislocation structure in most FCC metal film grains on a substrate is reasonably represented with the idealized schematic shown in Fig. 2-1. The substrate and the native oxide (or passivation) layer on the top of the grain are not shown in the schematic for simplicity. The grain with an arbitrary shape (thin solid lines) is reduced to a parallel prism (dashed line) with a square base. The size of the base and the height of the grain are defined by the effective in-plane grain size and the film thickness. A set of dislocation loops (thick solid lines) are generated at grain boundaries and they spread out across the grain on one of the inclined slip planes. However, in order to evaluate E_{disl} for the system, the details of the dislocation configuration should be considered, including the self energy of different parts of the dislocation loop which result from the different shear moduli of the oxide and the substrate, the image force on those dislocation segments, and the interaction energy of dislocations within a loop and between loops. The number of loops and the size of each loop should also be considered as a function of the applied strain.

Assume that N dislocation loops have glided across the (111)-textured grain and relax a given applied strain ε_{app} (which in the context of thermal cycling represents the thermal mismatch strain, $\varepsilon_{\text{thermal}}$ during temperature excursions) to the equilibrium residual elastic strain ε_{eq}. If the film is not bonded to the substrate (*e.g.*, a free-standing film without a surface oxide), and dislocation loops can sweep the entire grain and make slip steps at the surface of the grain, the amount of strain that each generated dislocation loop can relax is $\varepsilon_{\text{o}} = b'/d$, where b' is the projection of the edge component of the Burgers vector on the film surface (for $\{111\}\langle 110\rangle$ mixed dislocations in a FCC film, $b' = \sqrt{3}\ b/6$). If the film, however, is bonded to a rigid substrate and/or surrounded by its own oxide layer such that the generated loop is constrained from expanding throughout the entire grain, the resulting

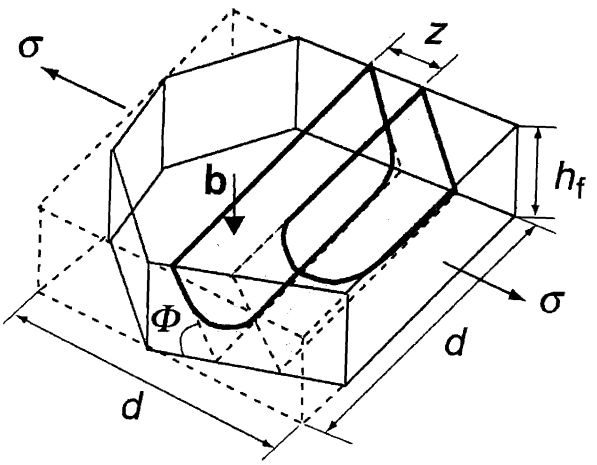

Figure 2-1: A schematic of dislocation loop structure along an inclined slip plane of a grain, where d is the grain size, h_f is the film thickness, z is the distance between loops, Φ is the angle between slip planes and film surface normal, $\mathbf{b}$ is the Burgers vector, and σ is the applied stress, or the film mismatch stress.

strain relaxation due to dislocation glide should be less than that of the free film. The extent of actual strain relaxation would be reduced to $\varepsilon_o = \eta b'/d$, where η ranges from 0 to 1. The correction factor η is expected be a function of the film thickness, the relative orientation of grains in the film plane, boundary conditions at the film/substrate or film/oxide interface, the elastic constants of the film and the substrate, and the dislocation density [42]. The number of dislocation loops generated in the grain is directly related to the extent of strain relaxation for an imposed thermal strain such that

$$N = \frac{(\varepsilon_{\text{thermal}} - \varepsilon)}{\varepsilon_o} = \frac{d(\varepsilon_{\text{thermal}} - \varepsilon)}{\eta\, b'} \,. \tag{2.8}$$

The biaxial stress state of the film would cause the strain to be relaxed by generating two sets of dislocation loops in two distinct directions. Thus, the dislocation energy can be expressed by:

$$E_{\text{disl}} = 2\sum_{i}^{N} W_{\text{self}} + \sum_{ij}^{2N} W_{ij} \,, \tag{2.9}$$

where W_{self} is the self energy of the single loop and W_{ij} is the interaction energy between each dislocation loop in the set.

In order to evaluate the total energy of dislocation loops including the interaction energy, several approximations are made so that a tractable model could be formulated:

(i) Both the film and the substrate are elastically isotropic.

(ii) Image stresses of the edge component of dislocation loops which arise due to the film/substrate and film/oxide interfaces are not considered.

(iii) Dislocation loops are coaxial, circular loops of radius R and uniform separation $z = d/N$.

(iv) The radius of the dislocation loops is an average of the grain size and thickness of the film (for example, $R = (d + h'_{\mathrm{f}})/4$ for the arithmetic average, or $R = \sqrt{dh'_{\mathrm{f}}/\pi}$ for the geometric average, where $h'_{\mathrm{f}} = h_{\mathrm{f}}/\sin\phi$).

(v) The interaction energy between parallel dislocation loops is limited to nearest neighbors.

The self energy and interaction energy of coaxial loops depend not only on loop radius and separation, but also on the direction of their Burgers vector. For two coaxial dislocation loops of the same radius R, with the same Burgers vector that exists in the plane of the loop, and the same sense of dislocation line direction ξ, the interaction energy is given by [44]:

$$W_{\mathrm{inter}} = 2\pi R \frac{2-\nu_{\mathrm{f}}}{2(1-\nu_{\mathrm{f}})} \frac{\mu_{\mathrm{f}} b^2}{2\pi} \left(\ln \frac{4R}{z} - 2 \right), \tag{2.10}$$

where z is the distance between dislocation loops. This equation is valid only when $z \ll R$. The self energy of a circular dislocation loop with a radius R is obtained by setting $z \approx b$ and dividing Eq. (2.10) by a factor of two:

$$W_{\mathrm{self}} = 2\pi R \frac{2-\nu_{\mathrm{f}}}{2(1-\nu_{\mathrm{f}})} \frac{\mu_{\mathrm{f}} b^2}{4\pi} \left(\ln \frac{4R}{b} - 2 \right). \tag{2.11}$$

Combining these energy terms in Eqs. (2.10) and (2.11) with Eqs. (2.8) and (2.9), in conjunction with the above assumptions, the total energy of the system is found to be:

$$E_{\mathrm{total}} = E_{\mathrm{elastic}} + 2NW_{\mathrm{self}} + 2(N-1)W_{\mathrm{inter}}$$

$$= 2\mu\frac{(1+\nu_f)}{(1-\nu_f)}\varepsilon^2 d^2 h_f + \frac{d(\varepsilon_{thermal}-\varepsilon)}{\eta b'}\frac{2-\nu_f}{2(1-\nu_f)}\mu_f b^2 R\left(\ln\frac{4R}{b}-2\right)$$

$$+2\left(\frac{d(\varepsilon_{thermal}-\varepsilon)}{\eta b'}-1\right)\frac{2-\nu_f}{2(1-\nu_f)}\mu_f b^2 R\left(\ln\frac{4R}{z}-2\right). \quad (2.12)$$

For a given thermal strain $\varepsilon_{thermal}$, the equilibrium strain ε_{eq} is the value of strain ε which minimizes E_{total}. The elastic film stress can then be calculated as the product of the film biaxial modulus and the equilibrium strain ε_{eq}.

2.3 Comparison with Experimental Data

In this section, we compare the predictions of the above model with available experimental data for polycrystalline Al and passivated Cu thin films on Si substrates, and ploycrystalline Cu thin films on deformable substrates.

2.3.1 Polycrystalline Al thin films on Si substrates

Venkatraman and Bravman [21] performed a systematic experimental study of the variations of mismatch stress with temperature as a function of film thickness and grain size for Al films on Si substrates. The variation in film thickness for a given grain size was achieved by the repeated, controlled growth and dissolution of an anodic oxide layer on the surface of the Al film. Stress measurements were conducted as a function of temperature using the substrate curvature method.

Figures 2-2(a) and (b) show the effect of film thickness on the flow stress of polycrystalline Al films, with a fixed grain size, as a function of temperature. The effective radius of dislocations loops is evaluated by setting the arithmetic average of the film thickness and grain size ($R = (d+h_f')/4$). While Eq. (2.3) poorly predicts the stress-temperature relation of these thin films, the stresses calculated on the basis of the present model, Eq. (2.12), match the experimental trends well for $\eta = 0.6\sim0.8$. In the case of the 0.98 μm thick Al film, Eq. (2.3) underestimates the experimental flow stress at room temperature by 40 %.

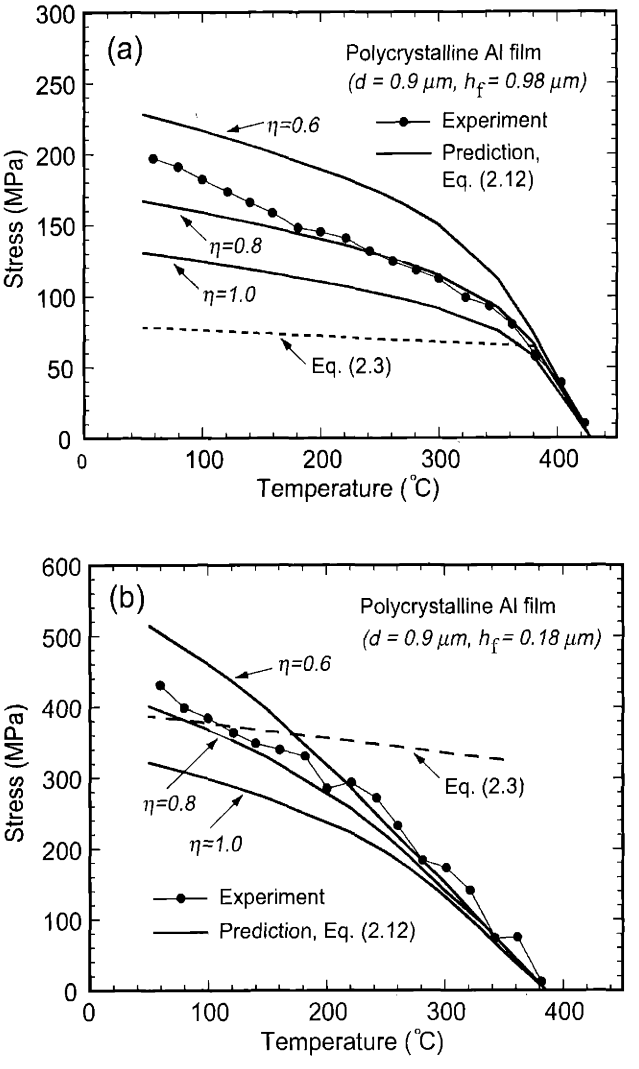

Figure 2-2: Stress evolution in thin polycrystalline Al films on Si substrates during cooling, (a) for d=0.9 μm and h_f=0.98 μm, and (b) for d=0.9 μm and h_f=0.18 μm. Symbols are experimental data from Venkatraman and Bravman [21] , solid lines are calculated from Eq. (2.12), and dashed lines are calculated from Eq. (2.3).

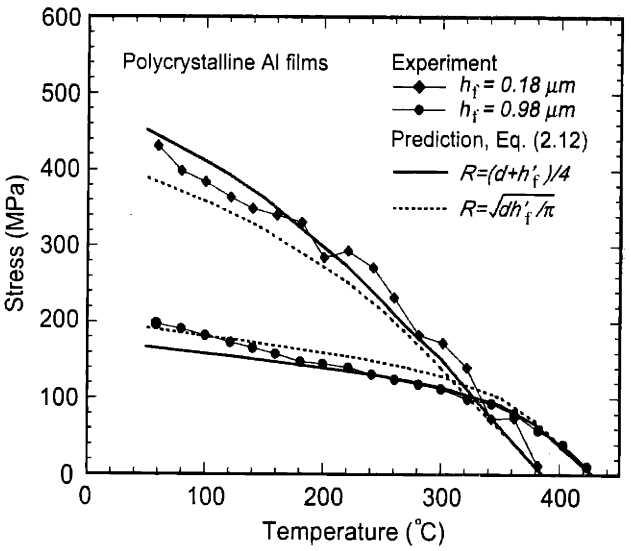

Figure 2-3: Stress evolution in thin polycrystalline Al films on Si substrates during cooling, for h_f=0.98 μm and h_f=0.18 μm for a fixed grain size of 0.9 μm. Symbols are experimental data from Venkatraman and Bravman [21], solid lines are calculated from Eq. (2.12) when $R = (d + h'_f)/4$, and dashed lines are calculated from Eq. (2.12) when $R = \sqrt{dh'_f/\pi}$.

This discrepancy is due to the fact that Eq. (2.3) does not take into account the effect of grain size. In the case of the 0.18 μm thick film, the stresses predicted using Eq. (2.3), especially in the lower temperature regime, are similar to those predicted by Eq. (2.12) and the experimental data. This agreement may be due to the fact that the thickness of the film is relatively small compared to its grain size, so that the assumption of a single crystalline film is better suited for this geometry. However, the temperature-dependence of film stress in Eq. (2.3) is not sufficient to describe the stress evolution during the cooling process.

For both film thicknesses, the correction factor η in Eq. (2.12) which gives the best fit for values is about 0.6~0.8, with the calculated stress at the same temperature increasing with decreasing η. It is noted that these values for η lie within the experimentally measured range. Kuan and Murakami [42] reported that an empirical factor $\bar{f}$, which is similar to the parameter η in the present model, ranged between 0.6 to 1 for 0.2 μm thick polycrystalline Pb films of various grain size upon cooling from room temperature to 100 K. They also estimated a theoretical value for $\bar{f}$ in their system to be ~0.6.

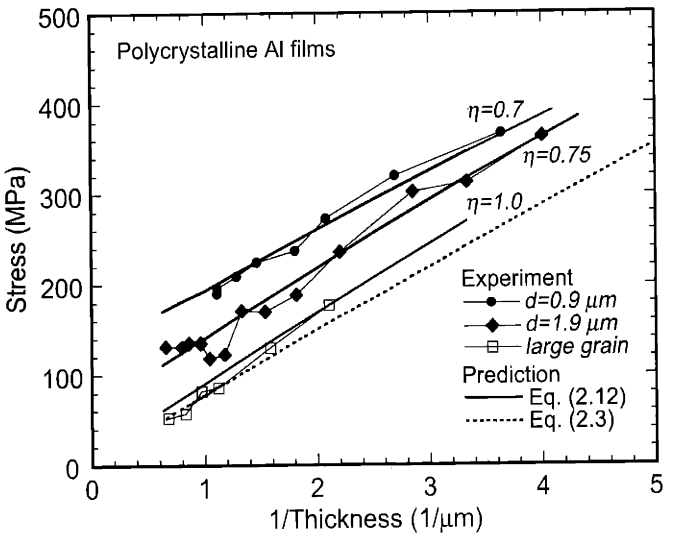

Figure 2-4: Stresses in thin polycrystalline Al films on Si substrates with d=0.9 μm, 1.9 μm, and laser reflowed large grain as a function of film thickness at 60°C. Symbols are experimental data from Venaktraman and Bravman [21], solid lines are calculated from Eq. (2.12), and dashed line is calculated from Eq. (2.3).

The magnitude of stresses evaluated from Eq. (2.12) also depends on the method used to calculate the radius of the dislocation loops. In Fig. 2-3, the estimated stress evolution is presented for two different calculations of R, using the same experimental data as shown in Fig. 2-2. The difference between these two methods becomes significant when the thickness of the films decreases, forcing the actual shape of loops to become more elliptical. This leads to errors in the choice of proper grain shape and consequently, the assumed radius of the loops R fails to represent the length-scale effects well in Eq. (2.12) for cases in which the ratio of film thickness to grain size (h_f/d) deviates substantially from unity.

Figure 2-4 shows the experimentally measured and calculated film stress as a function of film thickness at 60°C, after cooling from about 450°C, for three different grain sizes of Al films. The stresses calculated using Eq. (2.12) are based on the same temperature difference from a stress-free reference temperature (ΔT = 370°C). The effects of thickness and grain size on the strength of thin films are reasonably well predicted by Eq. (2.12) for the choice of η described above; by comparison, the predictions of Eq. (2.3) match experiments

only for the large-grained films. It should be noted that the value of η for a given thickness decreases when grain size decreases. This trend is similar to that shown in Fig. 2-2, which suggests that when either the grain size or thickness of the Al film decreases, the strain relaxation afforded by dislocation glide is reduced. Another important point to note here is that the slopes of the stress vs. inverse film thickness plots in Fig. 2-4 are not the same for 3 different grain sizes; this indicates that the effects of grain size and film thickness on film stress are not independent.

2.3.2 Passivated polycrystalline Cu thin films on Si substrates

Thermal stresses of thin Cu films on Si substrates were examined by Keller *et al.* [22] as a function of film thickness and the presence of a silicon nitride passivation layer. Three different thicknesses of passivated Cu films were examined and the grain sizes of films were measured by TEM. Dislocation densities were also determined at room temperature via X-ray diffraction. Figure 2-5 shows the stress evolution in passivated Cu films of 1.0 μm and 0.45 μm thickness on Si substrates during cooling from 600°C to room temperature. The average grain size for the two film thicknesses was 1.3 μm and 0.83 μm, respectively. The films were passivated with 50 nm of Si_3N_4. This nitride passivation layer limits diffusional creep through the surface and grain boundaries at high temperatures. Thus the passivated Cu films are more suitable for assessing the validity of the present model than unpassivated films that could develop different stress–temperature responses due to the thermally activated processes.

The predicted stress values of Eq. (2.3) clearly underestimate the experimental data for both cases because the film thickness and grain size are comparable. The stresses calculated from Eq. (2.12) correctly predict stress evolution at high temperature in both Figs. 2-5(a) and (b). However, experimental data begin to deviate from predictions of Eq. (2.12) around 200°C, and stresses increase rapidly below that temperature. Similar experimental results were reported by Kobrinsky *et al.* [45] in Ag thin films on oxidized Si wafers. These researchers use *in situ* TEM observations to show that the rapid increase of stress in the low-temperature regime is due to the decreased thermal energy to overcome the barrier of the dislocation glide through forest dislocation obstacles. Since the present model

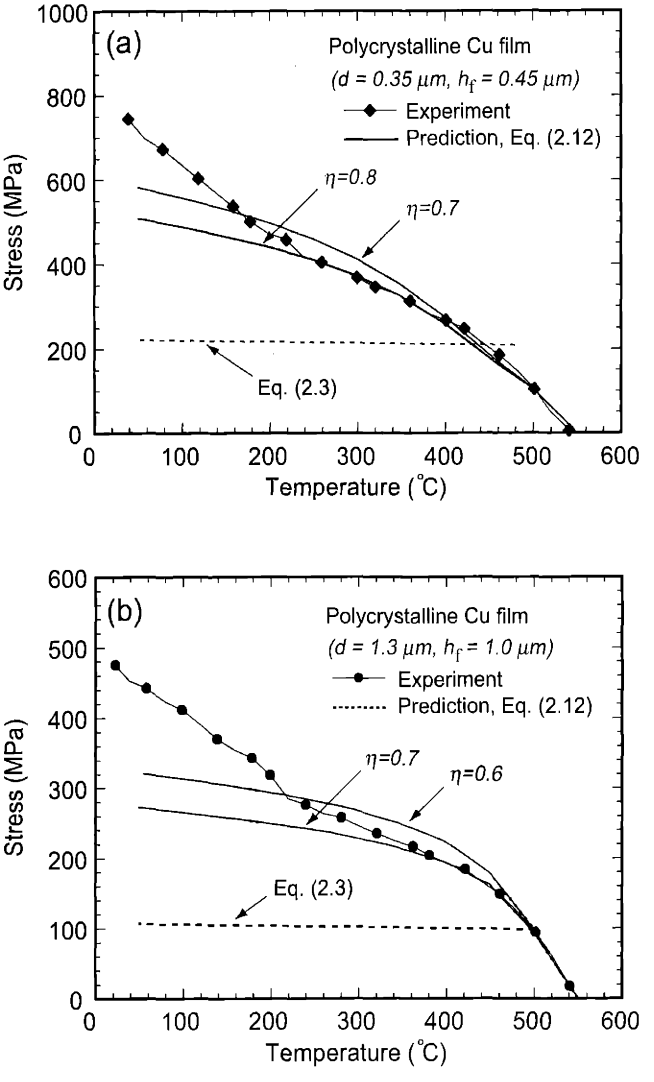

Figure 2-5: Stress evolution in passivated thin polycrystalline Cu films on Si substrates during cooling, (a) for d=0.35 μm and h_f=0.45 μm, and (b) d=1.3 μm and h_f=1.0 μm. Symbols are experimental data from Keller *et al.* [22], solid lines are calculated from Eq. (2.12), and dashed line is calculated from Eq. (2.3).

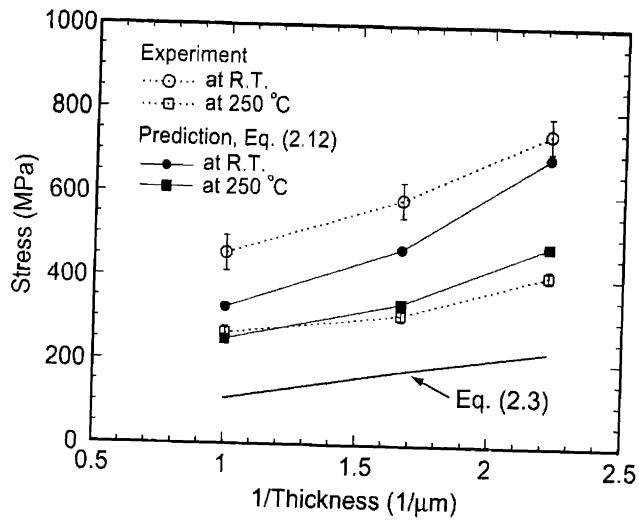

Figure 2-6: Stress at room temperature and at 250°C for passivated thin polycrystalline Cu films on Si substrates as a function of film thickness. Open symbols are experimental data from Keller *et al.* [22], filled symbols are calculated from Eq. (2.12), and solid line is calculated from Eq. (2.3).

uses the equilibrium energy criterion as a necessary condition for dislocation generation, and hence does not consider the energy required to nucleate and propagate dislocations, it can not capture such mechanisms operating at low temperatures.

In Figure 2-6, the experimentally measured and predicted stresses at room temperature and at 250°C are shown for passivated Cu films, cooled from 600°C, as functions of inverse film thickness. At room temperature, the difference between experiments and predictions decreases as the film thickness and grain size decrease. This discrepancy is related to the mechanism transition described above. Above 200°C, the calculated stresses agree well with experiments.

2.3.3 Polycrystalline Cu thin films on a deformable substrate

Hommel and Kraft [46] studied the stress-strain behavior of Cu thin films during microtensile tests as a function of microstructure parameters, such as film thickness (0.4–3.2μm), grain size, and texture. The tensile test was performed at room temperature, and a compliant substrate (polyimide foil) transferred applied strains to the film. The stress of films

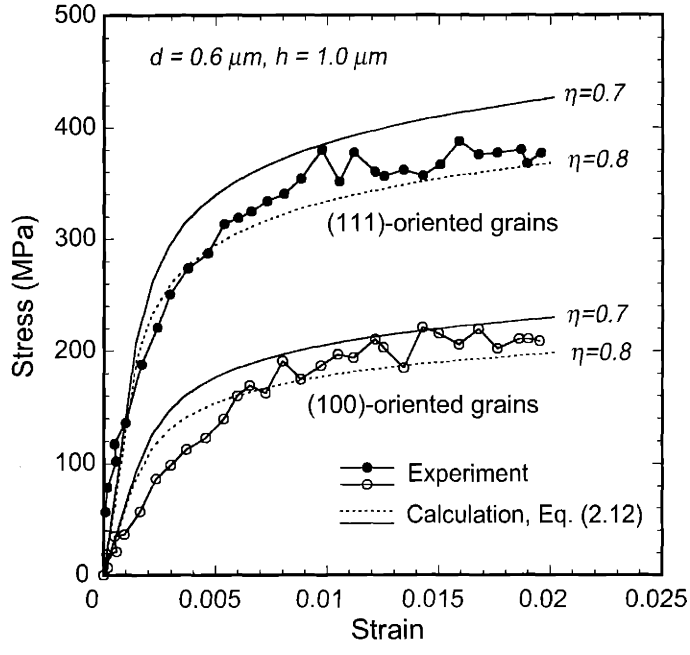

Figure 2-7: Stress–strain behavior of a thin polycrystalline Cu film on a polyimide substrate at room temperature, for h_f=1.0 μm and d = 0.9 μm. Symbols are experimental data from Hommel and Kraft [46]and lines are calculated from Eq. (2.13).

was measured by X-ray diffraction and the macroscopic strains of sample were measured by a laser scanning system. Figure 2-7 shows the stress–strain behavior of the (111)- and the (100)-oriented grains in a 1 μm thick Cu film with a grain size of 0.6 μm on a polyimide substrate. Since strains were applied uni-directionally on the different crystal orientations, Eq. (2.12) was slightly modified:

$$E_{\text{total}} = \frac{M_{hkl}}{2(1-\nu)}\varepsilon^2 + NW_{\text{self}} + (N-1)W_{\text{inter}} \tag{2.13}$$

where M_{hkl} is the biaxial modulus of thin-film crystal with $[hkl]$ texture. The calculated stress from Eq. (2.13) correctly predicted not only the stress levels after yielding but also the difference in the elastic slope due to the large elastic anisotropy in Cu film grains. The theoretical ratio of elastic modulus in (111)- and (100)- oriented films was 2.3 whereas the calculated ratio of that from the predictions was 2.2. For both orientations of grains, the upper and lower limits of experiments were well bounded by the predictions with the correction factor η of 0.7$\sim$0.8.

2.4 Discussion

The dislocation interaction model presented in this chapter describes the stress evolution of a film–substrate system during thermal excursion, as shown through the comparison with experimental data. It also indicates the relative importance of the coupled effects of two length parameters (*e.g.*, film thickness and grain size) on the strength of the thin films. Venkatraman and Bravman [21] and Keller *et al.* [22] analyzed their experimental assessments of film stress with a linear combination of the effects of film thickness and grain size. In order for the linear superposition of these effects to be valid, the relationship between film stress and inverse thickness must be independent of grain size. From Fig. 2-4, it is clear that the variation of stress with thickness is indeed a function of grain size: the variation decreases with decreasing grain size. The reported ambiguity concerning the grain-size dependence of film strength (d^{-1} or $d^{-1/2}$ variation) could arise from a lack of consideration of this coupling.

In Figure 2-8, the calculated residual strains at room temperature after stress relaxation caused by dislocation loop generation are shown for a polycrystalline Al film as a function of inverse film thickness for two values of η, where the film grain size is taken to be equal to film thickness. The system was cooled down from 375°C to 25°C. The residual strain increases with decreasing film thickness and the increase in residual strains seems to be mitigated. For the range of film thicknesses shown here, the residual strain does not reach the value of the imposed thermal strain. This trend was experimentally observed in Pb films on Si substrates by measuring strain relaxation via X-ray diffraction [20, 47]. They showed that the residual strain approached a constant value when the thickness or grain size is reduced below a critical value, and the plateau in the residual strain occurs at a smaller value than the imposed thermal strain; this difference has been attributed to strain relief by grain boundary relaxation. *In situ* TEM experiments of Pb and Al films during thermal cycling [32, 37] also showed that no extensive slip or plastic deformation occurred within extremely small grains, even among different size of grains in the same film to which the same magnitude of thermal strain was imposed. The agreement of the present model predictions with these experimental observations thus suggests that the limited formation and motion of dislocations inside very small grains is responsible for the high flow stress of thin films and high strain hardening as described in Section 2.3.2.

In bulk materials, the increase of yield stress with decreasing grain size is well-known as the Hall-Petch relation [48, 49]. The basic idea of this microstructural length-scale effect is predicated upon the assumption that a dislocation pile-up within a grain can initiate slip across a grain boundary due to the stress concentration at the leading edge of a pile-up. The number of dislocations required to initiate this slip is quite large, and such large dislocation pile-ups have not been observed in thin-film systems [37]. One may expect a transition from this pile-up mechanism to another mechanism as the grain size becomes extremely small, as in the case of nanocrystalline bulk materials [50].

As noted by Keller *et al.* [22] and Kobrinsky *et al.* [45], strain hardening due to the high dislocation density is one of the important sources of thin film strengthening. The model developed in this study accounts for strain hardening as a function of film thickness and grain size by invoking rate-independent flow processes. The calculated stress-strain relation of Al films with different thicknesses, for a fixed grain size, is shown in Fig. 2-

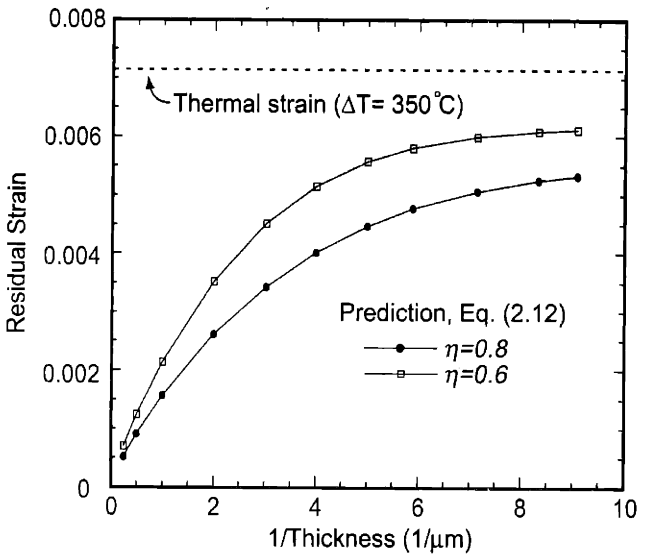

Figure 2-8: Residual strain at room temperature as a function of film thickness in thin polycrystalline Al film on Si substrate for a imposed thermal strain. Grain size is assumed to be the same as the film thickness. Solid lines with symbols are calculated from Eq. (2.12) for η=0.6 and 0.8, and dashed line represents the imposed thermal strain ($\varepsilon_{\text{thermal}}$=0.00714).

9. It is assumed here that the developed thermal strain induced during cooling equals the total strain. It is evident that thinner films show greater strain hardening. If power-law strain hardening is assumed to evaluate the apparent hardening exponent n (from $\sigma = H\varepsilon^n$, $\sigma > \sigma_y$), the hardening exponent becomes 0.23 for a 1.0 μm thick film and its value increases to 0.55 for a 0.2 μm film. We obtained a similar variation in n for different grain sizes with a fixed film thickness. (For a 1 μm thick Al thin film, n becomes 0.26 and 0.52 for grain sizes of 1 μm and 0.2 μm, respectively.) These values of n are significantly higher than that of bulk Al alloy [51]. We believe this high strain hardening in thin metal films is due to the same mechanism previously described, in which the dislocation structure and interaction in thin-film grains are completely different from those in the bulk. For example, an Al thin film of 1 μm thickness and 1 μm grain size, the interaction energy terms become 35%, 69%, and 85% of the self energy terms in Eq. (12) as the total strain increases from 0.0021 to 0.0041 and 0.0062 due to the increase of temperature difference (ΔT).

A model for strain hardening in thin films as an extension of Eq. (2.3), has been

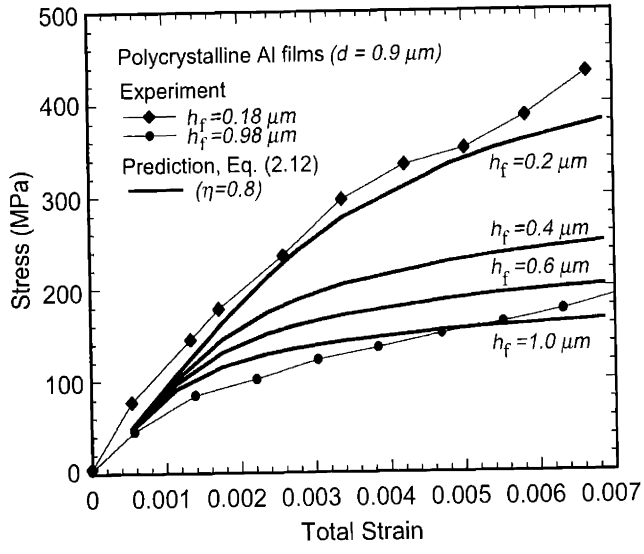

Figure 2-9: Stresses in thin polycrystalline Al film on Si substrate as a function of total strain with different film thicknesses. Grain size, d, is fixed at 0.9 μm. Symbols are replotted from Fig. 2-2, and solid lines are calculated from Eq. (2.12).

proposed [38]. The reduction of effective thickness, resulting from the strain field of pre-deposited misfit dislocation array at the film/substrate interface, generates high strain hardening behavior. However, this requires a large array of misfit dislocations in front of an advancing dislocation, which has thus far not been observed in *in situ* TEM experiments. Furthermore, such a process cannot account for the effect of grain size. The exceptionally high strain hardening exponent ($n \sim 0.5$) has also been observed in a 0.4 μm thick passivated Cu film bonded to a glass substrate [52]. The proposed mechanism is that the high strain hardening is accounted for by strong barriers to inelastic shear, provided by the inhibition of lateral spreading of the shear. This alternative mechanism arises from the limited volume of the confined thin film.

The dislocation density of a thin film can be calculated using Eq. (2.8) and the volume of grain after we evaluate the equilibrium strain ε_{eq} from Eq. (2.12). The calculated dislocation densities of three different passivated Cu films are compared with published experimental results by Keller *et al.* [22] in Table 2.4. The variation of calculated values is caused by the value of η used in Eq. (2.12), which ranged from 0.6 to 0.8. X-ray diffraction was used to determine dislocation densities of the films, and grain size of films were measured by TEM. The calculated dislocation densities are quite high, but smaller

Table 2.1: Experimentally measured and calculated dislocation densities of passivated thin polycrystalline Cu films on Si substrates at room temperature after cooling from 600°C. All data in the table, except the predictions from Eq. (2.8), are taken from Keller *et al.* [22]

Film Thickness (μm)	Grain Size (μm)	Dislocation Density (10^{14} m^{-2})	
		Experiment	Prediction, Eq. (2.8)
1.0	1.3	8.6	5.0∼6.1
0.6	0.83	13.8	7.2∼8.3
0.45	0.35	22.3	10.3

than experimental values. Keller *et al.* determined dislocation densities by an X-ray peak broadening model, which was developed for bulk materials, and assumed the peak broadening originated only from the strain fields around dislocations. Thus the cited experimental dislocation densities should be considered an upper bound of dislocation densities. Since the actual dislocation densities can be smaller than the reported values, the difference of a factor of two between calculated and measured dislocation densities may not be significant. The dislocation densities increase as the film thickness and grain size decrease. The typically reported values of dislocation densities for polycrystalline thin films of face-centered cubic (FCC) metals range from $10^{14} - 10^{15}$ m^{-2} [45], which is in good agreement with our estimates shown in Table 2.1.

2.5 Conclusions

This work has shown a simple way by which the interaction energies among dislocations can be used to rationalize a variety of experimental observations in thin polycrystalline metal films subjected to thermal excursions. The model successfully predicts the overall trends pertaining to the effect of length scale, such as film thickness and grain size, on stress evolution in film–substrate systems. Through comparison of experimental data for Al and Cu films (with different thickness and grain size) on Si substrates, the stress–temperature curves of those films upon cooling from a high temperature could be estimated without considering the possibility of rate-dependent processes such as diffusional creep.

However, thermally activated processes leading to stress relaxation must be taken

into account in order to broaden the scope of this model for those metal films which are not covered by native oxide or effective passivation layer. Nevertheless, the present approach demonstrates the strong coupling between the dependence of film stress on two key length scales: the film thickness and the grain size.

These size effects are closely related to the increased strain hardening behavior of thin-film systems, which is caused by the confinement of dislocation generation and movement within a small volume of grain. Since the model predicts dislocation densities of thin films increase as the film thickness and grain size decrease, strain hardening due to high dislocation densities can be considered as an important source of thin-film strenghening.

The agreement between experiments and predictions of model indicates that the assumed dislocation structure is a plausible model of thin polycrystalline films (with thickness and grain size on the order of 1 μm). This dislocation structure may be chiefly responsible for the unique mechanical behavior of these systems. Although the model developed in this study can give us an insight as to the relations between size parameters and macroscopic mechanical properties, further work, including more detailed microscopic observations of dislocation evolution and glide during thermal cycling, is required to more accurately calculate the energy of dislocation structures and to understand in detail the evolution of the dislocation structure in a thin-film system.

Chapter 3

Stress evolution of an Al thin film on a Si substrate during thermal cycling

The stress evolution of a polycrystalline Al thin film on a Si substrate is characterized during thermal excursion using the kinematic hardening law. Strengthening beyond the initial yield stress occurs upon cooling and heating. The stress–temperature relationship of the Al film can be characterized by a kinematic constitutive law with temperature-dependent yield stress. It is shown that the high strain hardening and Bauschinger effect in thin films are primarily due to the rapid development of high back stresses, the origin of which is discussed in detail.

3.1 Introduction

The mechanical properties of small-volume structures, such as thin films, have been explored with great interest as the feature dimensions of integrated circuit devices continuously decrease. Common failure modes of metallization are stress-controlled processes such as delamination, cracking, void formation and electromigration [9, 10, 12, 15, 16]. The ability to predict the stress state of thin films, subjected to a given set of processing and work-

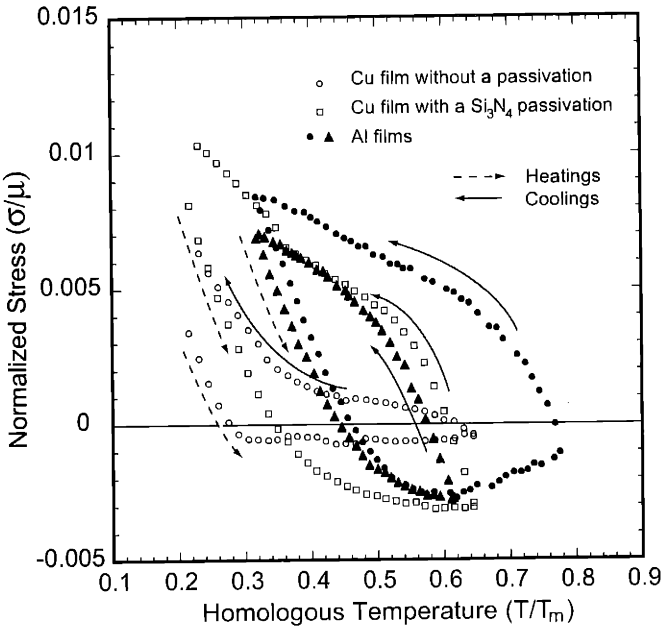

Figure 3-1: Stresses, normalized by the shear moduli (26 and 44 GPa for Al and Cu, respectively), of Cu films (with and without a passivation layer) [55] and Al films (with only a native oxide) [56] of the same film thickness (h_f = 1 μm) on Si substrates as a function of the homologous temperature. All curves are taken from the second stress–temperature cycle.

ing conditions, would prove extremely useful in understanding their failure mechanisms. Unfortunately, however, thin metal films have different dimensional and microstructural constraints than bulk metals do, and often exhibit quite different mechanical behavior [53] (see details in Chapter 2). One of the most popular methods capable of producing reliable quantitative measurements of the mechanical behavior of thin films is thermomechanical stress measurement, which involves subjecting a thin-film/substrate system to thermal excursions. Stresses arising in the film due to the thermal mismatch between the film and the substrate can be determined by measuring the curvature changes of the system. Alternatively, strains in the film may be determined by other methods (*e.g.*, X-ray diffraction) and then converted to stresses [54]. In either case, the resulting stress–temperature curves provide mechanical behavior characteristics that can be used to understand the deformation mechanisms involved.

Typical experimental stress–temperature curves for Al and Cu films on Si substrates [55, 56] are shown in Fig. 3-1. The temperature dependence of stresses is different

for Cu and Al films; Al films are capable of supporting higher stresses at higher homologous temperatures, relative to unpassivated Cu films, which relax stresses rapidly at higher temperature. The trend of rapid stress relaxation at higher temperature is often observed in noble metal films [57]. The shape of the curves begins to resemble that of Al films, which have their own oxide layer on the top of the films, when it is protected by a passivation layer since either natural surface oxide (for Al) or passivation (for Cu) layer can hinder stress relaxation by the diffusional creep through the surface and grain boundary diffusion. For films without the passivation layer, the stress–temperature hysteresis can be simulated by assuming that thermally activated flow in the grain interior and boundary is responsible for the temperature dependence of the flow stress [55]. However, the curves for Al and passivated Cu films are not so easily modeled by a single relaxation mechanism, where the diffusion effects are mostly inhibited. The thermomechanical behavior of these type of films can be summarized as follows: They (1) support higher stresses at both high and low temperatures, (2) exhibit high strain hardening rate, (3) show an increase in apparent hardening rate upon cooling below $\sim$ 150 °C, and (4) exhibit yielding even in a tensile stress state upon re-heating, which is a typical characteristic of the Bauschiger effect.

In this study, the stresses that arise in a thin film of Al on a Si substrate are measured as a function of temperature via laser scanning, substrate curvature measurements. The characteristics of the stress–temperature hysteresis, particularly the hardening behavior and Bauschinger effect, have been evaluated in the context of the change in minimum cooling temperatures during thermal excursion. A phenomenological constitutive law governing the stress–temperature curve has also been developed by taking into account the cyclic loading character of thermal excursion.

3.2 Background

3.2.1 The Bauschinger effect

Suppose that a material first deforms plastically in a certain direction of stress state. Then, let the direction of stress be reversed to the point of causing plastic deformation in the opposite direction. If the magnitude of the stress at which reversed yielding first occurs is

significantly less than the magnitude of the stress that caused forward yielding, the ensuing asymmetry of plastic yielding upon reversal of stress direction is called the Bauschinger effect [58]. The origins of the Bauschinger effect in bulk metals and alloys are related to changes in the internal stress state arising from the changes in dislocation substructure, from the interaction of dislocations with other dislocations, particles or interfaces, and from the dissolution of sub-grain boundaries during load reversal [59]. Structural obstacles opposing the motion of dislocations generate a back stress during forward deformation; this back stress assists the motion of dislocations upon load reversal, thereby leading to the asymmetry.

Contributions to strain hardening in a metallic material during forward deformation may arise from a variety of mechanisms [60–63], including intrinsic hardening effects, such as solid solution strengthening, glide resistance of grain boundaries or interfaces; interaction of mobile dislocations with intersecting or forest dislocations in the material; and a back stress arising through dislocation interactions at barriers to glide. The first two of these three effects must be overcome in essentially the same way for forward straining as well as for reversed straining. However, the last of these three factors aids reverse deformation rather than opposing it, thereby engendering the Bauschinger effect (hereafter referred to as the BE). If the BE is due to the presence of a back stress, then the flow stress in the forward and reverse direction can be considered as follows [64]:

$$\begin{aligned} \sigma_{\mathrm{F}} &= \sigma_{\mathrm{o}} + \sigma_{\mathrm{d}} + \sigma_{\mathrm{B}}, \\ \sigma_{\mathrm{R}} &= \sigma_{\mathrm{o}} + \sigma_{\mathrm{d}} - \sigma_{\mathrm{B}}, \end{aligned} \tag{3.1}$$

where σ_{F} and σ_{R} are the flow stresses in the forward and reverse direction, respectively, σ_{o} is the proportional limit of straining(or yield strength) , σ_{d} is the flow stress increased due to intrinsic and forest hardening, and σ_{B} is the back stress. Hence, the back stress can be evaluated as:

$$\sigma_{\mathrm{B}} = \frac{1}{2}(\sigma_{\mathrm{F}} - \sigma_{\mathrm{R}}). \tag{3.2}$$

For thin metallic films on substrates, BE-like behavior has been experimentally observed in several systems during thermal excursion [52, 65, 66]. However, the quantitative

analysis of the BE in thin films has not been conducted.

3.2.2 Kinematic hardening

The two strain hardening rules which widely used in metal plasticity are those involving isotropic hardening and kinematic hardening. If the yield surface (which represents the yield condition in stress space) expands uniformly during plastic flow with no shape change or translation, isotropic hardening occurs. On the other hand, kinematic hardening takes place when the yield surface simply translates in stress space in the direction of the outward normal without changing its size and shape. In an attempt to account for the BE, several kinematic hardening rules have been proposed. Masing [67] proposed a material model consisting of a group of parallel, elastic–perfectly plastic elements, but with different yield strengths. Asaro [68] used Masing's approach to explain the various types of unloading curves which have been observed as the BE. Since the group of elements deforms under iso-strain conditions in this premise, the shape of the reverse loading curve is then determined by the order of the yielding of each elastic–plastic elements upon reverse loading. The type I kinematic hardening (KI) is observed when the yielding of sub-elements occurs twice as much upon reverse loading as the forward load at yielding and the order of yielding in both load direction is the same. Mróz [69] introduced a multiple yield-surface model (or the concept of a field of hardening moduli) to generalize the known rules of kinematic hardening of cyclic loading. In this model, the yield surfaces of different size are initially similar and concentric. When the applied stress reaches the inner-most yield surface after the elastic loading, the plastic deformation develops by moving the yield surface without changing their shape and orientation, until it reaches the next adjacent yield surface. The plastic strain can be defined by the appropriate number of yield surface and prescribed tangent moduli. Both approaches result in an identical stress-strain curve upon load reversal, and the predicted curve in a material which exhibits kinematic hardening can be constructed as follows: assuming the forward loading curve has the form $\sigma = f(\varepsilon)$, then the corresponding reverse loading curve has the form $\sigma = 2f(\varepsilon/2)$ if a new coordinate system is chosen with its origin at the end of the forward loading and rotated 180 ° [68].

3.2.3 Constitutive law

During thermal excursions with a constant cooling and heating rate, the thin film stresses are represented by:

$$\sigma = f(\sigma_y, n, \varepsilon), \tag{3.3}$$

where the yield strength, σ_y, and the film strain, ε, are a function of temperature, and n is the strain hardening exponent assumed to be constant over the thermal cycling range. If the stress–strain behavior of the thin film, which are under an equibiaxial loading condition (in other words, *proportional loading condition*), follows the elastic and the power law hardening relationship, the state of stress can be described by a variant of power law hardening [51]:

$$\sigma = \begin{cases} H_f \varepsilon^n, & \text{when } \sigma \geq \sigma_y, \\ M_f \varepsilon, & \text{when } \sigma < \sigma_y, \end{cases} \tag{3.4}$$

where M_f is the biaxial elastic modulus of the film and H_f is a constant, respectively. Since $M_f \varepsilon = H_f \varepsilon^n$ at the yield stress, H_f is given by $M_f^n \sigma_y^{(1-n)}$.

The thermally-imposed strain is controlled by the experimental condition, $\varepsilon = \Delta\alpha\Delta T = \Delta\alpha(T - T_o)$, where ΔT is the temperature change from the initial temperature, T_o, and $\Delta\alpha$ is the thermal expansion mismatch between the film and the substrate. The total strain is composed of both elastic and plastic strains:

$$\varepsilon = \varepsilon_{el} + \varepsilon_{pl}. \tag{3.5}$$

If there is no yielding, $\varepsilon = \varepsilon_{el} = \Delta\alpha\Delta T$. Therefore, the stress in the film, from Eq. (3.4), is:

$$\sigma = M_f \Delta\alpha\Delta T. \tag{3.6}$$

Once yielding occurs, Eq. (3.4) gives:

$$\sigma = (\Delta\alpha\Delta T)^n M_f^n \sigma_y^{(1-n)}. \tag{3.7}$$

In addition, since $\varepsilon = \Delta\alpha\Delta T$ and $\varepsilon_{\rm el} = \sigma/M_{\rm f}$, the plastic strain of the film is given by:

$$\varepsilon_{\rm pl} = \Delta\alpha\Delta T - \frac{\sigma}{M_{\rm f}}. \tag{3.8}$$

Finally, since the yield strength, σ_y, should be considered a function of temperature:

$$\sigma_{\rm y} = \sigma^*(1 - \frac{T}{T^*}), \tag{3.9}$$

where σ^* is the nominal yield strength at 0 K and T^* is a characteristic temperature which describes the (linear) temperature dependence of yield strength.

Once the direction of thermal load (the direction of strain) is changed (*i.e.* re-heating after cooling), the governing equation of stress-strain curves can be approximated as (see Sec. 3.2.2):

$$\sigma' = 2f(\sigma_{\rm y}, n, \varepsilon'/2), \tag{3.10}$$

which means the magnitude of temperature change for the elastic limit on the reverse loading is as much as twice of that on the initial loading. The simulated stress-temperature hysteresis, using Eqs. (3.3), (3.4), (3.9), and (3.10), is schematically illustrated in Fig. 3-2.

3.3 Experiments

Experiments were performed on Al films on Si substrates. Si wafers were 525 μm thick and 10 cm in diameter, with a (100) orientation. Both sides of the substrate were polished and oxidized to obtain an oxide thickness of 200 nm prior to film deposition. Polycrystalline thin Al–1 w% Si) films were then sputter-deposited to a 1 μm thickness at room temperature. Subsequently, the specimens were annealed at 400°C in a forming gas (N_2/H_2) atmosphere for 1 hour to stabilize the grain structure of the film. The curvature change of the substrate was measured as a function of temperature using a laser scanning technique (TENCOR FLX2320, Tencor Instruments, Mountain view, CA) in a N_2 atmosphere to prevent further oxidation of the film. A constant heating (10 °C/min) and cooling rate (–6 °C/min) were

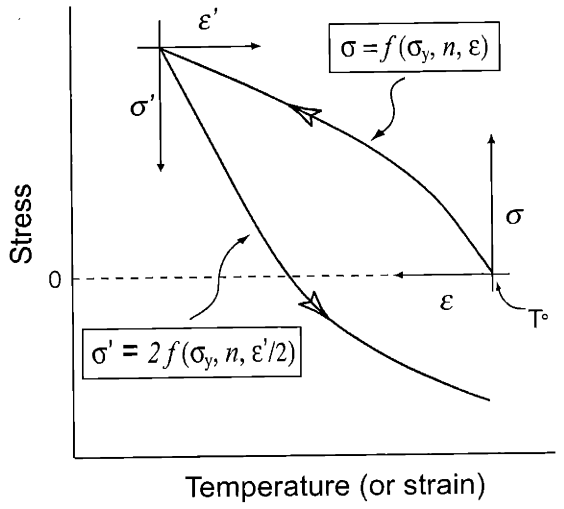

Figure 3-2: Simulated stress–temperature hysteresis of a thin film on an elastic substrate subjected to a kinematic hardening constitutive law with strong strain hardening and a temperature dependent yield strength.

imposed. The atmospheric N_2 gas was chilled in a liquid N_2 heat exchanger to maintain the constant cooling rate during the cooling cycle. The specimens were heated from room temperature to 300°C, and held for 30 minutes to relax the stress. The specimen was then cooled down to a predetermined temperature, and subsequently re-heated to 300°C. The designated minimum cooling temperatures used to impose varying levels of pre-strain were 110, 50, 20, and –10°C. The substrate curvature was continuously monitored during thermal cycling by recourse to the laser scanning method. Because of the relatively small film thickness, the Stoney formula was used to relate the film stress to the measured curvature change [56].

3.4 Results

Typical stress measurements obtained from a 1 μm thick Al film (cycled between room temperature to 300°C) are presented in Fig. 3-3. The linear portions of the curve represent the expected thermo-elastic behavior of Al films on Si substarates [Eq. (3.6)]. The first heating cycle is similar in shape to the curve for the second heating cycle, with the exception

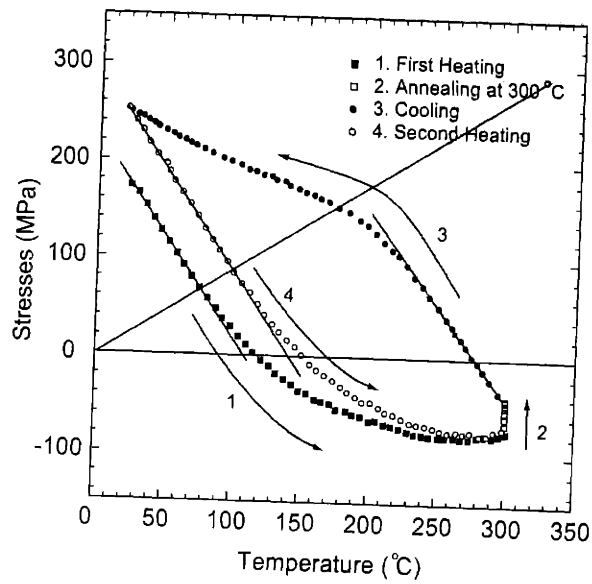

Figure 3-3: Stress–temperature hysteresis of a 1 μm thick Al film on a Si substrate thermally cycled between room temperature and 300 °C. The solid lines represent the elastic response of the film from Eq. (3.6).

of a lower initial stress. The difference arises because the stress has been relaxed, even at room temperature, after cooling from the annealing temperature. Once the stress begins to deviate from the linear behavior (at ~100°C), it increases continuously in compression, and then remains nearly constant from 250 to 300°C. During the 30 min holding period at 300°C, the stress relaxes to approximately one third of its initial value. Yielding upon cooling initiates at ~200°C, at a stress level of ~120 MPa. Upon further cooling, Hardening is essentially linear and the stress supported by the film at room temperature is ~250 MPa, indicating the relatively strong level of hardening. The rate of stress increase is slightly higher below ~60 °C. Upon re-heating, the deviation from the linear elastic response commences at ~130 °C, while the overall stress remains in the tensile state (~30 MPa). Further heating causes additional inelastic strain, and the stress increases in compression, up to ~280 °C. After the first full cycle, the hysteresis loop stabilizes and remains invariant if cycling continues within the same temperature range. The thermal excursions between other temperatures exhibit similar features. The stress-temperature curves of the first cooling and second heating cycles are used in subsequent analysis.

The experimental stress–temperature curves for four different thermal cycles are shown in Fig. 3-4. For the first cooling cycle (tensile strain) from 300 °C, all cooling curves are coincident, and the proportional limit, σ_o, of ~100 MPa is observed. The parameters that can be determined from Fig. 3-4 are the forward plastic strain, ε_F, the reverse yield stress, σ_R, and the maximum stress in the forward direction. The reverse yield stress is defined as the flow stress at a plastic strain of 0.0002 upon reverse loading (re-heating). These parameters can be used to calculate the forest hardening ($\sigma_d = \sigma_F - \sigma_B - \sigma_o$), total work hardening ($\sigma_{WH} = \sigma_F - \sigma_o$), back stress, and the Bauschinger effect ratio (BER $= \sigma_B/\sigma_{WH}$). Each of these parameters are summarized in Table 3.4 for varying thermal strain cycling levels.

The stress-temperature hysteresis implied by the constitutive equations for kinematic hardening given in Eqs. (3.4), (3.9), and (3.10) are compared with experiments in Fig. 3-4. Although the first cycle of heating and 30 min of annealing at 300 °C were applied to minimize any microstructural changes and residual stresses of the thin film, there was still a small level of unrelaxed stresses. Thus, the reference temperature for the comparison between the observation and the model has been chosen as $T_o = 275$ °. A single choice of values for the materials constants with n=0.4, σ^*=190 MPa, and T^*=1100 °C is in reasonable agreement with the experimental results for all four thermal cycles. The corresponding temperature-dependent yield stress is also presented with the dashed line. The excellent correspondence between the experimental and predicted curves suggests that kinematic hardening is the dominant hardening mechanism in the Al film on the Si substrate. Further evidence for the kinematic nature of hardening in Al thin films can be evidently found in Table 3.4. Although the effect of forest hardening slightly increases with increasing total forward strain, most of hardening is due to the back stress.

3.5 Discussion

The stress–temperature hysteresis curve in Figs. 3-3 and 3-4 have several characteristics: (i) Hardening continues upon cooling, resulting in the high stress. (ii) In the re-heating half cycle, hardening occurs as the temperature increases. (iii) Yielding initiates in tension in the re-heating half cycle, and this becomes more evident for lower minimum cooling

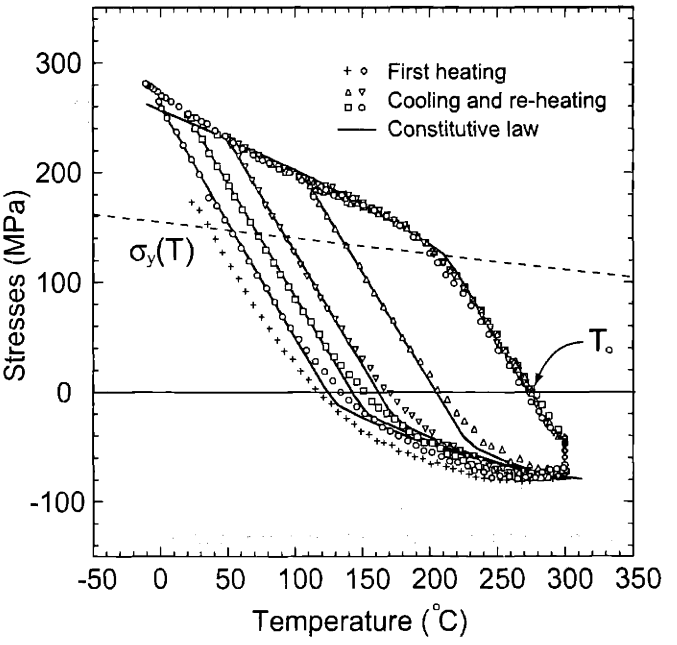

Figure 3-4: Stress–temperature hysteresis of a 1 μm thick Al film on a Si substrate thermally cycled between the several minimum cooling temperatures and 300 °C. The four minimum cooling temperatures are 110, 50, 20 and -10 °C. The solid lines represent the fitting of the constitutive law with Eqs. (3.3) and (3.10), combined with (3.4) and (3.9). The best fit yields n=0.4, σ^*=190 MPa, and T^*=1100 °C. The dashed line represents the temperature-dependent yield strength of the film.

Table 3.1: Bauschinger effect parameters for a 1 μm thick Al film on a Si substrate with different pre-strains (minimum cooling temperatures). σ_m is the maximum stress in the forward strain.

forward plastic strain (ε_p)	σ_m (MPa)	σ_{WH} (MPa)	σ_B (MPa)	BER
0.0006	188	88	71	0.807
0.0015	229	130	108	0.828
0.0019	252	152	124	0.816
0.0022	281	181	144	0.795

temperature. These characteristics cannot be explained by the normal yield behavior of Al. The first and second features can only be accounted for by invoking strong strain hardening, and the third indicates kinematic hardening. The stress difference between forward and reverse loading is essentially unaffected by the hardening upon forward loading (*i.e.*, cooling), and this is a typical of the Bauschinger effect (BE). As shown in Table 3.4, both the total work hardening and back stress increase monotonically with increasing forward strain, while the Bauschinger effect ratio (BER) remains nearly constant. The constant BER implies the majority of the hardening arises due to the back stress, and nearly 80% of hardening is due to the back stress.

An increase in the back stress with pre-strain is commonly observed in particle-hardened alloys or metal-matrix composites (MMC), for small strains ($\varepsilon_p < 0.01$) [60, 61, 64]. Although a single crystal or single-phase alloy also exhibits the BE, a dual-phase alloy or MMC, particularly one with strong, non-shearable obstacles to dislocation motion, exhibits a noticeably larger BE. An Al/SiC composite alloy can have a back stress of as much as 100 MPa with a pre-strain of 0.006 [60]. One explanation for the aforementioned phenomena is that the internal stress develops as a result of entrapment of shear loops around hard particles, which can also be evaluated in terms of the magnitude of plastic incompatibility between the plastic/soft matrix and the elastic/hard inclusions [57, 70]. An alternate explanation is based on the premise that plastic strain gradients develop between the hard and soft phases [71]. These strain gradients produce a residual stress which, in turn, produces the BE. However, neither of the above microscopic mechanisms can be directly applied to thin films even though there is a similar elastic/plastic mismatch between films and substrates (or passivation layers).

For a thin metallic film on a thick substrate, deformation in the absence of any diffusive processes occurs by dislocation glide or mechanical twinning. The likely scenario is that native oxide or the passivation layer and the substrate serve as primary obstacles to shear deformation. Since the thickness of the film is small, the spread of plastic deformation by cross slip or dislocation climb is restricted. Instead, dislocations would simply glide back and forth on the planes on which they were formed. This process then provides a possible mechanism for the generation of back stress during cyclic variations in stress through dislocation interactions, and a mechanistic rationale for the Bauschinger effect

reflected in kinematic hardening response in thin metal films.

Baker *et al.* [66] have shown that the pair-wise interaction of dislocations (threading-misfit or threading-threading) within the thin film may contribute to the strong strain hardening and high stresses observed. For most dislocation reactions, assuming annihilation does not occur, threading dislocations run back during unloading, which may be the source of such a high back stress in films on substrates. A recent modeling study with dislocations within the confined volume of thin-film grains shows a similar result [72]. The high strain hardening of thin films arises due to the interaction energy among dislocation loops and high dislocation density inside thin-film grains. The configuration of dislocation loops in the model was assumed to be generated in a parallel manner along the specific slip planes, which can easily restore dislocations into the original position upon unloading. The excessive energy due to the interaction among dislocations can increase as much as 45% of the total stored energy without considering the interaction for the similar film thickness and grain size of the film. Shen *et al.* [52] attribute the strong linear hardening of passivated Cu films on silica substrates to the strong barrier to inelastic shear, provided by the substrate and passivation layer. This is also accompanied by the inhibition of lateral spreading of dislocations (by climb or cross slip), attributed to the limited physical volume available in thin films. A back stress arises from the deformation in the inelastic shear plane, which enables kinematic hardening.

3.6 Conclusions

In this chapter, the strengthening of a thin Al film on a Si substrate has been shown to involve large strain hardening, and stress evolution of the thin film under various thermal cycles is successfully predicted by the kinematic hardening law. Based on the analysis of the Bauschinger effects, it has been shown that the back stress develops rapidly at small plastic strains. The high back stress arises from the confined deformation (by dislocations) within the small thin film grains, and that process enables kinematic hardening. The constitutive law based on the kinematic hardening model represents the stress–temperature hysteresis in this study, without other stress relaxation mechanisms such as diffusional creep. The mechanistic origin of the high back stress has not been verified at present. However, it is

suggested that such back stress is accounted for by the development of dislocation structures in the limited volume of film grains subjected to constraints by the film/substrate interface, passivation layer, and grain boundaries.

Chapter 4

Nanoindentation of Continuous Films and Patterned Lines on Si Substrates

In this chapter, a systematic experimental study of nanoindentation on continuous films and unidirectionally patterned lines of Al on Si substrates has been conducted. The results show an increase in the indentation compliance with increasing film thickness, h_f, and decreasing line width, w, in the very early stage of indentation, where the penetration depth of the indenter tip, h, is less than 100 nm ($h < 0.1h_f$). The observed experimental trends cannot be rationalized on the basis of continuum considerations (via finite element modeling), and suggest a significant role of the discrete dislocation motion in the incipient inelastic deformation mechanism. In small-volume structures, the experimental results show that the motion of dislocations is affected by various boundary conditions, such as film thickness and line width. A simple mechanistic model based on discrete dislocations is proposed.

4.1 Introduction

The inelastic mechanical behavior of small-volume structures depends on both the characteristic structural length scale and overall physical dimensions of the structures. This

dependence is increasingly apparent when the feature size is reduced to the micrometer scale. Such size dependence of mechanical response has been studied thus far primarily in the context of continuous thin films on substrates (see Chapter 2). These trends cannot be directly extended to assess the mechanical response of patterned features as, for example, when a film is patterned into strips, lines, or islands. These patterned features are encountered more frequently in applications of small-volume structures. Patterned features constitute structures that have small length in more than one dimension, and their mechanical response under different confining conditions remains largely unexplored due to the complexity of stress states within the structure and the deficiency of appropriate experimental techniques to characterize local deformation.

As we have seen in the previous chapters, one of the most common experimental techniques employed to measure the mechanical properties and stress evolution of thin films on substrates is the substrate curvature method. Interpretation of such experimental results is generally accomplished by recourse to the Stoney formula [73], in which the stresses in the film are assumed to be equibiaxial, constant through the film thickness and proportional to the underlying substrate curvature. However, the patterning of a continuous film into strips, lines or islands introduces a triaxial stress state and gradients in stress in the resulting structures. X-ray diffraction is another common experimental method used to extract volume-averaged stresses in thin films and patterned lines on substrates [74, 75]. During diffraction experiments, a film is typically thermally strained (as in curvature experiments) and the lattice constant of the strained film or line structure is measured and compared to that of unstrained film. A conversion via Hooke's law is used to calculate the corresponding stresses. Such an experimental measurement does not require knowledge of substrate curvature to extract film and line stresses, but the probe width of any X-ray experiment is often larger than the width of the structures (*e.g.* line width) presently under study. Moreover, those experimental techniques impose strains by using thermal excursions, which facilitate the thermal expansion mismatch between a film (or line) and a substrate. Thus, an understanding of the temperature-dependent properties is required, but little is known as to those properties of small-volume structures. Various computational and analytical efforts have been pursued to quantify the stress state of small-volume structures [76–80], but these analyses are limited in that they calculate the stresses in an elastic state, and

often provide overly constrained boundary conditions.

Nanoindentation, defined as the quasi-static penetration of a surface to depths on the order of nanometers, has been utilized extensively to probe mechanical properties of thin films [81–83]. As this technique can generate large strain (or stress) within a relatively small volume of the material, nanoindentation can be utilized to probe small-volume structures, such as patterned lines and islands on substrates. Nanoindentation experiments at such a small scale also provide considerable opportunity to investigate the initial stage of material deformation and the effect of geometrical boundary conditions (overall physical dimensions of structures and their constraints) on the deformation mechanisms. In addition, imposing strain at room temperature allows us to circumvent the issue of temperature-dependent properties. A particularly appealing attribute of nanoindentation is that, at least in principle, it offers a means to probe the elastic and plastic deformation characteristics, as well as residual stresses [84], in small features that are patterned onto substrates under constraints which are representative of those present in real applications including micro-electro-mechanical systems (MEMS) and microelectronic devices and packages. However, the interpretation of material response during indentation remains a complex issue, and nanoindentation of small-volume structures on substrates inevitably requires careful assessment of the various length scales involved [27, 29, 83]. First, the nanoindentation responses can be sensitive to such factors as surface oxidation, surface roughness, residual stress, as well as the texture, grain size and thickness of the film on the substrate. Secondly, given the small depths of indenter penetration into the thin film, the tip geometry (i.e., the shape and tip radius) of the indenter can markedly influence the indentation response, especially in the early stages of loading [29, 85]. Thirdly, depth-sensing indentation is known to be strongly affected by the nucleation of defects and by the plastic deformation characteristics of the materials, which, in turn, are functions of geometrical length scales (e.g., film thickness and line width) and microstructure (e.g., grain size, texture, etc.). Despite the growing interest in nanoindentation on films and small-volume structures, very little is known about the microscopic deformation processes occurring beneath the indenter and their effects on the overall indentation response with different boundary conditions. This understanding is necessary in order to accurately extract the mechanical properties of small-volume structures from the nanoindentation response.

In this chapter, instrumented nanoindentation experiments of continuous films and patterned lines of aluminum on a silicon substrate have been performed to explore the effects of two length scales (film thickness and line width) on the indentation load–displacement (P–h) response. Computational modeling of these experiments, discussed in Chapter 5, is conducted to correlate the experimental observations and underlying mechanisms.

4.2 Materials and Experimental Procedures

Polycrystalline thin films of Al–1.5wt% Si, 0.33, 0.7, and 1.0 μm in thickness, were sputter-deposited on 525 μm thick Si substrates at room temperature. X-ray diffraction data confirmed strong (111)-oriented textures of all films. Transmission Electron Microscopy (TEM) of an as-deposited film of 1 μm thickness was conducted using standard dimpling and ion-milling procedures. The TEM micrograph in Fig. 4-1 shows that the average grain size of the film was $\sim$0.6 μm and the grains exhibited a typical columnar structure. A film of 1 μm thickness was subsequently patterned into sets of parallel lines with different widths, using standard photolithography and dry etching techniques. The nominal line width was varied from 1.5 μm to 5.0 μm with an incremental increase in width of 0.5 μm, for a total number of eight line width sets. The length of lines was 500 μm. Each set of lines contained seven lines of the same width, with an inter-line spacing equal to line width [Fig. 4-2(a)]. A square pad of 500 μm$\times$500 μm was patterned next to the sets of lines to represent a continuous thin film. Each of the sets was separated by 20 μm. All structures were constructed on the same wafer by a single set of deposition and etching processes such that all characteristics of film and lines are expected to be the same, except for the in-plane dimensional length scale (*i.e.* line width).

Nanoindentation experiments were carried out with a three-sided diamond Berkovich indenter tip on two types of commercially available nanoindenter machines: NanoTest 600 indenter (MicroMaterials, Ltd., Wrexham, UK) and Triboindenter (Hysitron, Inc., Minneapolis, MN). Two nanoindentation machines were equipped with indenters of different tip radii. All necessary experimental parameters, such as the tip area function and machine compliance, were carefully calibrated prior to the set of each experiment using a standard quartz specimen on both nanoindenters. Load-controlled, depth-sensing nanoindentations

Figure 4-1: Plane view of TEM micrograph of a 1 μm thick polycrytalline Al film on a Si substrate.

over a complete loading and unloading cycle, were conducted on the thin films and lines of different widths. On the Triboindenter, loading was terminated at 250 μN and 1000 μN, as it was not possible to terminate loading at a specific depth; these maximum loads were chosen to attain approximately the same maximum depth of indentation as on the NanoTest600. In both sets of experiments, a constant loading/unloading rate of 20 μN/s was applied, and a dwell period of 10 s was imposed at the maximum load, prior to unloading. The positioning of the indenter in the middle of the line is an experimental challenge which has been successfully overcome in the present experiments on both nanoindenters. By employing each indenter as a scanning probe (please see Appendix B for details), the accuracy of indenter positioning at the center of the lines was better than ± 0.1 μm. All indentations were oriented identically with respect to the line direction in order to minimize anisotropic effects due to the low symmetry of the Berkovich (trigonal pyramid) indenter. Figure 4-2(b) shows a series of indents at the center of the top surface of a 3 μm wide line to demonstrate positioning accuracy.

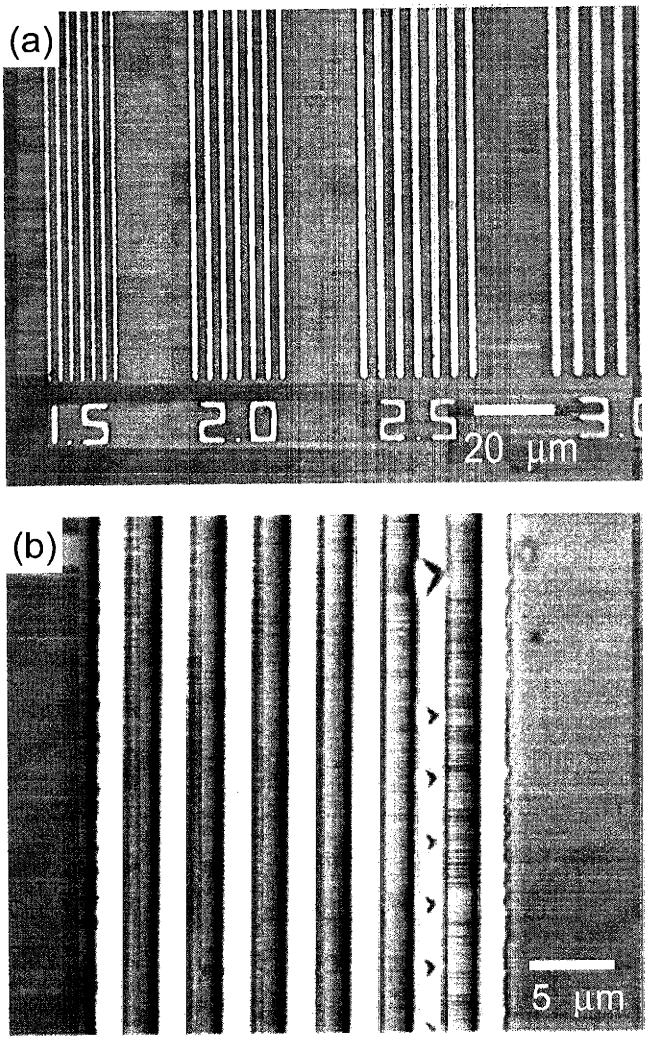

Figure 4-2: Micrographs of (a) the patterned lines of polycrystalline Al on a Si substrate, and (b) a series of indents at the center of the top surface of 3 μm wide Al line. The maximum depth of indentation was 500 nm to demonstrate large indents. All indentations were oriented in the same way with respect to the line direction.

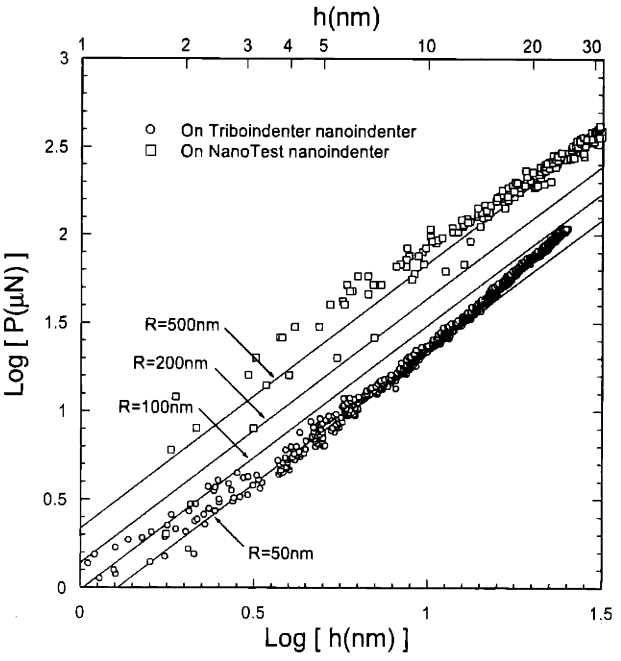

Figure 4-3: Load-displacement (P–h) response of two diamond indenters on a quartz specimen in log-log scale. Solid lines represent Eq. (4.1) with different tip radii.

4.3 Experimental Results

4.3.1 Evaluation of tip radius

Since indenters are not atomically sharp in practice and the penetration depths ($\leq$200 nm) in this study were comparable with the estimated tip radius ($\geq$50 nm), the evaluation of tip radius and shape is required for subsequent analysis of the experimental data. This tip may be approximated as having spherical shape. The side of the indenter is assumed to be tangent to the spherical tip (see Chapter 5 for details). The effect of tip radius on the elastic indentation response of a material can be probed using the classical Hertzian analysis [28, 29, 86]. When the depth of indentation is sufficiently shallow ($h < R$), the initial portion of the P–h curves prior to any inelastic deformation follows:

$$P = \frac{4}{3}E^* \cdot h^{3/2} \cdot R^{1/2}, \qquad \frac{1}{E^*} = \frac{1-\nu_1^2}{E_1} + \frac{1-\nu_2^2}{E_2}, \tag{4.1}$$

where R is the radius of indenter tip, E^* is the reduced elastic modulus of the specimen and indenter, E_1 and E_2 are the elastic moduli of the specimen and indenter, respectively, and ν_1 and ν_2 are the Poisson's ratio of the specimen and indenter, respectively. Based on Eq. (4.1), the nominal indenter tip radius can be estimated via plotting the elastic P–h response in the log-log scale if the mechanical property of materials involved in the indentation is well established. Figure 4-3 shows the log-log plot of P–h curves on quartz for Berkovich indenters mounted on two nanoindenters. Solid lines indicate Eq. (4.1) with different tip radii and a fixed E^* of 73 GPa for quartz indented by a diamond indenter. While the tip mounted on the Triboindenter was relatively sharp (50$\sim$100 nm), the tip on the NanoTest was more rounded ($\sim$500 nm). Thus, hereafter the experiments noted as *"with a sharp tip"* and *"with a rounded tip"* indicate ones on the Triboindenter and on the NanoTest, respectively.

4.3.2 Nanoindentation of continuous films

A typical load-displacement (P–h) response of an Al film, 1 μm in thickness, with a sharp tip is presented in Fig. 4-4(a) and a corresponding log-log plot of the loading curve, which

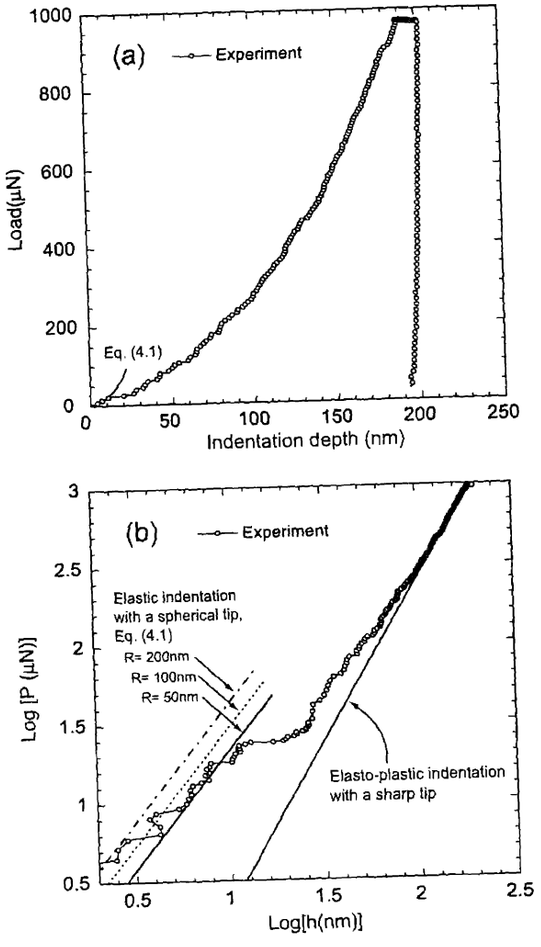

Figure 4-4: A typical load-displacement (P–h) response of a continuous Al film of 1 μm thickness in normal scale (a) and in log-log scale (b). The predictions for elastic indentation responses with a spherical tip (Eq. 4.1) and an elasto-plastic response with a sharp tip are also plotted.

can reveal the details in the very early stage of indentation, is also presented in Fig. 4-4(b). Characteristic discontinuities, which have been observed consistently in the experimental P–h responses of thin film or bulk single- and polycrystalline face-centered cubic (FCC) metals indented to nanometer-scale depths [28, 83], are also observed in this study. The initial portion of the P–h curves prior to the first discontinuity follows the elastic response for spherical indentation [86]. The estimated local shear stresses beneath the indenter, at the onset of the first discontinuity, approach the theoretical strength of Al ($\mu/10$ = 2.7 GPa, where μ is the shear modulus). This observation indicates that homogeneous defect nucleation is a plausible mechanism for the initiation of contact-induced plasticity [87, 88]. This hypothesis has been supported by the *in situ* experiments via the Bragg-Nye bubble raft analogue [87], which showed that nanoindentation of a two-dimensional crystal indeed resulted in homogeneous dislocation nucleation. After deviation from the initially elastic response, the P–h response gradually approaches the prediction of sharp indentation for an elasto-plastic material. For a film of 1 μm thickness, the penetration depth at a load of 200 μN is less than 10% of the film thickness t, a generally accepted depth limit [81] beyond which the substrate may contribute to the nanoindentation response of the films. Up to this loading point, however, the P–h response consists of a series of discontinuities, and the transition to the continuous elasto-plastic response is not attained fully. Due to the presence of these discrete events in the P–h response, these data cannot be analyzed in terms of continuum concepts of plasticity.

In order to analyze the discontinuous nanoindentation response quantitatively, the penetration depth h, at a particular level of imposed load P is considered as a measure of the indentation compliance of material during nanoindentation. This parameterization can be extended to nanoindentation of patterned lines, where the general analysis of indentation based on the semi-infinite half space of the indented material is invalid due to the unconstrained line sidewalls. These loads are chosen to be 100 and 200 μN, such that the corresponding indentation depths are less than $0.10h_{\mathrm{f}}$ in a continuous film where h_{f} = 1 μm.

Figure 4-5 shows the statistical variation of penetration depths of continuous thin Al films with a rounded tip at a fixed indentation load of 100 and 200 μN. The mean penetration depths h_{mean} are also indicated. Although there exists a relatively large scatter in

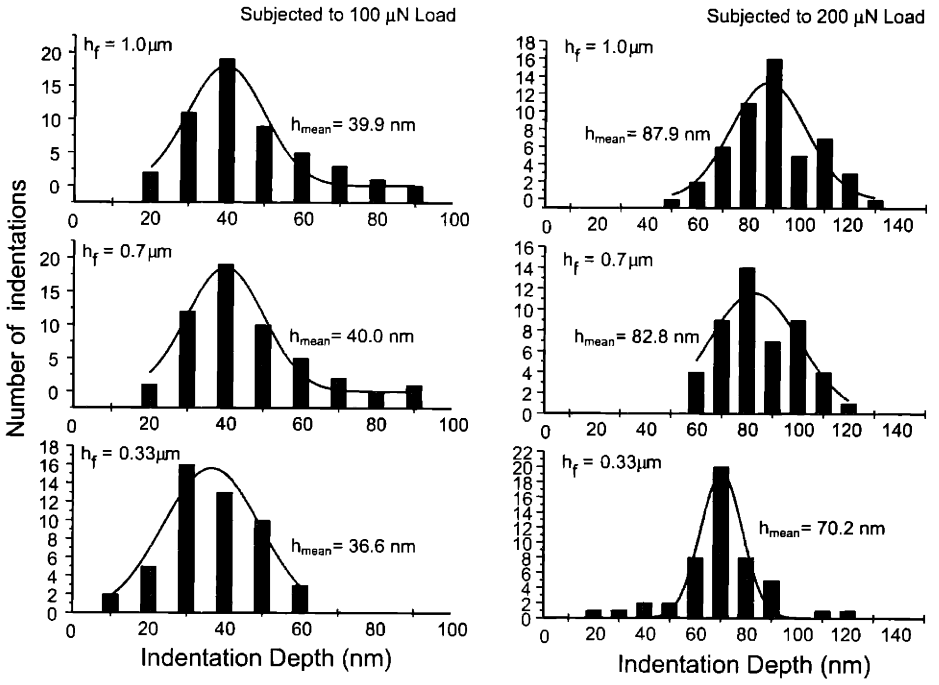

Figure 4-5: Statistical distributions of indentation depth at 100 and 200 μN indentation load for polycrystalline Al thin film of 0.33, 0.7, and 1.0 μm thicknesses. Each set of experiments contained 50 indentations. The mean penetration depths of indentation h_{mean} are indicated near the normal distribution curves, which are denoted by the solid lines.

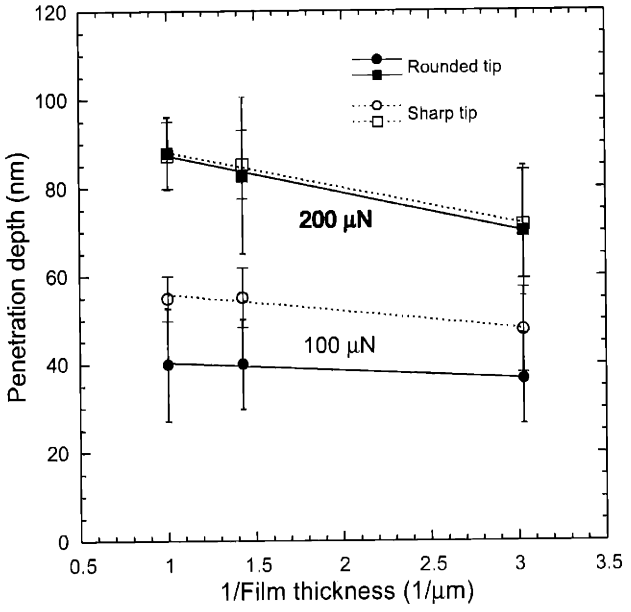

Figure 4-6: Penetration depth as a function of film thickness of continuous Al films subjected to 100 and 200 μN indentation loads. The error bars indicate ± 1 standard deviation in penetration depths of 20, at least, indentations.

experimental data, likely due to the polycrystalline nature and as-prepared surface roughness of the specimens, the observed trend is clear: thicker films are more compliant under the same indentation load, resulting in a greater indentation depth. Results observed with a sharper indenter tip ($R \sim 100$ nm) show the same trend. At a load of 100 μN, the average penetration depths h_{mean} of 0.7 and 1.0 μm-thick films are the same, but exceed that of 0.33 μm thick film, indicating that no thickness effect on the P–h response at this load for $h_{\text{f}} > 0.7$ μm. The variation of penetration depths (*i.e.*, experimentally observed scatter) is similar for all three films, with the exception that the two thicker films exhibit an increased frequency of above-average penetration depths. Note that at a load of 200 μN, the mean penetration depth and the distribution of observed depths (scatter) increase with increasing h_{f}. The penetration depth as a function of film thickness at 100 and 200 μN indentation loads is summarized in Fig. 4-6 for both indenters. The difference in the penetration depths for two indenter tip radii at 100 μN is clear—depths are larger with a sharp tip—but this difference diminishes considerably at a load of 200 μN.

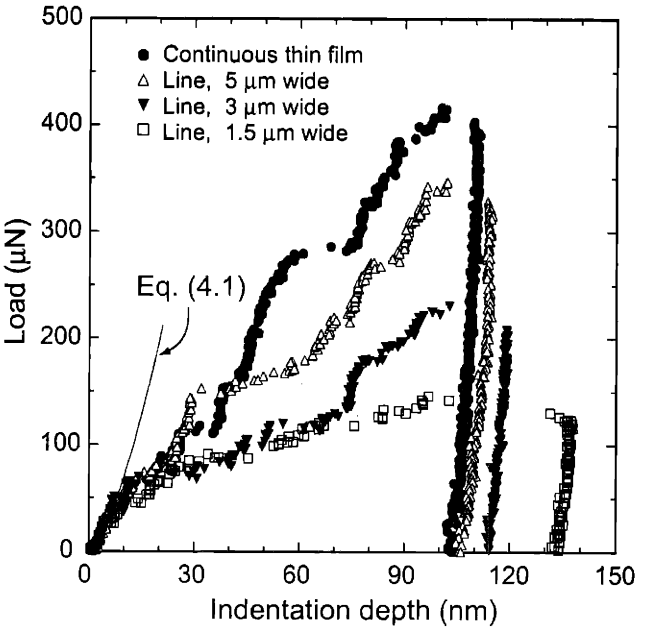

Figure 4-7: Load-displacement (P–h) responses of polycrystalline Al thin film and lines of 1.5, 3.0, and 5.0 μm line widths. The solid line denotes the elastic response on aluminum of a spherical diamond indenter with the tip radius $R = 500$ nm.

4.3.3 Nanoindentation of patterned lines

Typical load-displacement (P–h) responses of continuous film and patterned lines of three different line widths, all of equal thickness t, are shown in Fig. 4-7. Nanoindentation was conducted with a rounded tip. The film and lines have the same thickness of 1 μm. The initial elastic P–h response matches well with the elastic response for a spherical indentation when the spherical tip radius is assumed to be 500 nm [Eq. (4.1)]. The initial deviation from the elastic response, which occurs over a load range of 45–65 μN, is approximately independent of line width w. The corresponding maximum shear stress sustained by the indented film and lines are 1.8–2.0 GPa at the point of first deviation from the elastic response, which compares well with the theoretical shear strength of Al ($\sim$2.7 GPa), and is similar to the trends documented for continuous films of Al and Cu [29, 83]. The indentation compliance, which can be represented by the curvature of the loading response, is also unaffected by line width prior to the first deviation.

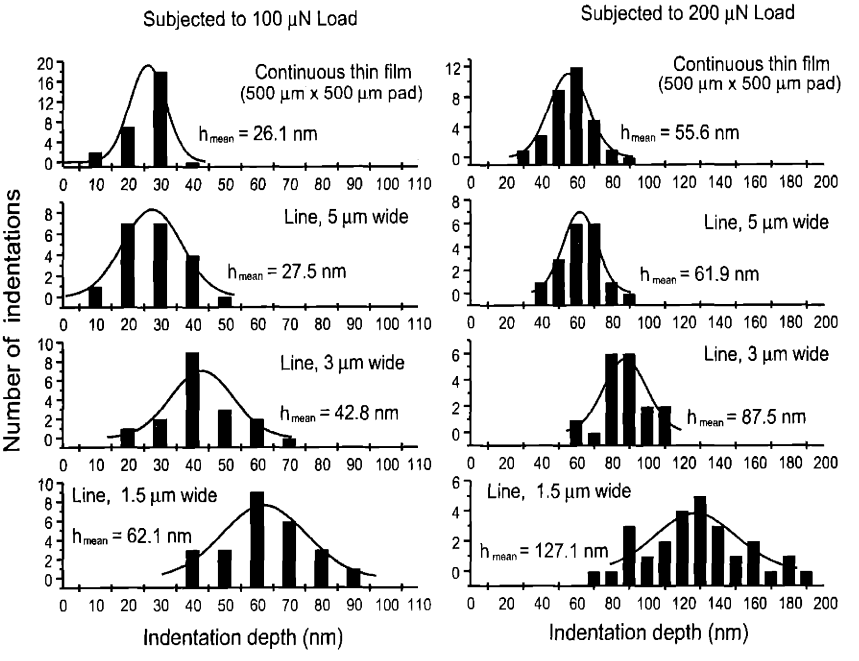

Figure 4-8: Statistical distribution of indentation depth at 100 and 200 μN indentation load for polycrystalline Al thin film and lines with 1.5, 3.0, and 5.0 μm line widths. The mean penetration depths of indentation h_{mean} are indicated near the normal distribution curves, which are denoted by the solid lines.

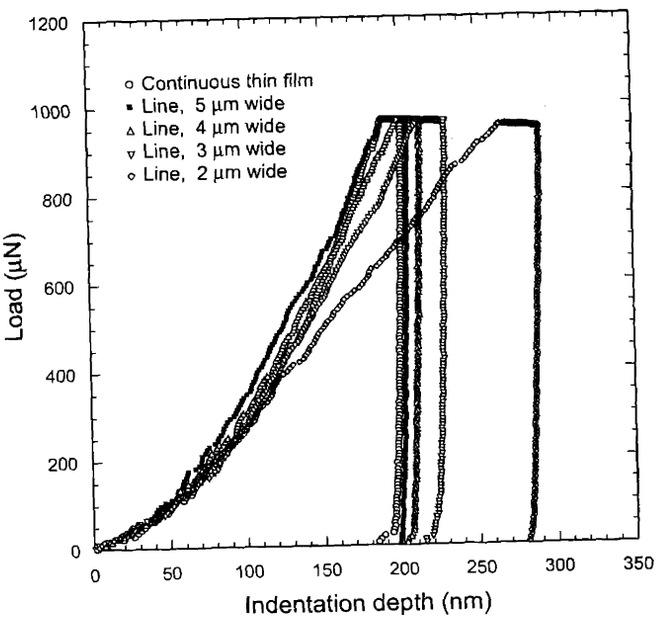

Figure 4-9: Load-displacement (P–h) responses of polycrystalline Al thin film and lines of 2, 3, 4, and 5 μm line widths with a sharp indenter tip. The maximum load is fixed as 1 mN, and the film and line thickness are the same of 1 μm.

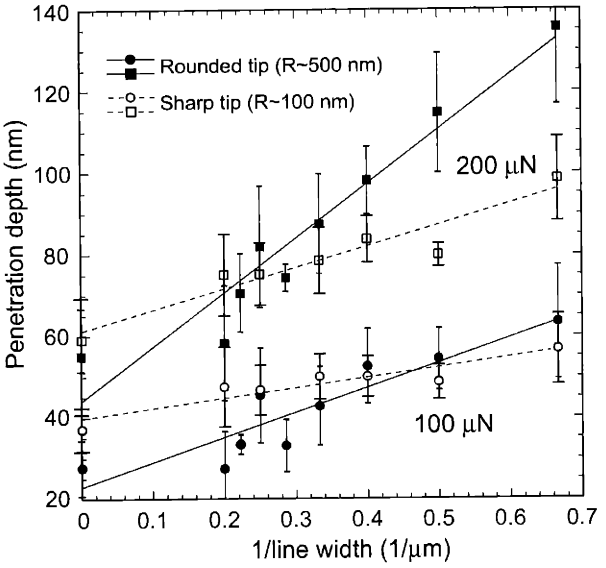

Figure 4-10: Indentation depth as a function of line width for 100 μN and 200 μN indentation loads. The error bars indicate ± 1 standard deviation in penetration depth of indentation experiments.

Each of these P–h curves exhibits discrete changes (jumps) in the load versus displacement response after the initial deviation from the elastic response, as observed in continuous thin films. The distinct separation of discrete discontinuities, commonly associated with defect nucleation, is reduced with decreasing line width (for a fixed line thickness). Unlike the elastic response, the P–h response subsequent to this initial deviation is a function of line width, w. The curvature of the loading response decreases with decreasing, w, indicating a greater indentation compliance for smaller line width. The discrete discontinuities in the P–h response are not as clear as those observed in the indentation of single-crystalline continuous films [29, 83]. The penetration depth during a holding period of 10 s at maximum load also increases with decreasing line width. The unloading slope in Fig. 4-7 is similar for all line widths, which results in a decrease of the apparent elastic contact modulus during unloading.

Again, the penetration depth, h, at a particular level of imposed load can be considered as a measure of the indentation compliance to quantify the loading portion of the P–h response. Figure 4-8 shows the statistical variation of indentation depths of the continuous

thin film and lines of the same thickness at a fixed indentation load of 100 and 200 μN. The mean penetration depths h_{mean} are indicated in Fig. 4-8. It is evident that narrower lines deform more readily under the same indentation load, resulting in a greater indentation depth. The indentation depth of a 5 μm wide line is almost equal to that of the continuous film, and the average indentation depth increases as line width decreases. The variation of indentation depths in a given set of experiments for a particular line width also increases as line width decreases. Typical P–h curves with a sharp indenter tip, which were conducted at the higher maximum load, are presented in Fig. 4-9. Although the increase in compliance with line width in this figure is not apparent as much as in Fig. 4-7 at the loads of 100 and 200 μN, the statistical analysis clearly shows the same trends. Indentation penetration depth for both a rounded and a sharp indenter tip as a function of line width for 100 μN and 200 μN indentation loads is summarized in Fig. 4-10. Each data point is the average of at least 13 experiments for a rounded tip, and that of seven experiments for a sharp tip, respectively. It is apparent that compliance increases more rapidly with decreasing line width w as the tip radius R increases.

4.4 Discussion

Both theoretical and experimental studies for thin metal films on a substrate, chiefly via curvature and X-ray diffraction methods (see Chapter 2), have shown that a thinner film is plastically stronger (less compliant) than a thicker one. In this case, a homogenous state of equibiaxial stress exists in the thin film (except near the free edges). In contrast, the stress field near the indenter tip is highly localized and inhomogeneous. Several studies have investigated the influence of substrates on the nanoindentation responses of thin films [89–91]. The chief concerns of these investigations have been estimation of the hardness and modulus of films independent of the substrate. As these studies employed continuum analysis and focused on the unloading response required to calculate these material parameters, such findings cannot be extended directly to our experimental observations which are dominated by discrete load-displacement events. In addition, the indentation depths considered in the present analysis were about 12% of film thickness. Ohmura *et al.* [92] experimentally verified the critical depth, beyond which the substrate effect comes in, can be extended 20% of film

thickness for several FCC metal thin films on sapphire single crystal. Recent finite element modeling (FEM) showed that the limits can be extended to greater depth for softer films on harder substrates [93]. Therefore, it is likely that the change of indentation compliance with film thickness, especially in the thicker films used in the present experiments ($h_f = 0.7$ and 1.0 μm), is not attributable to an increasing yield stress with decreasing film thickness.

Stress states in patterned metal interconnect lines on Si substrates have also been studied using other, complementary experimental and theoretical techniques [76, 94–96]. Most experimental work has been focused on the stress evolution of patterned lines with a passivation layer (either oxide or nitride) during thermal excursions. Such results indicate that the patterned lines with a passivation layer withstand much higher stress than films, and in fact some lines exhibit almost no plastic deformation. This suggests that patterned lines with a passivation may exhibit higher strength than films of the same thickness and may reflect the unique constraints of passivated metallic lines. However, the present experimental observation of nanoindentation on patterned lines without a passivation showed that narrower lines deform more readily under the nano-scale contact. Although the properties of unpassivated patterned lines are much less explored, this observation suggests that the yeild stress may decrease with decreasing line width. FEM-simulated P–h responses of patterned lines with the same yield stress as the continuous film have failed to explain such a large increase in compliance under indentation (Fig. 4-11). However, the significant number of discontinuities in the very early stages of indentation responses, which relate to the discrete motion of dislocations, prevents straightforward interpretation of the increase in compliance of lines with decreasing σ_y.

4.4.1 Plastic zone size

One possible explanation for the observed increase in compliance with decreasing line width is the interaction of the elasto-plastic boundary beneath the indenter with the free sidewall surfaces of the patterned lines. It has been shown [27, 28] that a force balance of Johnson's elasto-plastic indentation model can be used to estimate the plastic zone size, c, as a function

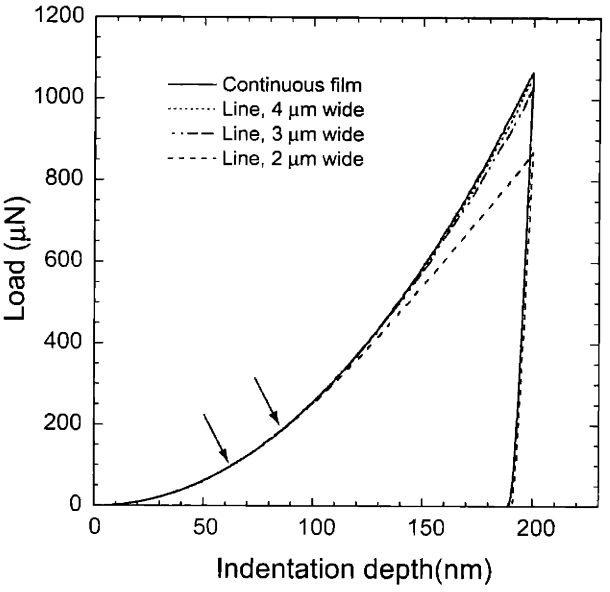

Figure 4-11: Simulated load-displacement (P–h) responses of Al thin film and lines using the general purpose finite element package ABAQUS [97]. The indenter was a sharp conical rigid indenter with the included half angle of 70.3°, and σ_{ys} of film and lines is assumed to be 300 MPa. The arrows denote the load levels in Fig. 4-10.

of the applied load and tensile yield strength, σ_{ys}, of the material as:

$$c = \sqrt{\frac{3P}{2\pi\sigma_{ys}}}. \tag{4.2}$$

From Eq. (4.2), the plastic zone sizes are 0.40 and 0.56 μm for indentation loads of 100 and 200 μN, respectively, when σ_{ys} is assumed to be 300 MPa [2]. Since the stress outside the plastic zone vanishes quickly with increasing distance from the indenter tip ($\sigma \sim r^{-3}$) [86], the zone size is expected to be similar for the film and lines. Finite element modeling (FEM) [97] of a sharp conical indentation on the continuous film, as well as on 2 and 3 μm wide lines of the same 1 μm thickness on a Si substrate (see details in Chapter 5), indicates that the plastic zone sizes are 0.57~0.58 μm for the film and lines at 200 μN indentation load, which agree well with the analytical prediction. The corresponding FEM simulated P–h curves in Fig. 4-11 show that the response of these three cases are essentially indistinguishable up to a load of 300 μN.

The initial stage of nanoindentation is often explained by the 'punch-out' of dislocation loops around the indenter tip [27, 83]. When the indenter depth increases, the dislocation density increases by the nucleation of new dislocations and/or the expansion of existing dislocations. The indenter tip displacement should be accommodated by the plastic flow beneath the indenter tip which is directly related to the number and position of dislocations. The interference between the stress field of dislocations and the free surfaces of the lines could be considered if the 'punched-out' dislocations can extend their equilibrium position beyond the continuum elasto-plastic boundary. This supposition appears to be a feasible mechanism, in light of the recent result of nanoindentations on Al and Cu films [29, 83]. In these experiments, the P–h curves are affected by film thickness even at very shallow depths of indentation ($h \leq 0.1h_f$) which are generally considered small enough to avoid substrate effects. Since the P–h response of single-crystalline Al films of two distinct thickness (0.6 and 1.0 μm) are distinguishable at a load of 30 μN ($c \approx$0.22 μm) [76], dislocations would be expected to extend as much as 5 times beyond the continuum plastic zone. Using this line of reasoning, the dislocation extension in our experiments can be as much as 2.8 μm at 200 μN load. This distance agrees well with pattern line half-width (since c is the radius of plastic zone) at which the P–h response of lines begins to deviate from that of the film.

4.4.2 Discrete dislocation model

Considering that dislocations are generated near the indenter tip and that they glide along the slip plane to the side surfaces, the effect of dislocation glide on the indenter tip penetration depth in the lines can be rationalized in the following manner. For simplicity, only edge dislocations, which are parallel to the line direction, are considered. It is assumed that the dislocations move in the cross-sectional plane of the line, which has height of h_f and width w, as shown in a schematic in Fig. 4-12.

As a first-order approximation, the total indentation depth of patterned lines is assumed to be a linear sum of the displacement due to dislocation generation along the indentation direction ($h_{film} \sim Nb_y$, where b_y is the projected magnitude of the Burgers vector along the indentation direction) and the additional displacement of the tip due solely

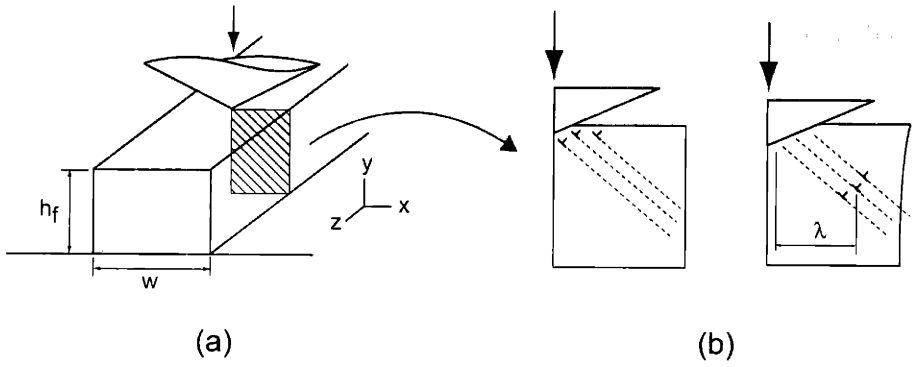

Figure 4-12: Schematics for a discrete dislocation model, (a) Geometrical configuration of the indenter and patterned line, and (b) Deformation of the cross sectional plane (shaded area in (a)) by the glide of dislocations along the slip planes.

to the geometrical effect of the dislocation movement parallel to the line surface (Fig. 4-12(b)). The additional plastic shear strain of the cross section due to the parallel movement of a dislocation becomes $\gamma = (2\lambda b_x/wh)$ [98], where b_x is the projected magnitude of the Burgers vector along the x direction and λ is the dislocation glide distance parallel to the line surface. When there are N dislocations that move over the average glide distance λ, the additional plastic strain around the indenter tip is given by $2\lambda N b_x/wh$. This term becomes negligible in the case of continuous films for which $w = \infty$. In the case of patterned lines, however, the material displacement around the indenter tip accompanying this strain becomes $2\lambda N b_x/w$ for a fixed film thickness of h_f. Thus, the total indentation depth of patterned lines, h_{line}, becomes:

$$h_{line} = h_{film} + h_{geo} = h_{film} + \alpha \frac{2\lambda N b_x}{w}, \tag{4.3}$$

where α is a geometrical constant that includes the relative direction of dislocation motion with respect to the indentation axis. The inverse-linear dependence of line width on the indentation depth in Fig. 4-10 is captured by Eq. (4.3). Assuming that the number of generated dislocations N is the same for both films and lines, the average glide distance of dislocation λ can be evaluated from the experimental slope of Eq. (4.3) in Fig. 4-10. The number N can be estimated by the indentation depth deviation from the elastic curve.

Taking $\alpha \sim 1$ and $b_x = 0.28$ nm, λ is evaluated to be 2.2 μm and 1.7 μm for 100 and 200 μN indentation loads with a rounded indenter tip, respectively. These calculated values of λ agree well with the value estimated from the mechanistic reasoning given earlier (2.8 μm), and again are much larger than the plastic zone size derived from continuum prediction (0.56 μm).

4.5 Summary of Experimental Observations

As the nanoindentation response consisted of a stochastic distribution of discontinuities in load and displacement, the penetration depth at a fixed load was chosen to parameterize the compliance of material under nanoindentation. The experimentally observed behavior can be summarized as follows:

- There are no length-scale effects on the elastic response of indentation, prior to the first displacement discontinuity that indicates the onset of plastic deformation. The critical shear stress sustained by the indented material at this first discontinuity approaches the theoretical shear strength of the material, suggesting that this discontinuity indicates homogeneous (subsurface) dislocation nucleation.

- In spite of the large scatter among experiments, the overall trends can be captured by using an appropriate statistical analysis. The experimental scatter may arise from several factors, such as polycrystalline nature of specimen, surface roughness, and various microstructural obstacles to dislocation movement.

- In the inelastic deformation regime, thicker films are more compliant during nanoindentation, exhibiting larger penetration depths at a fixed indentation load. Although the indentation depth is relatively shallow ($h \leq 0.12t$), the effect of film thickness on resistance to the deformation is pronounced.

- In the inelastic deformation regime, narrower lines are more compliant during nanoindentation when $w \leq 5$ μm. The penetration depth of indentation increases as w decreases, but those of a continuous film and of a 5 μm wide line are comparable.

- The indenter tip radius R plays a role in the effect of length scale on nanoindentation experiments. The indenter with smaller tip radius shows larger penetration depth on continuous films, and compliance increases more rapidly with decreasing line width for larger R.

As continuum based analyses (both analytical and FEM) cannot rationalize this experimental trend, a simple mechanistic model of discrete dislocation extension has been proposed as a possible mechanism. Although no direct experimental evidence for such a mechanism proposed in this study has been reported, the substantiation of the results in this study may contribute significantly to our understanding the microplasticity at the incipient stage of nanoindentation, as well as the effects of length scale on the early stage of inelastic deformation of materials.

Chapter 5

Simulations of Nanoindentation on Thin Films and Patterned Lines

In this chapter, nanoindentation of continuous films and patterned lines on Si substrates is simulated via two distinct computational approaches. Continuum and atomistic computational simulations of these nanoindentation experiments through finite element modeling (FEM) and molecular dynamics (MD), respectively, are conducted to elucidate the mechanism by which constraint influences the size-dependence of plastic flow, as well as the mechanisms by which this earliest stage of plastic deformation progresses in the material. By correlating observations from both experiments and computations, possible mechanisms responsible for those size effects are discussed.

5.1 Finite Element Simulation of Nanoindentation

5.1.1 Introduction

The finite element method (FEM) has been widely used to simulate elastic and plastic deformation during indentation, due to the obvious mathematical complexity of the indentation process [99–103]. Measuring material hardness via a sharp pyramidal indenter (*e.g.*, Berkovich, Vickers), is a very complex analytical problem, despite its widespread experi-

mental use. This complexity is due to the three-dimensional loading geometry associated with elastic and plastic deformation, and inherently large strain fields. For bulk materials, comprehensive theoretical and computational studies have been conducted in order to reveal deformation mechanisms during indentation and to extract reliable material properties from indentation experiments [99, 102, 104, 105]. It has been demonstrated that Young's modulus, E, and hardness, H, can be extracted from the slope of the linear portion of the unloading curve [34, 104] and that elasto-plastic properties (yield stress and strain hardening exponent) and residual stresses can be evaluated by considering both loading and unloading responses [99, 106, 107]. For small-volume structures, however, those comprehensive solutions are generally not feasible due to the additional boundary conditions such as the film/substrate interface and the free sidewall surface of patterned lines. In such cases, FEM has been used chiefly to fit experimental data by assumed material properties and boundary conditions.

A first example of comparison between FEM analysis and experimental results in thin films was presented by Bhattacharya and Nix [108], in which they simulated a submicrometer indentation test. These researchers verified that FEM could be an effective tool for simulating hardness measurements. Film/substrate systems with various combinations of film and substrate properties (*e.g.*, hard coatings on soft substrates or vice versa) have been studied using FEM [89, 100, 101, 109]. Sun *et al.* [110] employed an axisymmetric FEM model to simulate a hard coating on a softer substrate. In their study, the nanoindentation process for various coating-to-substrate yield strength ratios (σ_f/σ_s) was analyzed, including the effect of the indenter tip radius. Sun *et al.* found the critical depth, upon which the hardness of film begin to be affected by the substrate, was reduced by the increase of the yield strength ratio or of the tip radius. Recent numerical and experimental studies [91, 93] have shown that the effect of the substrate on film hardness was negligible in the case of soft films on hard substrates when the penetration depth was less than ~50% of film thickness. Substrate effects are especially pronounced for films which are harder than substrates, because much of the indentation penetration is accommodated by pressing the film into the substrate. However, in general, the effect of the substrate on the indentation response of the film is not clearly understood. Moreover, FEM simulations to examine the additional boundary conditions effect (*e.g.*, line widths) have not been attempted.

In this section, nanoindentation responses are simulated using FEM for continuous films and patterned lines on Si substrates. Various factors that can affect the indentation responses are examined, which include the yield stress of films and lines, indenter tip radius, and line width. Through comparing the simulated results to experimental observations in the previous chapter, limitations of a continuum-based approach in this range of nanoindentation length scales are discussed.

5.1.2 Finite element modeling

The finite element models used in these simulations was comprised of a three-dimensional indented body and a conical rigid indenter to simulate the load-displacement response of continuous films and patterned lines on Si substrates. The validity of the conical indenter geometry to simulate pyramidal indenters such as the Berkovich type has been verified by others [99, 108, 110]. Figure 5-1(a) schematically shows an ideal sharp, conical indenter and a conical indenter with a spherical tip, where h is the maximum indentation depth, a is the contact radius at h, and θ is the included half angle of the indenter, which is chosen to be 70.3 degrees to have the same projected area to depth relation of a Berkovich indenter.

The specimen is modeled only in a quarter space using 8-noded linear, reduced integration elements ($\sim$16,000 elements). Appropriate boundary conditions are imposed, and the semi-infinite nature of the substrate is achieved by $40\times40\times40$ μm system size (Since FEM has no length scale, all units are a relative length scale as compared to the tip radius and the film thickness). Repeated simulations showed that a system that is larger than 25 μm in all directions is sufficiently large to eliminate edge effects. The region of fine mesh near the contact area is designed to ensure numerical accuracy, and the minimum element size at the center of the indention axis is 7.6 nm along all three axes. The element size increases with increasing distance from the indentation axis and surface. At the maximum load, the minimum number of the contact elements in the contact zone is no less than 16 in each FEM computation. The mesh is well-tested for convergence and is determined to be insensitive to far-field boundary conditions. Computations are performed using the general-purpose finite element package ABAQUS [97]. The quarter space three-dimensional mesh is verified against the axisymmetric model for the continuous film case. Large deformation

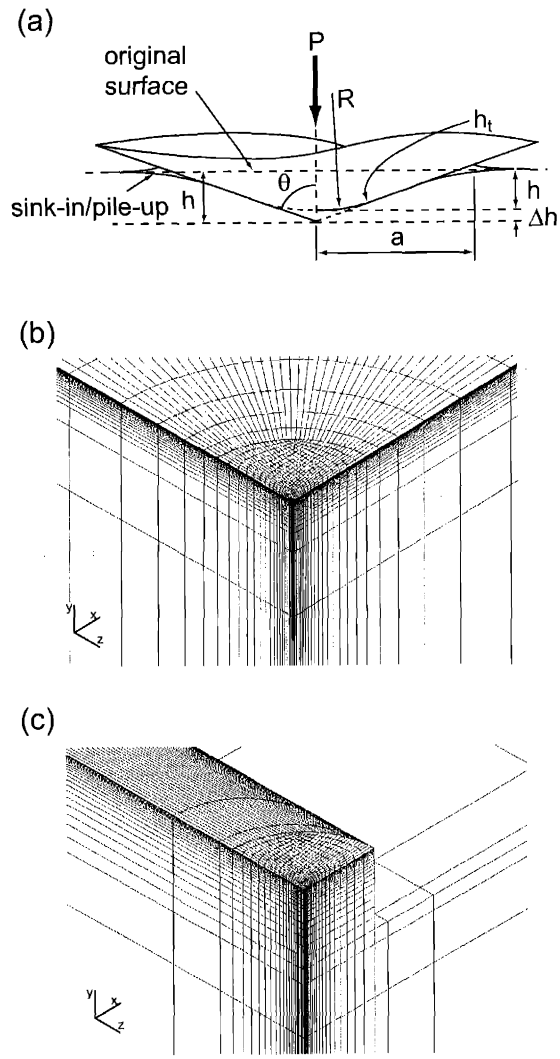

Figure 5-1: Computational modeling of nanoindentation. (a) schematic of a conical indenter with a sharp tip (left side) and a round tip (right side), where θ is the included half angle of indenter, a and R are the contact radius and tip radius, respectively. Detailed illustrations of mesh design near the indenter tip for the continuous films (b), and for the patterned lines (c) on substrates.

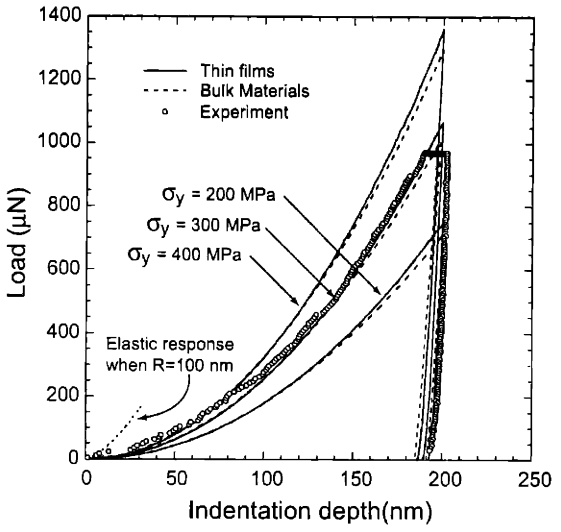

Figure 5-2: Simulated load-indentation depth (P–h) response of 1 μm thick Al films on Si substrates and bulk counterparts with the same yield stress. A typical experiment of a 1 μm thick Al film on a Si substrate is also plotted.

theory and frictionless contact between the indenter and material are assumed throughout the analyses.

Indentation was simulated via a complete, displacement-controlled loading and unloading cycle. During loading, the rigid surface of a modeled indenter tip moves along the negative y direction (see Fig. 5-1(b) and (c)) and penetrates the specimen up to the maximum depth; during unloading, the tip returns to the initial position. The von Mises yield criterion was applied to determine the onset of plastic deformation. All film and line materials were modeled as isotropic, elastic/perfectly plastic solids, where the elastic properties were fixed to represent aluminum (E = 70 GPa, ν = 0.33) and yield stress σ_y was varied to test hypotheses regarding deformation; perfect plasticity was assumed for mathematical simplicity. The properties of the Si substrate were fixed as a fully elastic solid (E=130 GPa, $\nu = 0.28$). The thickness of films and lines is fixed as 1 μm.

5.1.3 Simulation results of FEM

Nanoindentation of continuous films

FEM calculations for the load-displacement (P–h) responses of continuous films on Si substrates were carried out to illustrate the effect of the substrate (Fig. 5-2). The film thickness was fixed at 1 μm, and the maximum indentation depth was 0.2 μm. The corresponding P–h responses of bulk materials with the same yield stress and a typical experimental result of a continuous polycrystalline Al film of 1 μm thickness on a Si substrate are also shown in the figure. As seen in Fig. 5-2, the associated load at a given depth of penetration increases as the yield stress increases. At the early stages of indentation, the loading portions of P–h responses are essentially indistinguishable up to ~120 nm of penetration depth ($0.12t$) for films and their bulk counterparts. Moreover, the depth at which the film and bulk cases diverge increases slightly for the softer film. A typical experimental P–h curve, which was conducted by using a nominally sharp Berkovich indenter ($R \sim 100$ nm), agrees well with the simulated curve of $\sigma_y = 300$ MPa beyond the early stage of indentation, in which the P–h response is dominated by a series of discontinuities. Hereafter, a representative yield stress of the 1 μm thick continuous film is assumed to be 300 MPa, as the patterned lines were fabricated from the same continuous film. Thus it is neglected that the possibility that processing steps subsequent to film deposotion (*e.g.*, dry etching) may have changed the intrinsic yield stress of the lines.

As mentioned in the previous chapter, the effect of tip radius should be considered in this study since no indenter is atomically sharp and the indentation depth is comparable with the tip radius. This imperfection may be modeled by a conical indenter with a spherical tip. The side of the cone is assumed to be tangent to the sphere as shown schematically in Fig. 5-1(a). The tip geometry is determined by the tip radius, R, and the indenter half angle, θ. Specifically, the height of the tangent point from the tip end is given by;

$$h_t = R(1 - \sin\theta) = 0.0585R, \tag{5.1}$$

where θ is fixed as 70.3 degree for a Berkovich indenter. The depth difference between the sharp and rounded indenters, Δh in Fig.5-1(a) is given by

$$\Delta h = R(\frac{1}{\sin\theta} - 1) = 0.0622R. \tag{5.2}$$

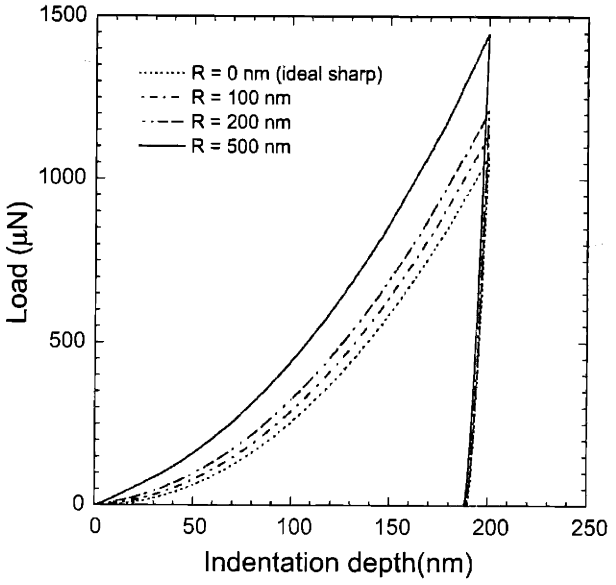

Figure 5-3: Simulated P–h response of 1μm thick Al films on a Si substrate with various tip radii. The yield stress of films is the same of 300 MPa.

Neglecting sinking-in and piling-up of surface profiles around the indenter, loading curves should follow that of a spherical indentation when $h/R < 0.0585$ and approach that of an ideally sharp conical indenter when $h/R \gg 0.0585$. When h and R are comparable, which is frequently encountered experimentally, loading curves are expected to deviated from that of a spherical or an ideally sharp conical indenter. FEM calculations are carried out to illustrate the changes in loading curves with varying R. As seen from Fig. 5-3, the deviation from the P–h response of an ideally sharp conical indenter increases with increasing R. The amount of deviations are appreciable in the range of this study although the h_t for a 500 nm tip radius is less than 30 nm. As observed experimentally, the force required for the indenter to reach a given penetration depth increases with increasing R. Furthermore, the loading part of P–h response can indeed deviate significantly from its predicted quadratic functional form.

Nanoindentation of patterned lines

Figure 5-4 shows the simulated P–h response with a sharp conical indenter on the continuous film, as well as on 2, 3, and 4 μm wide lines of the same 1 μm thickness on

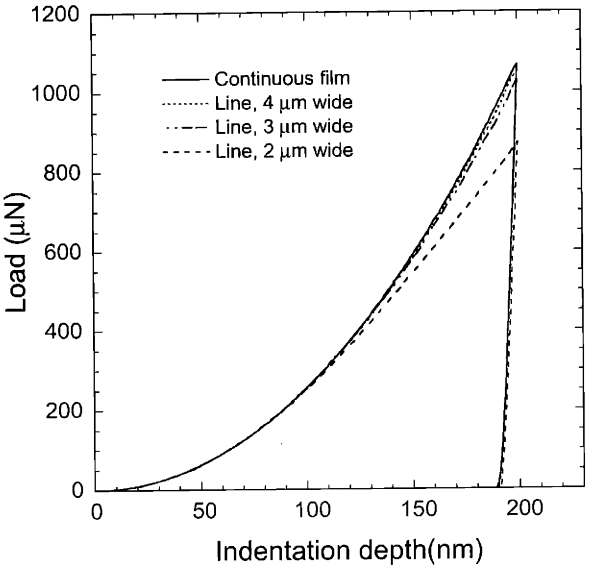

Figure 5-4: Simulated P–h response of continuous film and patterned lines of 2, 3, 4 μm width on a Si substrate. Thickness and yield stress of film and lines are the same of 1 μm and 300 MPa, respectively.

a Si substrate. The yield strength of the film and the lines is assumed to be 300 MPa. The P–h responses for film and lines of 3 and 4 μm width are essentially indistinguishable up to a load of $\sim$400 μN, such that differences may not be perceptible in practice due to experimental scatter. For the 2 μm wide line, the P–h response of the line begins to deviate from that of the film at a load of $\sim$300 μN ($\sim$120 nm in depth). Although the simulated FEM results on the lines exhibit a more compliant P–h response with decreasing line width, the magnitude of this compliance increase, even at higher load, is not sufficient to correctly capture the experimentally observed trends.

The effect of tip radius on the P–h response of a film and a 2 μm wide line of the same 1 μm thickness is shown in Fig. 5-5. The yield stress is 300 MPa for both the film and the line. The P–h response of the line begins to deviate at the similar indentation load of 300 μN, regardless of tip radius. For example, at a load of 750 μN, the penetration depth increases due to the line width effect are 14, 14, and 19 nm for tip radius of 0, 200, and 500 nm, respectively. That is, the penetration depth at a given load is not a strong function of R for the lines. The effect of yield stress on the P–h response for films and lines of 2

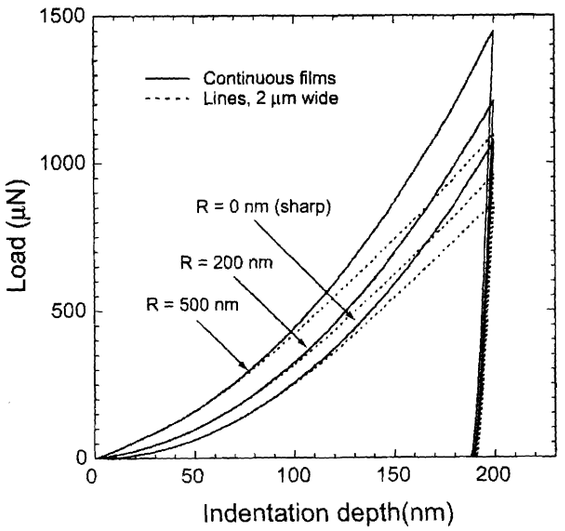

Figure 5-5: Effect of tip radius on the simulated P–h response of continuous film and patterned line of 2 μm width on a Si substrate. Thickness and yield stress of film and lines are the same of 1 μm and 300 MPa, respectively.

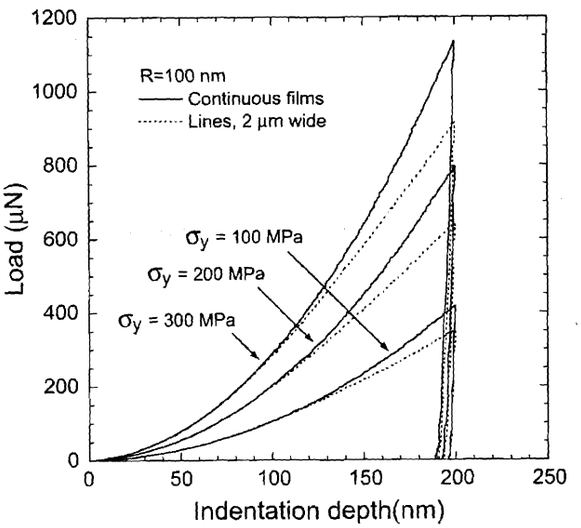

Figure 5-6: Effect of yield stress on the simulated P–h response of continuous film and patterned line of 2 μm width on a Si substrate. Film and line thickness is 1 μm, and the tip radius is 100 nm.

μm width is shown in Fig. 5-6 when the tip radius R = 100 nm. The yield stress effect on the curvature of loading portion of P–h responses is apparent even at the early stage of indentation for both films and lines, and the limits at which the P–h responses of the lines start to deviate from those of the films increase in load, but decrease in depth as the yield stress increases.

5.1.4 Correlation with experiment

The effect of tip radius on nanoindentation of continuous films, particularly during the transition period from the elastic to the continuous plastic response by a series of discontinuities, is evident when the P–h responses are plotted on a log-log scale. Two experimental P–h responses are shown with the FEM simulated elasto-plastic indentation results (solid lines) for different tip radii in Fig. 5-7. The analytical Hertzian solutions [Eq. (4.1)] of spherical indentations (dashed lines) with various indenter tip radii are also shown. The yield stress of the film for FEM simulations is fixed at 300 MPa, and the tip radii vary from R=0 to 500 nm. The effect of tip radius in experiments is pronounced for both elastic and elasto-plastic regime. The indentation load at the first displacement discontinuity, which may reflect the subsurface, homogeneous nucleation of dislocations, can be calculated as [86]:

$$\tau_{\max} = 0.31 \left(\frac{6PE^{*2}}{\pi^3 R^2} \right)^{1/3} \tag{5.3}$$

where P is the indentation load, and E^* is the reduced Young's modulus which accounts for elastic deformation of both the indenter and the sample. Equation (5.3) indicates that a larger tip radius requires a greater load to nucleate the dislocation homogeneously, as clearly indicated in Fig. 5-7. The critical loads for the first discontinuity are 17.8 and 28.3 μN for a sharp and a rounded indenter tip, respectively. The critical shear stress beneath the indenters are calculated as 3.8 and 1.5 GPa, respectively, using Eq. (5.3). These stress values are much higher then the value of yield stress, and approximately the theoretical shear stress of Al ($\sim$2.7 GPa). The ensuing changes of P–h responses approach the elasto-plastic predictions by FEM simulations. The penetration depth difference in this transition region is evident, and the sharper tip shows larger penetration depth for a fixed load.

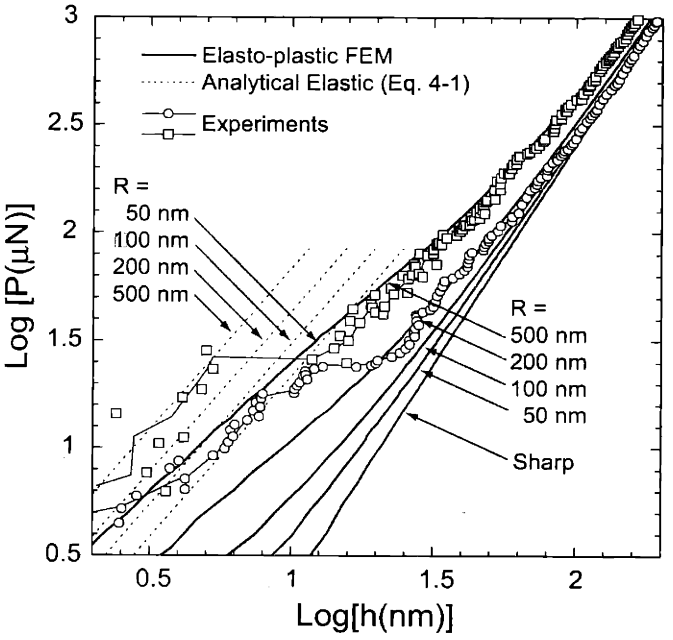

Figure 5-7: Load-displacement (P–h) response of continuous film of 1 μm thickness on a Si substrate in the log-log scale. Dashed lines indicate the analytical elastic P–h responses of spherical indentation from Eq. (4.1) with various tip radii, and solid lines indicate the elastic-plastic FEM simulations with spherical tips. Symbols represent two experimental indentation responses with two different tip radii.

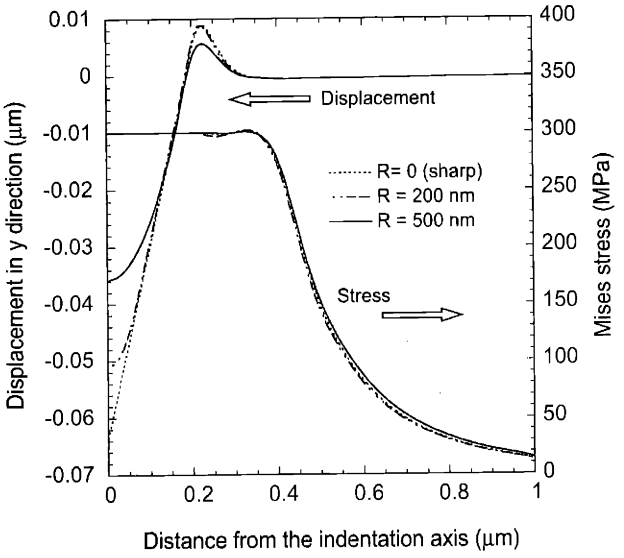

Figure 5-8: Mises stress and deformed surface profile around indenters with different tip radii as a function of the distance from the indentation axis at a fixed indentation load of 100 μN.

The FEM-calculated plastic zone and deformed surface profile of films beneath the indenters with different tip radii are illustrated at a fixed load of 100 μN in Fig. 5-8. Deformed surface profiles around the indenters are almost identical, except near the region of the indenter tip due to the different tip radii. The case of $R = 500$ nm shows slightly less pile-up around the indenter perimeter, but the plastic-zone sizes are the same for all three values of R. This observation clearly indicates that the opposing force of the indented material in response to the indenter does not concentrate at the tip end, but is evenly distributed over the whole contact area. This result supports the concept that the average indentation pressure is a representation of the material's resistance to indenter penetration [86]. It is also interesting to note that the depth difference between different tip geometries can be evaluated by Δh in Fig. 5-1(a) and Eq. (5.2), neglecting piling-up of surface profiles around the indenter. After correcting the penetration depth by Δh, all P–h curves in Fig. 5-3 collapse onto a single P–h curve for the relatively large penetration depth.

FEM simulated P–h responses of patterned lines with the same yield stress as the

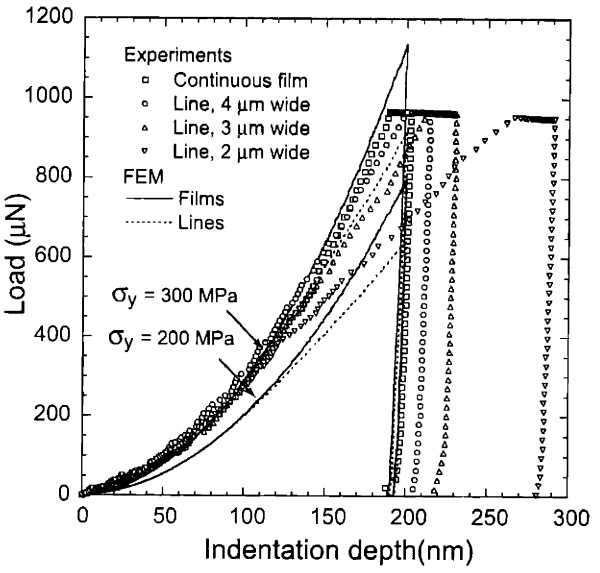

Figure 5-9: Load-displacement P–h response of continuous film and patterned lines. Symbols are experiments with a relatively sharp tip, and lines are FEM simulated response with tip radius of R=100 nm on a continuous film and a 2 μm wide patterned line on a Si substrate.

continuous film have failed to explain such a large increase in compliance under indentation. Thus, the FEM simulated P–h responses of lines with different yield stresses have been tried and compared with experiments in Fig. 5-9. Experimental P–h curves represent typical nanoindentation experiments with a relatively sharp indenter tip ($R \sim$ 100 nm) on a continuous film and patterned lines of 2, 3 and 4 μm line width. FEM simulations are carried out on the film and 2 μm-wide line with yield stresses of 200 and 300 MPa. The curvature of the experimental curve seems to approach the simulated curve of the line with 200 MPa yield stress for line width of 2 μm, at a relatively large penetration depth (h >150 nm). However, the P–h response in the early part of indentation (h <150 nm) is almost indistinguishable from FEM-simulated curve with 300 MPa yield stress, which is the same as the yield stress of the film. Since the loading curvature difference with yield stress in the P–h responses is apparent even at the very early stage of indentation, the decrease of the yield stress with decreasing line width is not the factor responsible for the line-width effect. Again, the significant number of discontinuities in the very early stages of indentation responses, which relate to the discrete motion of dislocations, also prevents

straightforward interpretation of the increase in compliance of lines with decreasing σ_y.

5.2 Atomistic Simulation of Nanoindentation

5.2.1 Introduction

Atomic scale simulations such as molecular dynamics (MD) calculations of nanoindentation can simultaneously provide the details of the evolving defect charaterization and load-displacement (P–h) response over a well defined, though limited, time period. Several researchers have modeled nanoindentation of 3-D, face-centered cubic crystals and observed dislocation activity [111, 112]. However, the length scales in such studies are limited by computational resources, resulting in unrealistic system dimensions and strain rates which are incongruous with those attainable in experiments. Even when computational analyses incorporate multiple length scales to approach realistic dimensions, such as in the quasi-continuum method [113], the observations have not been sufficiently well-calibrated against experiments and do not culminate in predictive capabilities. Despite these limitations, MD can be used to assess the effects of boundary conditions on atomistic processes such as dislocation plasticity, and is particularly well suited to the investigation of small volume structures such as patterned lines.

Recently Van Vliet *et al.* [30, 88] related experimental and atomistic computational analyses of nanoindentation which were designed together to elucidate the mechanisms by which localized contact can induce the transition from elastic to plastic deformation in an initially defect-free crystal, and by which that plasticity proceeds in the early stages of nanoindentation. This framework can be extended to the long-standing problems in the initiation of deformation and plasticity beyond the narrow context of indentation. Nevertheless, the effects of various geometrical boundary conditions (*e.g.*, film thickness and line width) on the early stage of nanoindentation have not yet been addressed, including before and beyond the first load or displacement discontinuity. Moreover, the results from the previous section indicate that the continuum mechanics-based approach via FEM has a limited capability to explore the range of nanoindentation experiments in which the discrete discontinuities are dominant. Thus, it appears that the atomistic-scale simulation can be considered a plausible approach to explicate the deformation mechanism by which the early stage of nanoindentation is governed and the effect of those boundary conditions on that

mechanism.

Here, two- and three-dimensional (2-D and 3-D) MD simulation results are presented to demonstrate the effects of size and constraint (boundary conditions) on the early stage of nanoindentation. The goal of the present section is to understand qualitative trends in nanoindentation experiments by simulating P–h responses in a model crystal, rather than to duplicate the exact experimental results. Thus, various simulation sizes and constraints (boundary conditions) are imposed on the MD simulation to examine the corresponding effects on the nanoindentation response (the first and subsequent discontinuities) in a 2-D model crystal. Then, nanoindentation on a 3-D FCC metallic crystal is simulated to extend and verify the trends extracted from 2-D simulation results. Details of the simulation are described in refs. [30, 88]. In all simulations, indentation proceeded in displacement control. Thus, discontinuities in the P–h response appear as sharp decreases in load, rather than as large bursts in displacement.

5.2.2 MD Simulation of indentation on a 2-D crystal

In order to simulate the effect of various boundary conditions on the nanoindentation response at the atomistic scale, a MD code originally developed to simulate the bubble-raft experiments outlined in Refs. [87, 88] has been modified to ensure the application of those boundary conditions. The goal of this simulation is not to replicate the exact P–h responses during actual nanoindentation experiments, but instead to learn about the effect of boundary conditions on the indentation response by regarding this atomic configuration as a generic model of close-packed 2-D crystals. Thus, the following interatomic potential is adopted with a short range, smooth cut-off mathmatical function for ease of implementation,

$$V(r) = \begin{cases} \alpha(r-1)^4 - \beta(r-1)^2, & r < 1 \\ 0, & r \geq 1 \end{cases}, \tag{5.4}$$

where $\alpha = (1 - r_\circ)^{-4}$ and $\beta = 2(1 - r_\circ)^{-2}$, respectively. The primary units of length and energy, cut-off distance R_c and potential well depth ϵ, are both scaled to unity. We normalize the distance by R_c valued unity, so that $r_\circ$ is a dimensionless quantity less than

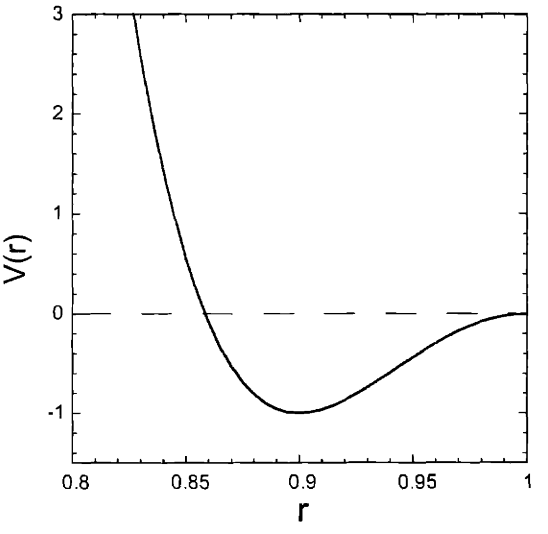

Figure 5-10: Short-range interatomic potential with equilibrium separation distance $r_o = 0.9$. Both the potential-well depth and cut-off distance are set to unity and serve as normalizations of energy and length, respectively.

unity. Consequently, a single parameter r_o, the equilibrium inter-atomic distance, controls the shape of the potential. In order to convert from these normalized values to physical units in actual experiments, one multiplies normalized quantities by physical measures of ϵ and r_c. The quantities, α and β, modulate the potential. When $r_o = 0.9$, Eq. (5.4) is shown in Fig. 5-10.

As r_o decreases, the crystal exhibits more brittle behavior. In all the following results, r_o is taken to be 0.9, and plots of potential and depth are shown in these reduced units. When the material undergoes only elastic deformation, the stresses and strains are related by Hooke's Low. For isotropic elastic response,

$$\sigma_{ij} = \mathrm{C}_{ijkl}\varepsilon_{kl}, \qquad \mathrm{C}_{ijkl} = \lambda\delta_{ij}\delta_{kl} + \mu(\delta_{ik}\delta_{jl} + \delta_{il}\delta_{jk}), \tag{5.5}$$

where C_{ijkl} are the elastic constants, λ is known as the Lamé constant, μ is the shear modulus, and δ_{ij} is the Kronecker's delta, respectively. By considering the strain energy at

Table 5.1: Conditions of molecular dynamics simulation for 2-D crystals.

Code	w^a	t^a	No. of atoms	R^a	PBC^b
F1R1	414	234	108,000	29	On
F2R1	324	156	72,000	29	On
F3R1	324	78	36,000	29	On
L1R1	324	156	72,000	29	Off
L2R1	234	156	52,000	29	Off
L3R1	171	156	38,000	29	Off
F2R2	324	156	72,000	87	On
L1R2	324	156	72,000	87	Off
L2R2	234	156	52,000	87	Off

[a] w = line width, t = film/line thickness, and R = indenter tip radius are given in reduced units.
[b] PBC = periodic boundary condition.

uniform strain, elastic constants, λ and μ, are evaluated as:

$$\lambda = \mu = \frac{2\sqrt{3}}{(1 - r_0)^2}, \tag{5.6}$$

and the Poisson's ratio ν is therefore 1/3. When we define the equilibrium separation distance $r_0 = 0.9$, we obtain λ=μ=346.4 in reduced units. The infinitely rigid indenter is implemented as an external potential field with the radius R. The potential increases from 0 infinitely smoothly upon contact with atoms, but rises precipitously when the atom penetrates a pre-defined distance inside the indenter. As such, there is zero friction between the indenter and the substrate, and the indenter represents a very rigid indenter. A vacuum environment surrounded the simulation cell, and temperature was 0 K, as maintained via a Berendsen thermostat [114]. The atomic mass is arbitrarily chosen to be valued 1.

Two-dimensional crystals were constructed by a portion of a {111} plane, and indentation was conducted along the $\langle 11\bar{2} \rangle$ direction. The maximum indentation depth was less than 10% of the film thickness t. The motion of atoms in the bottom layer was fixed, implementing the rigid film/substrate interface boundary condition. The interface was parallel to $\langle \bar{1}10 \rangle$ direction. In-plane periodic boundary conditions (PBC), perpendicular to the indentation direction, were imposed for nanoindentation of films, and were de-activated for nanoindentation of lines to allow the free motion of atoms on the surface of line sidewall.

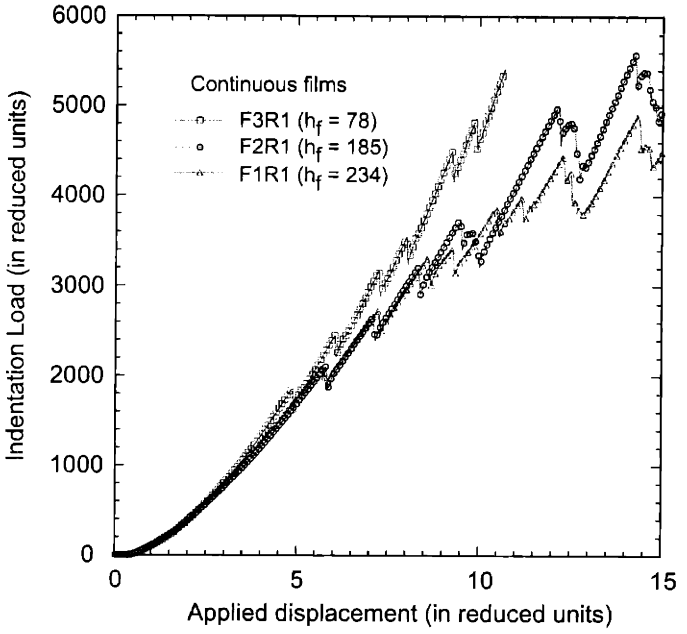

Figure 5-11: Effect of film thickness on the MD simulated nanoindentation responses. The indenter radius is 29 in reduced units.

The interatomic potential employed here does not reflect the interatomic potential of Al. The simulation setup and boundary conditions are summarized in Table 5.1.

5.2.3 Correlation of 2-D MD simulation with experiment

Effect of film thickness

Figure 5-11 shows the change in far-field indentation load as a function of the simulation cell thickness, which represents film thicknesses. Since the primary units of length (r_c) and energy (ε) of the interatomic potential in the model 2-D simulations have been normalized to equal one, all quantities are presented in the reduced units. The indenter was cylindrical with a radius R of 29 in reduced units. For both of the thicker films simulated (h_f= 185 and 234), the initial elastic responses are almost identical up to the second dislocation burst. The critical indentation load for the first homogeneous defect nucleation event is ~2100 at a applied depth of 5.73, in reduced units. The maximum shear stress underneath the cylindrical indenter is a value of 45.4, which is 13% of the calculated shear modulus, and

is close to the estimated theoretical shear strength of this set of atoms ($\tau_c = \mu/(2\pi) = 55.1$). It is verified that each load relaxation in Fig. 5-11 corresponds to a sequence of dislocation dipole nucleation through the visualization of the atomic coordination number. This dislocation structure is a function of the 2-D constraint of the simulation. The deviation of the thinnest film case ($h_f = 78$) from the predicted elastic response arises from a strong substrate effect: the stress field imposed by the indenter approaches the film/substrate interface even prior to the first observed discontinuity.

After the first load relaxation, which corresponds to subsurface dislocation dipole nucleation, the dislocation dipole separates. One dislocation moves to the surface, making a surface step, and the other quickly moves into the material. Once a dislocation nucleates and moves way, the local stress (*i.e.*, the stress in the region near the position of dipole nucleation) decreases by a certain amount, which relates to the relaxation in the far-field external load. The force balance determines the equilibrium position of the dislocation. The force imposed on the dislocation includes the repulsive stress field imposed by the indenter and the repulsive stress field due to the elastic mismatch at the film/substrate interface. Due to the fixed position of the bottom layer, the imaginary substrate has an infinitely large elastic modulus, which repels the dislocation from the interface. In order to nucleate subsequent dislocations homogeneously, the local stress must increase again to the GPa level. As the contact width increases (*i.e.*, as indentation depth increases), the load required to reach this stress level increases. In addition, since the previously nucleated dislocation asserts a stress field on the region of maximum shear stress beneath the indenter, the external loading to create another dislocation is altered by the back stress of this pre-existing dislocation. Therefore, thinner films sustain larger external loads subsequent to the first dislocation nucleation event because of greater back stress: Increased proximity of the (repulsive) substrate interface causes previously generated dislocations to remain closer to the indenter tip. The overall load-displacement relation becomes less compliant when the film thickness decreases, as the film effectively hardens more readily.

Effect of line width

The effect of line width on the MD simulated P–h response is illustrated in Fig. 5-12. As expected, soon after the first deviation from the elastic behavior occurs, the indentation

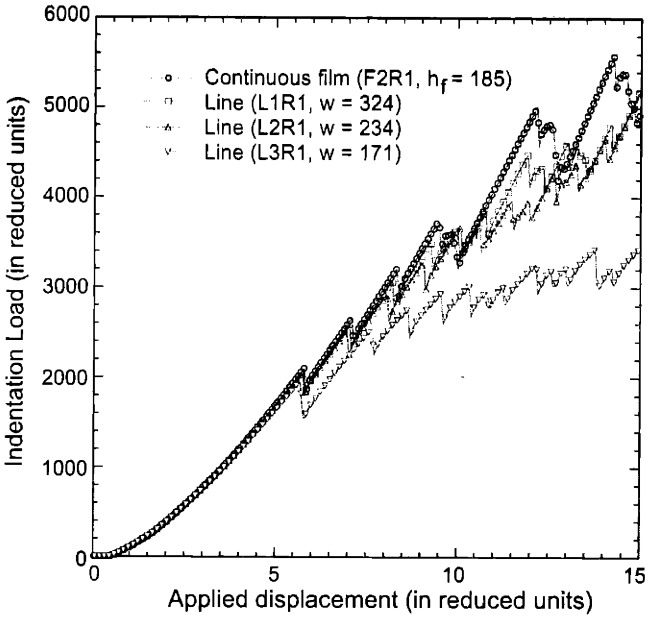

Figure 5-12: Effect of line width on the MD simulated nanoindentation responses. All units are in reduced unit. Thickness of film and lines are 185 and the indenter radius is 29, respectively, in the reduced unit.

responses show increasing compliance with decreasing line width. Unlike the effect of film thickness, the elastic responses prior to the first deviation are the same for all three line widths because the initial stress field does not approach either the substrate interface or the free surface of the line sidewall. The effect of line width is evident in subsequent P–h responses after several dislocations have been generated and have moved away from the indenter tip. As argued above, the back stress from the previously generated dislocations alters the far-field external loading, and, in the case of lines, the free surface of the line sidewall decreases the effective back stress from dislocations to the indenter tip. In these lines, dislocations move to the free surface to relieve the external loading stresses, rather than to the substrate interface where they would contribute to back stresses that would increase the external loading required for further deformation.

Effect of tip radius

The MD simulated P–h responses of films and lines of two distinct widths are illustrated for the indenter tip radii of $R = 29$ and $R = 87$ in Fig. 5-13. As predicted by [Eq. (5.3)],

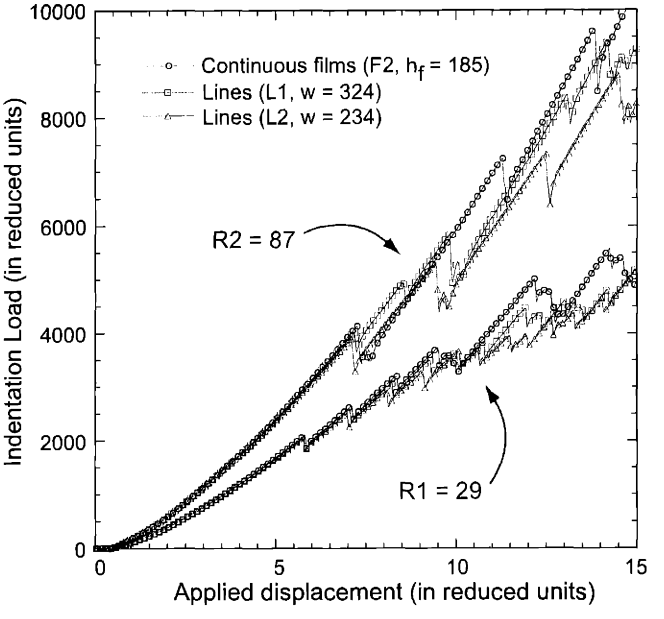

Figure 5-13: Effect of tip radius on the MD simulated nanoindentation responses. All units are in reduced unit. The simulations are conducted on a film and lines of two widths with the tip radius of $R = 29$ and $R = 87$ in the reduced units. Film and line thickness are the same of 185 in the reduced units.

the critical indentation load to nucleate the defects is higher for the larger indenter radius. The maximum shear stresses at the first dislocation nucleation events are 45.7 and 36.7 for $R = 29$ and $R = 87$, respectively, which are 13% and 11% of the shear modulus ($\tau_c = 55.1$). Note that compliance increases with decreasing line width, and also increases rapidly with increasing R. This result is not predicted for a continuous film or bulk material, and appears to be an effect of the unique boundary conditions of the line. In continuous films and bulk samples analyzed by recourse to continuum description, increasing R correlates with decreasing stress for a given indentation load, and thus compliance decreases with increasing R. This difference points to the interaction between the boundary conditions and the indentation stress field: As the plastic zone of indentation approaches the dimensions of the line, the sidewalls facilitate stress relaxation and the line appears to deform more readily than film or bulk counterparts.

5.2.4 MD Simulation of indentation on 3-D crystals

Although 2-D molecular dynamics (MD) simulations can afford insight into the initial stages of nanoindentation and the effects of various constraints, these computations cannot be compared directly to experimentally observed nanoindentation behavior because (1) dislocation structure is limited to (1D) edge dislocations; (2) the restricted dimensionality of these dislocations confers artificially high mobility; and (3) the P–h response does not converge (*i.e.*, it is dependent on the size of the sample). Previous 3-D MD simulations [88] have shown that dislocations and defects intersect to form complex structures beneath the indenter tip, including the formation of sessile locks due to the concurrent nucleation of dislocations on adjacent slip planes in Al subject to spherical nanoindentation. These sessile locks can serve as heterogeneous nucleation sites for defects in the subsequent stage of nanoindentation. Thus, to extend 2-D simulations, 3-D MD simulations of spherical indentations have been performed for a spherical indentation of Cu comprising 90,000 atoms. We chose to model Cu rather than Al because the accuracy of the Mishin Cu embedded atomic potential [115] at large strains has been confirmed independently [116]. However, it should be noted that the stacking fault energy and elastic anisotropy of Al and Cu differ substantially. A sphere of 4 nm radius was used to indent normal to {111} plane of the defect free Cu single crystal in displacement control. The simulation size was $8.85 \times 9.39 \times 12.78$ nm in $x, y,$

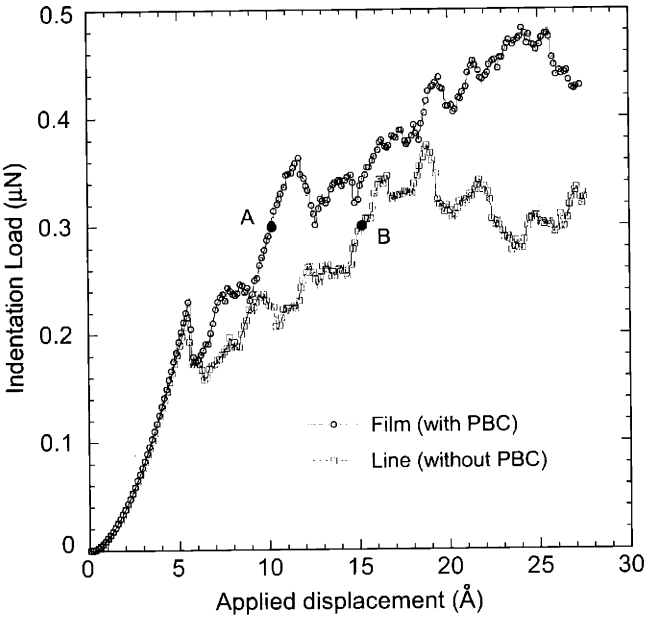

Figure 5-14: MD simulated load-displacement (P–h) responses of 3-D Cu crystal comprising 90,000 atoms. A sphere of 0.4 nm radius indents normal to the {111} plane of the defect-free crystal of Cu. The simulation size is 8.85 nm×9.39 nm×12.78 nm. The displacement rate of the indenter is 12 m/s.

and z directions, respectively. The displacement rate of the indenter was 12 m/s along the negative y direction. The bottom of $y = 0$ plane is fixed to simulate a rigid substrate. The periodic boundary conditions (PBC) along the x-direction were de-activated to simulate the patterned line structure of the same dimension.

Figure 5-14 shows that the P–h response of the system with and without PBC along the x-direction, which represent a continuous film and a patterned line on a substrate, respectively. In all simulations, the initiation of dislocation activity was concurrent with far-field indentation load relaxation, and the dislocation structure comprised a dislocation glide loop on {111} slip planes. As expected, the indentation response is identical for both cases, up to the first load relaxation (*i.e.*, within the elastic regime). After the first deviation from the elastic response, dislocations nucleate inside the material near the top surface and generate loops in the {111} slip planes. Further load relaxation is mediated by expansion of these glide loops in the slip planes. The expanding glide loops intersect the surface, and

generate the ⟨110⟩ slip steps. The subsequent P–h response indicates clear differences in the behavior of the film and line cases. The defect structure underneath the indenter is shown for both cases in Fig. 5-15 at a load of 0.3 μN, corresponding to points A and B in Fig. 5-14. Atoms having the perfect bulk coordination number, 12, are not shown here for ease of visualization. For the film case, those dislocations generated by the contact are entangled beneath the contact area. The density of defects is higher than that of the line case, which results in a higher rate of strain hardening during indentation loading. In contrast, the volume of the defect structure for the line case is larger (*i.e.*, lower defect density), and some dislocations escape from the free surface of the line sidewall and form several ⟨110⟩ slip steps. Note that the presence of these sidewall slip steps correlates with the decreased density of dislocations beneath the contact zone and on the top surface of the line (compared to the film case), facilitating a relative increase in the penetration depth sustained by the line structure. The anisotropy of such slip step formation may be related to the elastic anisotropy of the Cu crystal.

5.3 Discussion

The simulation results from the previous section indicate that the continuum approach via FEM has a limited capability to explore the range of nanoindentation experiments in which the discrete discontinuities are dominant. Although FEM can consider more realistic dimensions, and the quasi-static nature of nanoindentation loading, the simulated indentation responses are insufficient to reproduce the overall experimental trends at the nanoscale, whereas MD simulations of 2D perfect crystals clearly exhibit the general trends observed experimentally. This suggests that the plastic deformation in the range examined herein is governed by an atomistic (*discrete*) mechanism rather than a mechanism explained by continuum concepts. However, the mobility of dislocations in 2D crystals is artifactually high due to the lack of out-of-plane constraints, and the number of dislocations examined is quite low ($\leq$ 20), compared to the number expected in the real experiments (>150). In 3D simulations, the cluster of defects expanded much more in the lateral directions than observed in 2D simulations, due to the entanglement of concurrently generated dislocations in adjacent slip planes. Some of these dislocations indeed escaped to the line sidewall,

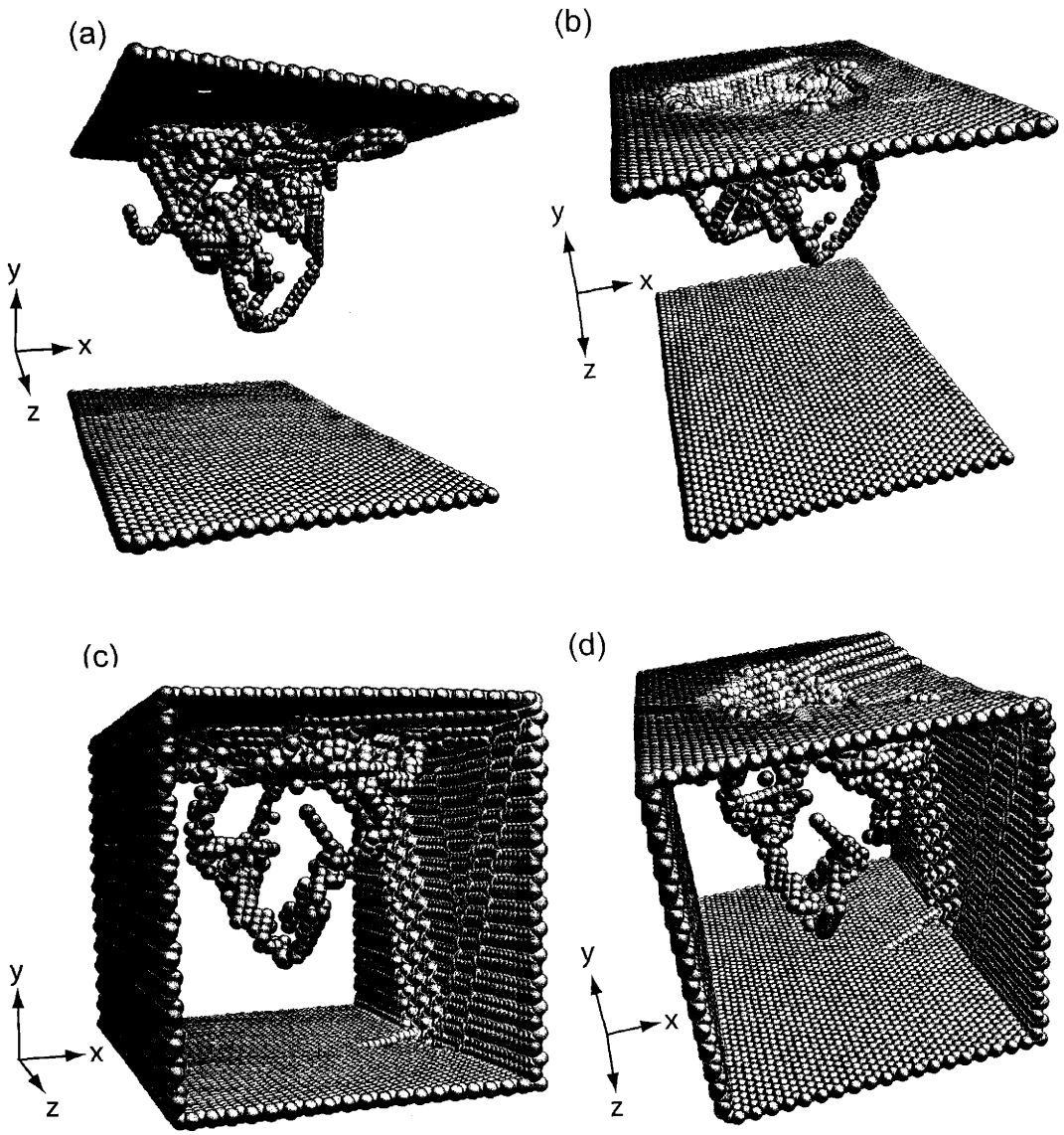

Figure 5-15: Defect structures underneath indenters for (a) the film case and for (c) line case at a load of 0.3 μN (denoted as points A and B in Fig. 5-14). (b) and (d) are the rotated views of (a) and (c), respectively, to reveal features on the top and side wall surfaces. In both cases, $x = \langle 11\bar{2} \rangle$, $y = \langle 111 \rangle$, $z = \langle 1\bar{1}0 \rangle$.

and facilitated penetration of the indenter by depositing slip steps in addition to those on the top surface of the line. Consequently, the size of the defect zone, or volume occupied by defects, is larger in the patterned line than in the continuous film. Beyond the region of discontinuities, continuum approaches should prevail, a feature which has already been validated by others [99–101]. It should be noted that there is no effect of geometrical constraints on the elastic response of nanoindentation prior to the first discontinuity in this small scale deformation.

In Fig. 5-16, schematics of dislocation configurations at the initial stages of indentation for a bulk material, a continuous film, and a patterned line on a substrate are illustrated. At this stage of deformation, the number of generated dislocations may not be enough to be treated corporately as in the continuum mechanics domain so that it must be done discretely. Since there are no geometrical boundary condition effects in the bulk, the equilibrium position of dislocations is established by only the indentation-induced stress field and the internal resistance in the lattice, such as the Peierls-Nabarro barrier. Even in this case, the dislocations can extend beyond the continuum-predicted plastic zone boundary as illustrated in Fig. 5-16(a). In the case of continuous films on a substrate for which the elastic modulus exceeds that of films, the equilibrium position of extended dislocations is nearer to the film surface due to the repulsive force from the elastic mismatch of the film/substrate interface [117]. Therefore, the extension of dislocations is limited, such that the stress field from these dislocations modifies the stress field of the critical region underneath the indenter where the next dislocation will be generated. Such back stress originating from the film/substrate interface is eventually responsible for the increase of the external loading of indentation. In the case of patterned lines, however, the free surface of the line sidewall affects the equilibrium position of dislocations and the stress field of the critical region in the opposite manner: As some dislocations can generate slip steps at the sidewall surface, the far-field indentation load decreases, and the lines deform more compliantly under the same indentation load.

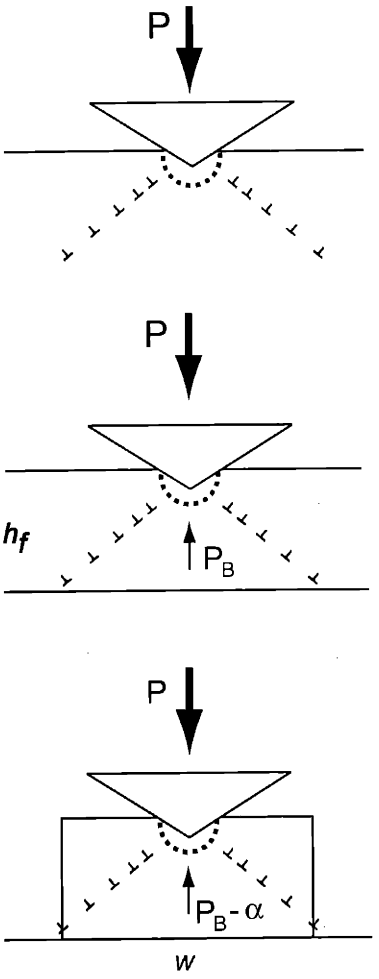

Figure 5-16: Schematics of dislocation configuration during the initial stage of indentation for a bulk material, and a film and a line on a substrate.

5.4 Conclusions

In this work, the systematic investigation on the size scale effects on the early stages of nanoindentation-induced plasticity has been conducted via experimental and computational approaches. It is evident that there is no size effect on the elastic load-displacement (P–h) responses. Beyond the onset of plasticity, two size scales (film thickness and line width) exhibit distinct effects on the P–h responses, depending on their geometric constraints; the bottom of films is constrained by film/substrate interface, but the sidewall surfaces of lines are free to deform. The indentation penetration depth decreases as the film thickness decreases (plastically less compliant) for the continuous films, whereas the penetration depth increases as the line width decreases (plastically more compliant) for the patterned lines.

Through computational simulations with concomitant experimental observations of nanoindentation, we have shown that the early stage plasticity of small volume structures is described more accurately by discrete dislocation interactions than by continuum concepts. These results indicate that individual defects and their interaction with boundary conditions become important in this extremely small-scale deformation, and that the stress arising from those defects counters the far-field applied load. The resistance to indenter penetration is determined by the force balance between the applied stress field imposed by the indenter and the stress field imposed by the dislocations in their equilibrium position. For continuous films, increased proximity to the film/substrate interface (decreasing film thickness) causes greater resistance to the indenter penetration due to the repulsive stress field of previously generated dislocations by the elastic mismatch at the interface. In contrast, the existence of free sidewall surfaces in patterned lines reduces this repulsive stress field. Under these reduced constraints, dislocations relieve stress due to external loading by terminating at the sidewall surfaces, resulting in greater penetration depth of indentation and an apparent increase in plastic compliance.

Chapter 6

Concluding Remarks and Suggestions for Future Work

The implication of this thesis work can provide a new frame of view on the length-scale effect on stress state and deformation behavior of materials in small-volume structures, particularly thin films and patterned lines of metallic materials on substrates. The stress evolution and inelastic deformation of those materials are governed by the generation and motion of dislocations, which is strongly affected by the microstructural and physical length scales of materials. Experimental, analytical, and computational approaches adopted in this thesis demonstrate that the equilibrium distribution of individual dislocations (or a set of dislocations) relates to the deformation behavior of materials in small volume structure. Those distributions are tailored by the loading conditions (uniform vs. localized) and various confinements of length scales. The key results of this thesis are:

1. A simple analytical model based on a set of dislocation loops can be used to rationalize a variety of experimental observations of thin polycrystalline metal films on substrates. The confinement of dislocations within small thin-film grains and the interaction energies among dislocations play a key role in the stress evolution of thin films on substrates. The model successfully predicts the overall trends pertaining to the effect of length scale, such as film thickness and grain size, on the stress evolution in film–substrate systems. Through the comparison of previously published experi-

mental data of Al and Cu films (with different thickness and grain size) on substrates, the stress–temperature curves of those films upon cooling from a high temperature can be estimated without considering the possibility of rate-dependent processes such as diffusional creep. The model is also able to predict the film texture effect (crystal orientation effect) on stress evolutions. The present approach demonstrates the strong coupling between the dependence of film stress on two key length scales: the film thickness and the grain size of the film.

2. Length-scale effects on the stress evolution are closely related to the increased strain hardening behavior of thin-film systems, which is caused by the confinement of dislocations within a small volume of thin-film grains. Since the model predicts dislocation densities of thin films increase as the film thickness and grain size decrease, strain hardening due to high dislocation densities can be considered as an important source of thin-film strenghening. This confinement of dislocations leads to rapid development of the back stress even at small plastic strains. In conjunction with the Bauschinger effect analysis, the phenomenological constitutive law based on the kinematic hardening model successfully represents the stress–temperature hysteresis of an Al film on a Si substrate, over different thermal cycles.

3. In contrast to the uniform loading conditions in the thermal excursions of thin-film systems, the first systematic nanoindentation experiments on patterned lines on a Si substrate reveal the effect of the free boundary on the elastic and inelastic deformations of these small volume structures. Although a quasi-quantitative analysis is applied to nanoindentation of continuous films and patterned lines of Al on Si substrates because of the discontinuities and large scatter in the load-displacement responses, the experimentally observed behaviors with the penetration depth at a fixed load as a measure of the indentation can be summarized as follows. Firstly, In spite of large experiment scatter, the overall trends of experiments can be captured via an appropriate statistical analysis. Those scatter may arise from several factors, such as polycrystalline nature of specimens, surface roughness, different dislocation nucleation sources, obstruction of dislocation movement, and instrument configurations. Secondly, there are no length scale effects on the elastic response of indentation prior to the first discontinuity prior to the initiation in plasticity. Thirdly, The inelastic

deformation of thicker films and narrower patterned lines is more compliant during nanoindentation, exhibiting larger penetration depth at a fixed load of indentation. This suggests a strong effect of boundary conditions on the motion and equilibrium position of dislocations, which can modify the far-field indentation load. Lastly, the indenter tip radius seems to play a role in the effect of length scale on nanoindentation experiments. The indenter with smaller tip radius shows larger penetration depth on continuous films, and is less sensitive to changes in line width.

4. The simulations via Finite Element Method (FEM) and Molecular Dynamics (MD) calculations, correlated with experimental observations, suggest that the length scale effects on the initial stage of nanoindentation can be better described by the discrete atomistic description rather than by the continuum concepts of material deformation. Although FEM can construct more realistic experimental length and timescale, including specimen and indenter size, tip radius, and loading rates, the simulated load-displacement (P–h) responses with various boundary conditions are insufficient to capture the observed experimental trends. In contrast, MD-simulated indentation responses clearly capture those length scale effects on the early stage of nanoindentation responses in spite of the inherent limitation of this method, such as nano-sclae simulation size and high loading rates. This result indicates that the role of individual defects becomes important in this nano-scale deformation, and that the stress field resulting from those defects configuration affects the far field applied load. The geometrical boundary conditions, such as the film/substrate interface and the free surface of the patterned lines, strongly modify the configuration of defects, and, subsequently those collective back stress from the combined stress field of defects affect the deformation behavior of materials.

As materials deform plastically, the defects within the materials must accommodate the deformation in an irreversible way. The main achievement through this study herein is that we demonstrate the effect of materials length scales on the generation and movement of dislocations and subsequent mechanical responses of materials when they are in a small scale. The analytical dislocation model based on the dislocation loop structure confined in the film grains predicts the film thickness and grain size effect on the stress evolutions of various thin film systems on substrates upon cooling from the high temperature. The resulting

consequence of increased strain hardening leads to the prediction of full hysteresis stress-temperature curves of an Al film on a Si substrate through the kinematic hardening law. In the present study, no time dependent phenomena have been considered. However, thermally activated processes leading to stress relaxation must be taken into account in order to broaden the scope of the model developed here for those metal films not covered by a native oxide or an effective passivation layer. Although the correspondence between experiments and predictions of model indicates that the assumed dislocation structure is a plausible model of thin polycrystalline films (with thickness and grain size on the order of μm's), the configuration of dislocations is chiefly responsible for the unique mechanical behavior of these system. Thus, more detailed microscopic observations of dislocation evolution and glide within a thin film grain is required to understand in detail the evolution of the dislocation structure in a thin film system.

We also demonstrate the first systematic nanoindentation experiments on the patterned lines on substrates. The careful experiments with various boundary conditions on different platforms of instruments constantly and clearly show the effect of line width on the indentation response. Challenges in the positioning of indenter tip at the center of top surface of the patterned lines and large experimental scatter were successfully overcome. The free surface of the line side walls increase the compliance of material deformation in the very small scale of load and depth of indentation. The experimental trends are rationalized by the atomistic simulation of nanoindentation rather than by the continuum-based approach. This suggests that the initial stage material deformation during nanoindentation should be considered with a discrete description of defect generation and motion. However, the atomistic simulation performed in this study is limited by the simulation cell size, dimension, and unrealistic loading conditions. The extended molecular dynamic simulations with better boundary conditions could give us more insights of length scale effects on the early stage of nanoindentation. A mesoscale simulation, such as discrete dislocation dynamics, also allow a direct comparison of experiments and simulations, which leads us a better understating of underlying mechanism of initiation and propagation of inelastic deformation in small volume materials and the length scale effects.

Appendix A

Nanocrystallization During Nanoindentation of a Bulk Amorphous Metal Alloy at Room Temperature

An example of microstructural modifaction due to the nano-scale contact[1]

It is known that nanocrystallites can form in shear bands produced during severe bending or high-energy ball milling of thin ribbons of a metallic glass. We present direct experimental evidence that highly confined and controlled local contact at the ultra-fine scale in the form of quasi-static nanoindentation of a bulk glassy metal alloy at room temperature can also cause nanocrystallization. Atomic force microscopy and transmission electron microscopy show that nanocrystallites nucleate in and around shear bands produced near indents, and that they are the same as crystallites formed during annealing without deformation at 783 K. Drawing an analogy with recent experiments in glassy polymers, these results are reasoned to be a consequence of flow dilatation inside the bands and the

[1]This ariticle published in *Science*, Vol. 295, 25 January 2002, with co-authors: J.-J. Kim, S. Suresh, and A.S. Argon

attendant, radically enhanced atomic diffusional mobility inside actively deforming shear bands.

The structure, thermodynamic stability, as well as electrical and magnetic properties of thin ribbons of amorphous metal alloys have been the focus of many theoretical and experimental investigations [118–123]. With the development of techniques to produce bulk metallic glasses, the mechanical properties of amorphous alloys have also become topics of scientific and technological interest [124–130] for structural and functional applications. Bulk amorphous alloys exhibit unique properties: high strength, localized deformation by shear banding, paucity of strain hardening, and much higher hardness than crystalline alloys of comparable elastic modulus. Since glassy alloys do not exist in thermodynamic equilibrium, they undergo crystallization with the supply of thermal energy.

Experiments have also shown that severe bending of thin ribbons of amorphous glasses can lead to the formation of shear bands within which nanocrystallites could be nucleated [123]. In addition, high energy ball milling or mechanical alloying of thin ribbons of some Al-based amorphous metals has been found to induce nanocrystallites whose underlying mechanistic processes can be different from those occurring during thermal anneal [131, 132]. Ball milling produces highly complex and uncontrolled stress states, and the possibility of significant local heating during high energy ball milling has remained a topic of controversy. To our knowledge, no experimental information is currently available on the possibility of nanocrystallization in a bulk amorphous alloy subjected to well-controlled, slow (quasi-static), ultrafine-scale normal contact at room temperature. Such information would be of considerable use in elucidating the mechanisms of deformation-induced crystallization of an amorphous metal on several counts. (a) It is known that discontinuous shear bands form locally around indentations in bulk amorphous alloys [129, 130]. It would be of interest to ascertain whether nanocrystallites form in the vicinity of these identation-induced bands. (b) Nanoindentation provides a convenient and controlled method for introducing highly localized mechanical deformation in a bulk amorphous alloy at room temperature without the possibility of significant increase in local temperature that could alter microstructural evolution. (c) Instrumented, depth-sensing nanoindentation is finding wider use as a tool to extract the local mechanical properties of a broad range of materials, including amorphous alloys [128, 129]. It is of fundamental interest to learn if and how microstructural

changes can be introduced during nanoindentation; such changes, in turn, could influence the accuracy of mechanical property determination in glassy metal alloys.

The nominal chemical composition of the bulk metallic glass used in the present study was Zr-17.9Cu-14.6Ni-10Al-5Ti (atomic per cent). The alloy was prepared by arc-melting and drop-casting method. The as-cast specimen was of cylindrical shape with a diameter of 6.7 mm, and the fully amorphous as-cast condition was verified. Further details on the melting and preparation of the alloy as well as basic structural evolution can be found elsewhere [133]. Nanoindentation experiments were carried out on the alloy with a diamond Berkovich (three-sided pyramid) indenter mounted in a nanoindenter. Depth-sensing indentations covering a complete loading and unloading sequence were made, in a load-control mode, to maximum loads of 20 mN for the transmission electron microscope (TEM) and 20 mN and 60 mN for atomic force microscope (AFM) observations[2]. The quasi-static indentation experiments were conducted at a loading/unloading rate of no more than 2 mN/s. Although nanoindentation of a bulk amorphous metal is a rather straightforward task, preparation of TEM specimens containing the nanoindents without inducing microstructural changes in the region surrounding the indent and quantitative analyses of crystallization induced in and around the indents involve considerable experimental challenges. With these issues under consideration, specimens of the metallic glass were cut into the shape of a disc, 3 mm in diameter, and carefully thinned down to a thickness of 100 mm for later TEM observation. After indentation, thinning of the specimen was accomplished only from the side opposite to the indented surface, and the time for dimpling was maximized to reduce the final ion-milling time so as to minimize any damage or change to the microstructure near the indented area. Subsequent foil preparation steps involved ion-milling with the indented surface of the specimen facing down, and the ion-milling stage was shielded by a hollow metal cylinder so as to protect the indented side from re-deposition of any sputtered species produced during the milling process. The TEM observations of the reference, unindented regions also involved an identical ion milling procedure so that the

[2]Nanoindentation experiments were conducted in a load-control mode using the NanoTest™ Ltd, Micro-Materials, Wrentham, UK. For TEM observation, up to 400 indentations, equally spaced in the horizontal and the vertical directions with 20 mm separation, were made on the specimen that was previously cut into a disk 3 mm in diameter. For AFM, ten indents for each load level were made. Electron microscopy studies were made using model 200CX, JEOL TEM operating at 200 kV. The specimens for TEM observations were prepared by ion milling methods using a Gatan Duo-Mill™ at 0.5 mA and 4 kV. The AFM studies were conducted on Nanoscope IIIa Scanning Probe Microscope™ from Digital Instruments.

sole effects of nanoindentation on structural changes could be interpreted in a controlled manner.

Figure A-1 (A) shows an AFM image of discontinuous shear bands formed around an indent made under a maximum load of 60 mN (indenter penetration depth $\sim$ 720 nm) in the glassy alloy. Here, the existence of intense bands of shear along the sides of the pyramidal impression bounded within the triangular indent is evident. Shear bands formed around an indent made at a maximum load of 20 mN (indenter penetration depth $\sim$ 400 nm) are seen in the TEM image [Fig. A-1 (B)]. Figure A-2 (A) is a dark-field TEM image of the center region of the indenter impression directly beneath the indenter tip. Also shown in this figure is the corresponding selected area diffraction (SAD) pattern. Since the aperture size for SAD is comparable to the indent size, electron diffraction produces both a diffused halo ring pattern, representative of the amorphous material, and distinct spots, representative of the nanocrystallites. Figure A-2(B) is a dark-field TEM image of the indented region where the dark triangular zone representing the indent impression is visible since the surface thinned from the backside extended to the full depth of the indent. When the SAD pattern is obtained in a region located at a small distance from the indent, where no crystallites form, only a diffused ring pattern representing a fully amorphous material was observed (bottom right image of Fig. A-2 (B)). The same ring patterns associated with the fully amorphous structure were seen in the as-received material using the same TEM foil preparation methods. On the other hand, SAD analysis of the indent reveals clear diffraction spots associated with the presence of nanocrystallites. The six spots, which are close to the exact Bragg condition, near the directly transmitted beam of the SAD pattern (Fig. A-2 (B) bottom left image and schematic) were identified as being produced by diffraction from the (111) planes of Zr_2Ni nanoparticles. The presence of nanocrytallites can be clearly seen in the TEM image. It is also evident from the TEM images of Figs. A-2 (A) and (B) that the nanocrystallites form both along the faces of the indent and in the region beneath the indent tip, where the most severe deformation occurs. Analysis of the nanocrystallites indicates that the particles range in size from 10 nm to 40 nm, with a median particle diameter of approximately 20 nm. The surface uplift produced by the pile-up of material around the indent is seen from the AFM image of Fig. A-3 (A). Quantitative analysis of surface uplift in the AFM shows that indentation results in pile-up of as much

as 150 nm above the average surface level in this non-hardening material [Fig. A-3 (B)], indicating the severity of local plastic flow around the indent.

Systematic experiments [128] on the crystallization of the present bulk amorphous alloy under thermal annealing, in the absence of any mechanical deformation, have shown that no discernible crystallization occurs up to a temperature of at least 683 K. At an annealing temperature of 783 K, partial crystallization occurs whereby primary crystallites of tetragonal Zr_2Ni nucleate. These crystallites are the same as those formed in the present nanoindentation experiments at room temperature. However, spot distributions in the SAD patterns of Figs. A-2 (A) and (B) show that the crystallographic orientations of nanocrytallites are not perfectly random. Preferential crystallographic alignments can occur in the deformation induced nanocrytallites, unlike that seen during thermal annealing.

The formation of nanocrystallites in our nanoindentation tests, whose duration is roughly 10 s, points to the need for high atomic mobility. The rate controlling process in the formation of Zr_2Ni is expected to be the diffusion of Ni. The required diffusion constant is simply estimated to be $D \sim L^2/4t$, where L is the distance over which the constituent atoms are gathered (which we estimate to be twice the average crystallite size of 20 nm), and $t = 10$ s, is the indentation time. This gives $D \sim 4 \times 10^{-17} m^2/s$. Diffusion constants of this magnitude are typically observed in metallic glasses only above their glass transition temperatures [134].

To explain such high atomic mobilities, several possibilities are considered here. Suggestions of local reordering during shear of an amorphous solid [123] have been made to explain the nucleation of stable clusters or embryos by exchange of atomic positions within shear band during large deformation. However, no evidence has been provided, on the basis of such arguments, for the large atomic mobility needed to form crystallites that are 10–40 nm in size. A large rise in local temperature, of up to several hundred degrees, has also been suggested to result from the adiabatic shear of metallic glass [135]. Such a situation, however, may be more likely during dynamic loading and/or fracture. For the present situation of shear bands connected to surrounding ideal heat sinks around quasi-statically produced indents, an estimate by Eshelby and Pratt [136] of temperature rise inside a shear

band should be more appropriate:

$$\Delta T = \frac{\sigma \dot{\gamma}_b h}{2\pi k} \sqrt{\frac{\pi k \Delta\gamma}{c_p \gamma_b}} \tag{A.1}$$

Here σ (= 1.23 GPa) is the plastic shear (yield) resistance, is the shear strain rate inside the band which is estimated to be 10^3 s^{-1} [137], h and $\Delta\gamma$ are the thickness and the total shear strain increment inside the band (which are estimated to be 12 nm and 2, respectively, from Figs. A-1 (A) and A-3), and k and c_p are the thermal conductivity and specific heat of the alloy which should roughly equal 3.5 $J/ms \cdot K$ and 5.5×10^6 $J/m^3 \cdot K$ for a typical metallic glass [133, 138]. Evaluation of eq. (A.1) gives a temperature rise of 0.05 K. Such estimates of insignificant temperature rise are also consistent with experimental measurements of local temperature rise even in the severely deformed plastic region of quasi-statically loaded crack tips [139]. The influence of the hydrostatic pressure underneath the indenter on the crystallization temperature of the amorphous alloy strongly depends on composition and the density difference between the crystalline and amorphous phase. It is also known, however, that hydrostatic pressure markedly inhibits precipitate growth [140]. In the present experiments, the nanocrystallites exhibit an average size of approximately 20 nm during quasi-static indentation experiments of only about 10 s duration.

It has been proposed [138, 141], and verified by direct measurements [142], that shearing of an amorphous material well below its glass transition temperature (T_g) can result in flow dilatation which autocatalytically causes intense shear localization within the shear bands themselves. Much more importantly, it has recently been established by direct diffusional measurements [143] that flow-induced dilatation inside actively deforming shear bands in disordered solids must have atomic level topological features and mobility characteristics that are nearly identical to those at Tg of the solid where thermally induced increase of local dilatation (free volume) results in a sharp reduction in interatomic interaction. Specifically, it has been shown that the penetration rate of a low molecular weight diluent into an actively plastically deforming high molecular weight glassy polymer at 386 K is nearly identical to the penetration rate at the glass transition temperature of 486 K. Without active plastic flow, the penetration rate at 386 K is immeasurable, which indicates that the observed effect of plastic flow in this glass is equivalent to an increase in the diffusion

constant by as much as a factor of 2×10^4 [143]. Corresponding experiments in amorphous metals have not yet been performed and there are important topological differences between glassy polymers and glassy metal alloys. However, there exists a striking similarity in the phenomenology and deformation mechanisms between the metallic and polymeric glasses [144]. We, therefore, conclude that the observed rapid formation of Zr_2Ni nanocrystallites around the shear bands of our bulk amorphous alloy is a direct consequence of the inevitable dynamic flow dilatation in the actively deforming bands (without any significant increase in temperature during plastic flow), and the attendant dramatic enhancement in atomic diffusional mobility.

In summary, the present work provides direct experimental evidence that controlled and highly confined local contact deformation in the form of quasi-static nanoindentation of a bulk metallic glass at room temperature results in nanocrystallization. Additional features of the present experiments are that nanocrystallization due to ultrafine-scale contact occurs even without the possibility of significant local heating, and that the nanocrystallites are identified to be the same as those found during thermal anneal at 783 K without any mechanical deformation or indentation. In order to explain these results, we invoke a mechanistic rationale predicated upon radically enhanced atomic diffusional mobility by drawing an analogy with recent experimental observations of enhanced diffusion in actively deforming amorphous polymers.

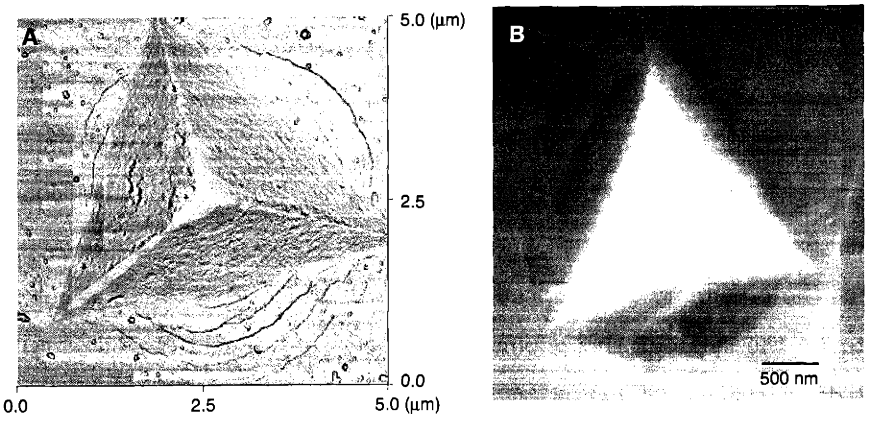

Figure A-1: Images of deformation around ultra-fine-scale indents. (A) AFM illumination mode image (5 μm$\times$5 μm) of an indented impression after a 60 mN maximum load. The characteristic circular patterns around the triangular indent impression constitute "pile-up", which represents overlapping layers of displaced material. Similar patterns also can be found along the pyramidal faces of the indent. (B) Bright field TEM image of an indented impression after a 20 mN maximum load. It also shows the same circular patterns around the triangular indent hole in a thin foil.

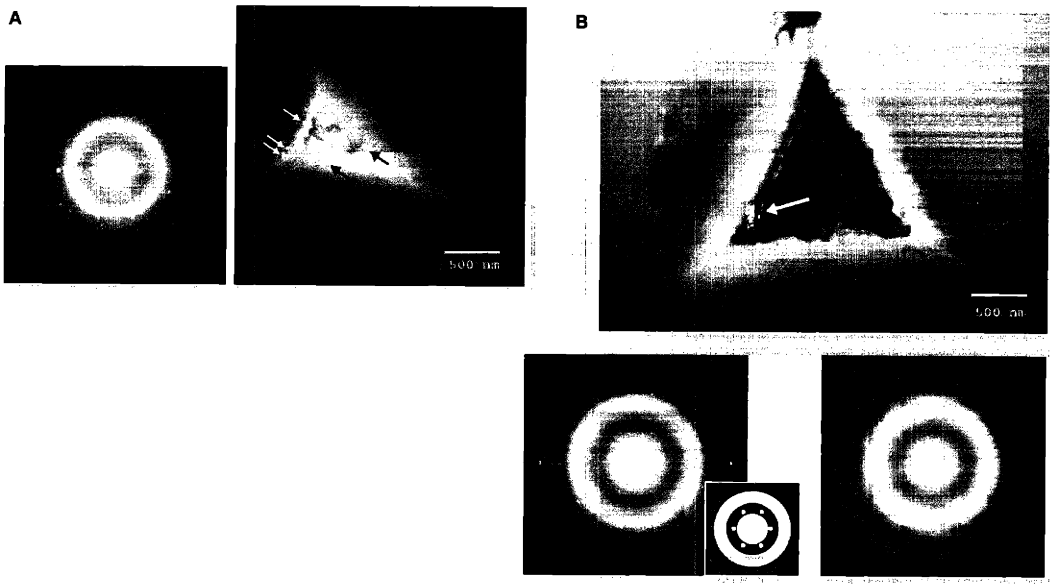

Figure A-2: Dark field TEM images of indents with nanocrystallites and their corresponding SAD patterns. The maximum applied load for these indents was 20 mN. (A) SAD pattern obtained from a region of indent beneath the indenter tip and dark field TEM image constructed using a diffracted spot in the SAD pattern. Since the thickness of the TEM foil directly beneath the indent impression is only slightly greater than the maximum penetration depth of indenter ($\sim$ 400 nm) and since the electron beam can transmit only near the indent tip region, we are able to see the region beneath the indenter tip (or the central region of the indent) in this image. The dark field shows a few groups of clustered nanocrystallites inside the indent, as indicated by the arrows. (B) Dark field TEM image obtained from an indented triangular hole and SAD patterns obtained in a region located at a small distance outside of the indent (bottom right) and from the indent (bottom left and schematic). In the dark field image, the arrow indicates clustered nanocrystallites at the edge of dark triangular zone, which is a hole made by the backside thinning through the indent impression. Six spots around transmitted beam in the schematic are analyzed and are found to be associated with the (111) plane of tetragonal Zr_2Ni (space group I4/mcm, a = 6.49 Å, c = 5.28 Å). Halo rings of the bottom right SAD pattern without spots indicate fully amorphous structure of metallic glass in a region that is not affected by the indentation.

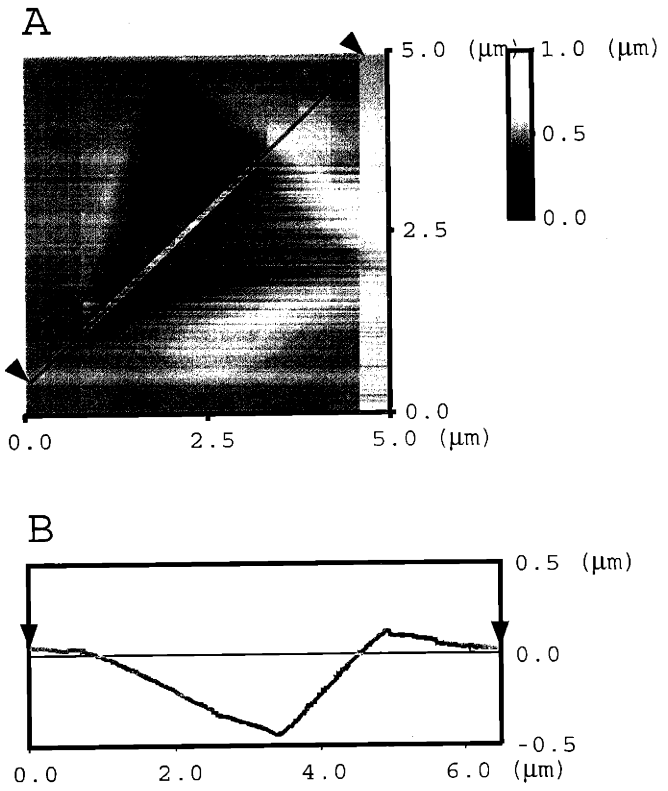

Figure A-3: Atomic force microscope analysis after 60 mN maximum load. (A) AFM height mode image (5 μm×5 μm) of an indent. We also see the characteristic circular patterns around such indent again, and the colored height information around the triangular indent reveals both large material pile-up at the perimeter of the indent and overlapping layers of severely displaced materials. (B) Cross sectional profile of the indent, along the green line of Fig. 3A, showing the surface uplift along one side to be as much as 150 nm above the reference surface. This large pile-up height around the perimeter of the indent, compared to the penetration depth (720 nm), indicates that the severity of plastic flow around this region during indentation.

Appendix B

Nanoindentation Experimental Details

B.1 Experimental procedure on NanoTest 600

This is the step-by-step procedure of nanoindentation experiment on patterned lines using NanoTest 600 (MicroMaterials, Ltd., Wrexham, UK).

1. Perform all nessesary calibration steps before sample loading: Series of calibration steps include Frame compliance, Load, Depth, and Diamond area calibrations.
2. Load a sample on the sample holder.
3. Turn the high resolution microscope on. (type C:\MICRO ON in DOS command line.)
4. Turn on the indenter machine in NT2 mode. (type C:\NT 2 and C:\MAIN in DOS command line.)
5. Perform the pendulum test.
6. Perform the microscope calibrations.

7. Move the specimen to the microscopeposition, and find a set of patterned lines to be indented.

8. Adjust the direction of patterned lines parallel to the y direction of specimen stage. Secure the specimen holder.

9. Move back the specimen to the indenter position, and find the contact position.

10. Retract the specimen 5 μm.

11. Get out of the MAIN software and run WIRESCAN software. WIRESCAN software is a modified sctratch test software and allows us to scan the profile of line surfaces.

12. Set a scan condition, and perform a scan. A typical scan condition is: scan length = 10 $\times$ line width, applied load = 0 or the minimum allowed load, scan speed = 200 nm/sec. An example of scanned profile of patterned lines is presented in Fig. B-1.

13. Keeping in mind the shape of the scanned profile, perform another scan. Stop the scan as soon as the scanned profile reaches the center of the line, as indicated with an arrow in Fig. B-1. The machine will automatically retract the specimen 5 μm from the contact position without changing x and y positions of the specimen.

14. Get out of the WIRESCAN software, and go back to the MAIN software.

15. Perform a series of indentations with a 5 μm separation along the y direction. In order to find the impressions easily under the microscope in the next step, the maximum depth is set to be deeper than actual experiments.

16. Move the specimen to the microscope, and examine the indentation impressions. If the impressions are not aligned along the center of the line, perform steps from 8 to 16 again. If the impressions are well aligned along the center of the line, move the specimen to the clean region of the line, and perform steps from 11 to 15 with a appropriate experimental condition.

17. Finally, check the position of indentation impressions with other high magnification microscope after unloading the specimen from NanoTest 600. If positions of impressions are not satisfied, discard all experimental data, and perform the whole sequence again.

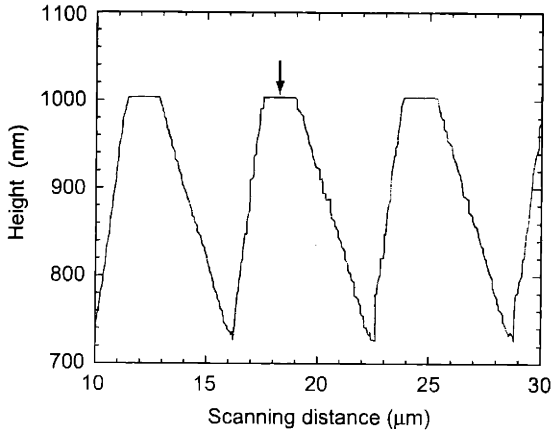

Figure B-1: Scanned profile of patterned lines by WIRESCAN software. The arrow indicates the center of a line.

B.2 Experimental procedure on Triboindenter

This is the step-by-step procedure of nanoindentation experiment on patterned lines using Triboindenter (Hysitron, Inc., Minneapolis, MN).

1. Perform all nessesary calibrations before sample loading: Series of calibration steps include Air indent, Area function, and Machine compliance calibrations.

1. Load a specimen.

2. Calibrate the microscope off-set.

3. Turn on the image mode. In this mode, the machine scan the specimen surface using the indenter tip, and construct an AFM-like image. Set the contact load appropriately to maintain the contact during scanning and to minimize a damage on the line surface, usually the contact load is 1 μN.

4. Adjust the scanning image size and speed appropriately with the line width. Move the line into the center of the scanning image.

5. Set up indentation parameters, and perform an indentation experiment.

6. Re-scan the indented area, and make sure the impression is located at the center of the line.

7. Move to the different position of the line, and perform the steps from 4 to 6.

Bibliography

[1] S.M. Hu. *J. Appl. Phys.*, 70(6):R53, 1991.

[2] W.D. Nix. *Metall. Trans.*, 20A:2217, 1989.

[3] *Thin Films: Stresses and Mechanical Properties I-VIII., MRS Procedings*, Pittsburgh PA, 1988-1998.

[4] L.B. Freund. *J. Mech. Phys. Solids*, 48:1159, 2000.

[5] R.W. Hoffman. *The Mechanical Properties of Thin Condensed Films, Physics of Thin Films*, Vol. 3, page 211. Academic Press, New York, edited by g. hass and r.e. thun edition, 1966.

[6] K.L. Chopra. *Thin Film Phenomena*, page 266. McGraw-Hill, New York, 1969.

[7] C.V. Thompson. *Annu. Rev. Mater. Sci.*, 38:159, 2000.

[8] L.B. Freund and S. Suresh. *Thin Film Materials: Stress, Defect Formation, and Surface Evolution.* Cambridge University Press, Cambridge, U.K., in press.

[9] M.A. Korhonen, P. Børgesen, K.N. Tu, and C.-Y. Li. *J. Appl. Phys.*, 73:3790, 1993.

[10] J.J. Clement and C.V. Thompson. *J. Appl. Phys.*, 78:900, 1995.

[11] R.J. Gleixner, B.M. Clemens, and W.D. Nix. *J. Mater. Res.*, 12:2081, 1997.

[12] B.Greenbaum, A.I. Sauter, P.A. Flinn, and W.D. Nix. *Appl. Phys. Lett.*, 58:1845, 1991.

[13] P.Børgesen, J.K. Lee, R.J. Gleixner, and C.-Y. Li. *Appl. Phys. Lett.*, 60:1706, 1992.

[14] J.W. Hutchinson and Z. Suo. *Advances in Applied Mechanics*, 29:63, 1992.

[15] J.W. Hutchinson, M.D. Thouless, and E.G. Liniger. *Acta Metall. Mater.*, 40:295, 1992.

[16] R.H. Dauskardt, M. Lane, Q. Ma, and N. Krishna. *Engin. Fract. Mech.*, 61:141, 1998.

[17] S.M. Spearing. *Acta Mater.,* The Millennium Special Issue, edited by S. Suresh, 48:179, 2000.

[18] H. Huang and F. Spaepen. *Acta Mater.*, 48:3261, 2000.

[19] E. Arzt. *Acta Mater.*, 46:5611, 1998.

[20] M. Murakami. *Thin Solids Films*, 59:105, 1979.

[21] R. Venkatraman and J.C. Bravman. *J. Mater. Res.*, 7(8):2040, 1992.

[22] R.-M. Keller, S.P. Baker, and E. Arzt. *J. Mater. Res.*, 13:1307, 1998.

[23] J.E. Siewenie and L. He. *J. Vac. Tech. A*, 17(4):1799, 1997.

[24] G. Chen and P. Hui. *Appl. Phys. Lett.*, 74:2942, 1999.

[25] G. Bochi, C.A. Ballentine, H.E. Inglefield, C.V. Thompson, and R.C. O'Handley. *J. Appl. Phys.*, 79:5845, 1996.

[26] O. Kraft and C.A. Volkert. *Adv. Eng. Mat.*, 3(3):99, 2001.

[27] D.F. Bahr, D.E. Kramer, and W.W. Gerberich. *Acta Mater.*, 46:3605, 1998.

[28] W.W. Gerberich, D.E. Kramer, N.I. Tymiak, A.A. Volinsky, D.F. Bahr, and M.D. Kriese. *Acta Mater.*, 47:4115, 1999.

[29] S. Suresh, T.G. Neih, and B.W. Choi. *Scripta Mater.*, 41:951, 1999.

[30] J. Li, K.J. Van Vliet, K.J. Zhu, S. Yip, and S. Suresh. *Nature*, 418:307, 2002.

[31] M. Oring. *The Materials Science of Thin Films.* Academic Press, New York, 1992.

[32] M. Murakami, T.-S. Kuan, and I.A. Blech., page 164, *Treatise on Materials Science and Technology, Vol. 24,* edited by G. Hass and R.E. Thun., Academic Press, New York, 1982.

[33] J.M. Blakely. *J. Appl. Phys.*, 35:1756, 1964.

[34] M.F. Doerner, D.S. Gardner, and W.D. Nix. *J. Mater. Res.*, 1(6):845, 1986.

[35] L.B. Freund. *J. Appl. Mech.*, 54:553, 1987.

[36] L.B. Freund. *Advances in Applied Mechanics*, 30:1, 1994.

[37] R. Venkatraman, S. Chen, and J.C. Bravman. *J. Vac. Sci. Technol. A*, 9:2536, 1991.

[38] W.D. Nix. *Scripta Mat.*, 39(4-5):545, 1998.

[39] W.W. Mullins. *Acta Metall.*, 6:414, 1958.

[40] C.V. Thompson. *J. Mater. Res.*, 8:237, 1993.

[41] J.W. Matthews. *Epitaxial Growth,* edited by J.W. Matthews, page 560. Academic Press, New York, 1975.

[42] T.S. Kaun and M. Murakami. *Metall. Trans.*, 13A:383, 1982.

[43] R. Venkatraman, J.C. Bravman, W.D. Nix, P.W. Davis, P.A. Flinn, and D.B. Fraser. *J. Electron. Mater.*, 19(11):1231, 1990.

[44] J.P. Hirth and J. Lothe. *Theory of Dislocations*, page 169. John Wiley, New York, 2nd edition, 1982.

[45] M.J. Kobrinsky and C.V. Thompson. *Acta Mater.*, 48:625, 2000.

[46] M. Hommel and O. Kraft. *Acta Mater.*, 49:3935, 2001.

[47] M. Murakami. *Acta Metall.*, 26:175, 1978.

[48] M.A. Meyers and K.K. Chawla. *Mechanical Metallurgy: principles and applications*, page 494. Prentice-Hall, New Jersey, 1984.

[49] H. Mecking. *Deformation of Polycrystals*, page 1573. Strength of Metals and Alloys, edited by P. Haasen, V. Gerold and G. Kostorz. Pergamon press, New York, 1979.

[50] H. Gleiter. *Acta Mater.,* The Millennium Special Issue, edited by S. Suresh, 48:1, 2000.

[51] N.E. Dowling. *Mechanical Behavior of Materials*, page 170. Prentice-Hall, New Jersey, 1997.

[52] Y-L. Shen, S. Suresh, M.Y. He, A. Bagchi, O. Kienzle, M. Rühle, and A.G. Evans. *J. Mater. Res.*, 13(7):1928, 1998.

[53] S.P. Baker. *Mat. Sci. Eng.*, A319-321:16, 2001.

[54] W.M. Kuschke and E. Arzt. *Appl. Phys. Lett.*, 64:1097, 1994.

[55] R.-M. Keller, S.P. Baker, and E. Arzt. *Acta Mater.*, 47:415, 1999.

[56] Y.-L. Shen and S. Suresh. *Acta Metall. Mater.*, 43:3915, 1995.

[57] M.J. Kobrinsky. PhD thesis, Massachusetts Institute of Technology, 2001.

[58] J. Bauschinger. *Mitt. Mech. Tech. Lab.*, 13:1, 1886.

[59] S. Suresh and A. Mortensen. *Fundamentals of Functionally Graded Materials.* Institute of Materials, U.K., 1998.

[60] R.J. Arsenault and U.T.S. Pillai. *Metall. Mat. Trans.*, 27A:995, 1996.

[61] M. Taya, K.E. Lulay, K. Wakashima, and D.J. Lloyd. *Mat. Sci. Eng.*, A124:103, 1990.

[62] N. Christodoulou, O.T. Woo, and S.R. Macewn SR. *Acta Metall.*, 34:1553, 1986.

[63] O.B. Pedersen, L.M. Brwon, and W.M. Stobbs. *Acta Metall.*, 29:1843, 1981.

[64] A.P. Reynolds and S.C. Baxter. *Mater. Sic. Eng.*, A285:265, 2000.

[65] P. Pant, K.W. Schwarz, and S.P. Baker. *MRS Symp. Proc.*, Vol. 673, 2001.

[66] S.P. Baker, R.-M. Keller, and E. Arzt. *MRS Symp. Proc.*, Vol. 505:605, 1998.

[67] G. Masing. *Wiss. Veröff. Siemens-Konzern.*, 3:231, 1927.

[68] R.J. Asaro. *Acta Metall.*, 23:1255, 1975.

[69] Z. Mróz. *J. Mech. Phys. Solids*, 15:163, 1967.

[70] P.S. Bate and D.V. Wilson. *Acta metall.*, 34:1097, 1986.

[71] Z. Li and H. GU H. *Matall. Trans.*, A21:717, 1990.

[72] Y. Choi and S. Suresh. *Acta Mater.*, 50:1881, 2002.

[73] G. G. Stoney. *Proc. R. Soc. Lond.*, A82:172, 1909.

[74] P.A. Flinn and C. Chiang. *J. Appl. Phys.*, 67(6):2927, 1990.

[75] B. Greenebaum, A.I. Sauter, P.A. Flinn, and W.D. Nix. *Appl. Phys. Lett.*, 58(17):1845, 1991.

[76] A. Gouldstone, Y.-L. Shen, S. Suresh, and C.V. Thompson. *J. Mater. Res.*, 13:1956, 1998.

[77] A. Gouldstone, A. Wikström, P. Gudmundson, and S. Suresh. *Scripta Mater.*, 41(3):297, 1999.

[78] T.-S. Park and S. Suresh. *Acta Mater.*, 48:3169, 2000.

[79] A. Wikström, P. Gudmundson, and S. Suresh. *J. Mech. Phys. Solids*, 47:1113, 1999.

[80] A. Wikström, P. Gudmundson, and S. Suresh. *J. Appl. Phys.*, 86:6088, 1999.

[81] G.M. Pharr and W.C. Oliver. *MRS Bull.*, 7:28, 1992.

[82] W.D. Nix. *Mat. Sci. Eng.*, A234-236:37, 1997.

[83] A. Gouldstone, H.J. Koh, K.Y. Zeng, A.E. Giannakopoulos, and S. Suresh. *Acta. Mater.*, 48:2277, 2000.

[84] S. Suresh and A. E. Giannakopoulos. *Acta Mater.*, 46:5755, 1998.

[85] T. Sawa, Y. Akiyama, A. Shimamoto, and K. Tanaka. *J. Mater. Res.*, 14:2228, 1999.

[86] K.L. Johnson. *Contact Mechanics.* Cambridge University Press, Cambridge, UK, 1985.

[87] A. Gouldstone, K. J. Van Vliet, and S. Suresh. *Nature*, 611:656, 2001.

[88] K.J. Van Vliet. PhD thesis, Massachusetts Institute of Technology, 2002.

[89] A.K. Bhattacharya and W.D. Nix. *Int. J. Solids Struc.*, 24:1287, 1988.

[90] T.Y. Tsui and G.M. Pharr. *J. Mater. Res.*, 14(1):292, 1999.

[91] R. Saha and W.D. Nix. *Acta Mater*, 50:23, 2002.

[92] T. Ohmura, S. Matsuoka, K. Tanaka, and T. Yoshida. *Thin Solid Films.*, 385:198, 2001.

[93] X. Chen and J.J. Vlassak. *J .Mater. Res.*, 16(10):2974, 2001.

[94] P.A. Flinn. *J. Mater. Res.*, 6:1498, 1991.

[95] I.-S. Yeo, S.G.H. Anderson, P.S. Ho, and C.K. Hu. *J. Appl. Phys.*, 78(2):945, 1995.

[96] I.-S. Yeo, P.S. Ho, and S.G.H. Anderson. *J. Appl. Phys.*, 78(2):953, 1995.

[97] *ABAQUS Version 6. 1: General Purpose Finite Element Program.* Hibbit, Karlson and Sorensen Inc., Pawtucket, RI, USA, 2000.

[98] F.A. McClintock and A.S. Argon edited. *Mechanical Behavior of Materials*, page 123. Addison-wesley, Reading, MA, 1966.

[99] M. Dao, N. Chollacoop, K.J. Van Vliet, T.A. Venkatesh, and S. Suresh. *Acta. Mater.*, 49:3899, 2001.

[100] J.A. Knapp, D.M. Follstaedt, S.M. Mayer, J.C. Bardour, and T.A. Friedmann. *J. Appl. Phys.*, 85(3):1460, 1999.

[101] M. Lichinchi, C. Lenardi, J. Haupt, and R. Vitali. *Thin Solid Films*, 333:278, 1998.

[102] Y.T. Cheng and C. M. Cheng. *J. Appl. Phys.*, 84:1284, 1998.

[103] Y.T. Cheng and C. M. Cheng. *J. Mater. Res.*, 14:3493, 1999.

[104] W.C. Oliver and G.M. Pharr. *J. Mater. Res.*, 7:1564, 1992.

[105] M.F. Doener and W.D. Nix. *J. Mater. Res.*, 1:601, 1986.

[106] A.E. Giannakopoulos and S. Suresh. *Scripta Mater.*, 40:1191, 1999.

[107] T.Y. Tsui, W.C. Oliver, and G.M. Pharr. *J. Mater. Res.*, 11(3):752, 1996.

[108] A.K. Bhattacharya and W.D. Nix. *Int. J. Solids Struc.*, 24:881, 1988.

[109] D. Ma, K. Xu, and J. He. *Thin solid Films*, 323:183, 1998.

[110] Y. Sun, T. Bell, and S. Zheng. *Thin Solid Films*, 258:198, 1995.

[111] J.A. Zimmerman, C.L. Kelchner, P.A. Klein, J.C. Hamilton, and S.M. Foiles. *Phys. Rev. Lett.*, 87:165507, 2001.

[112] J.D. Kiely, , and J.E. Houston. *Phys. Rev. B*, 57:588, 1998.

[113] R. Phillips, D. Rodney, V. Shenoy, E. Tadmor, and M. Ortiz. *Model. Simul. Mater. Sci. Eng.*, 7:769, 1999.

[114] H.J.C. Berendsen, J.P.M. Postma, W.F. van Gunsteren, A. DiNola, and J.R. Haak. *J. Chem. Phys.*, 81:3684, 1984.

[115] Y. Mishin nad M. J. Mehl, D. A. Papaconstantopoulos, A. F. Voter, and J. D. Kress. *Phys. Rev. B*, 63:224106, 2001.

[116] T. Zhu, J. Li, K.J. Van Vliet, S. Suresh, and S. Yip. *submitted to J. Mech. Phys. Solids.*

[117] M.L. Öveçoğlu, M.F. Doerner, and W.D. Nix. *Acta metall.*, 35(12):2947, 1987.

[118] Y. He, S.J. Poon, and G.J. Shiflet. *Science*, 241:1640, 1988.

[119] A.L. Greer. *Science*, 267:1947, 1995.

[120] I. Mat'ko, E. Illeková, P. Švec, and P. Duhaj. *Mater. Sci. Eng.*, A225:145, 1997.

[121] A. Makino, A. Inoue, and T. Masumoto. *Mater. Trans. Japan Inst. Mater.*, 36:924, 1995.

[122] T. Masumoto and R. Maddin. *Mater. Sci. Eng.*, 19:1, 1975.

[123] H. Chen, Y. He, G.J. Shiflet, and S.J. Poon. *Nature*, 367:541, 1994.

[124] A. Inoue, T. Zhang, and T. Masumoto. *Mater. Trans. Japan Inst. Mater.*, 31:177, 1990.

[125] A. Peker and W.L. Johnson. *Appl. Phys. Lett.*, 63:2342, 1993.

[126] A. Inoue. *Acta Mater.* The Millennium Special Issue, edited by S. Suresh, 48:279, 2000.

[127] P.E. Donovan. *Acta Metall.*, 37:445, 1989.

[128] J.G. Wang, B.W. Choi, T.G. Nieh, and C.T. Liu. *J. Mater. Res.*, 15:798, 2000.

[129] R. Vaidyanathan, M. Dao, G. Ravichandran, and S. Suresh. *Acta Mater.*, 49:3781, 2001.

[130] W.J. Wright, R. Saha, and W.D. Nix. *Mater. Trans. Japan Inst. Mater.*, 42:642, 2001.

[131] Y. He, G.J. Shiflet, and S.J. Poon. *Acta Metall. Mater.*, 43:83, 1995.

[132] K. Lu. *Mater. Sci. Eng.*, R16:161, 1996.

[133] C.T. Liu *et al. Metall. Mater. Trans.*, A29:1811, 1998.

[134] B. Cantor. *in Amorphous Metals and Semiconductors,* edited by P. Haasen and R.I. Jaffee, pages 108–125. Pergamon Press, Oxford, UK, 1986.

[135] H.J. Leamy, H.S. Chen, and T.T. Wang. *Metall. Trans.*, 3:699, 1972.

[136] J.D. Eshelby and P.L. Pratt. *Acta Metall.*, 4:560, 1956.

[137] H. Neuhauser. *Scripta Metall.*, 12:471, 1978.

[138] A.S. Argon. *Acta Metall.*, 27:47, 1979.

[139] K.M. Flores and R.H. Dauskardt. *J. Mater. Res.*, 14:638, 1999.

[140] W.H. Wang, D.W. He, D.Q.Zhao, T.S. Yao, and M. He. *Appl. Phys. Lett.*, 75:2770, 1999.

[141] F. Spaepen. *Acta Metall.*, 25:407, 1977.

[142] J. Megusar, A.S. Argon, and N.J. Grant. in Rapidly Solidified Amorphous and Crystalline Solids, edited by B.H. Kear, B.C. Giessen and M. Cohen, pages 283–287. Elsevier, Amsterdam, The Netherlands, 1982.

[143] Q.-Y. Zhou, A.S. Argon, and R.E. Cohen. *Polymer*, 42:613, 2001.

[144] A.S. Argon. in Materials Science and Technology edited by R.W. Cahn, P. Haasen and E.J. Kramer, volume 6, pages 461–508. VCH, Weinheim, Germany, 1993.